Annual Report
Jahresbericht

2014

Walther–Meissner–Institut
für Tieftemperaturforschung
Bayerische Akademie der Wissenschaften

Contact:

Prof. Dr. Rudolf Gross
Walther–Meißner–Institut für Tieftemperaturforschung
Bayerische Akademie der Wissenschaften
and
Lehrstuhl für Technische Physik – E23
Technische Universität München

Address:

Walther–Meißner–Str. 8	Phone:	+49 – (0)89 289 14201
D - 85748 Garching	Fax:	+49 – (0)89 289 14206
GERMANY	e–mail:	Rudolf.Gross@wmi.badw.de
	WWW–address:	http://www.wmi.badw.de

Secretary's Office and Administration:

Emel Dönertas	Phone:	+49 – (0)89 289 14202
	Fax:	+49 – (0)89 289 14206
	e–mail:	Emel.Doenertas@wmi.badw.de
		Sekretariat@wmi.badw.de
Ludwig Ossiander	Phone:	+49 – (0)89 289 14205
	Fax:	+49 – (0)89 289 14206
	e–mail:	Ludwig.Ossiander@wmi.badw.de
		Verwaltung@wmi.badw.de

Preface

Dear colleagues, friends, partners, and alumni of the Walther-Meißner-Institute for Low Temperature Research (WMI) of the Bavarian Academy for Sciences and Humanities (BAdW)!

We are pleased to present to you our ***Annual Report 2014***, providing an overview on our last year's teaching, research and public outreach activities. In research, our activities extend from fundamental studies in solid state and quantum physics, application oriented studies, and materials science to technological developments in low temperature, thin film and nanotechnology. Our main research topics cover the fields of superconductivity and superfluidity, magnetism, ordering and emergent phenomena in correlated electron systems, spin electronics and spin caloritronics, as well as quantum information processing and quantum coherence in solid state systems. As every year, our Annual Report comes early to give you a timely piece of information. It contains concise summaries of our ongoing research projects, but also information on our teaching activities as well as some statistical data about publications, completed and ongoing Ph.D., diploma, master and bachelor theses, cooperations, funding, and recent developments in infrastructure and experimental facilities.

Our successful research in 2014 is reflected in more than 30 ISI-listed publications (see page 89), new extramural funding (see page 103), and fruitful collaborations with international research institutions and industry. The high international visibility of WMI is documented by more than 1500 citations of our publications in 2014 and a large number of invited conference presentations and seminar talks (see page 113). WMI also has organized workshops and conferences and was contributing to several public outreach events (see page 105).

The WMI research program is strongly dependent on third party funding. Therefore, we are particulary happy that we could acquire new funding by the International Ph.D. School of Excellence (IDK) entitled ***"Exploring Quantum Matter (ExQM)"*** within the ***Elite-Netzwerk Bayern***. ExQM is a joint program of TU Munich and LMU Munich in cooperation with the Walther-Meißner-Institute of BAdW and the Max-Planck-Institute for Quantum Optics (MPQ). It aims at designing quantum matter and understanding its complex behavior by large-scale simulation of correlated quantum systems in laboratory experiments. Moreover, our research within the ***Priority Program SPP 1538*** on "Spin Caloritronic Transport" was highly successful and a second funding period (07/2014 – 06/2017) has been granted by the German Research Foundation (DFG). For all other coordinated projects fortunately no review processes have been scheduled for 2014, allowing us to concentrate on science. This includes the Excellence Cluster ***Nanosystems Initiative Munich (NIM)***, the ***Collaborative Research Center 631***, the ***Transregional Collaborative Research Center TRR 80***, the ***Priority Program SPP 1450***, as well as the EU Project ***"Quantum Propagating Microwaves in Strongly Coupled Environments – PROMISCE"***.

The Marie Curie Initial Training Network on ***"Cavity and Circuit Quantum Electrodynamics – CCQED"*** will end early in 2015 after a highly successful four-year funding period. It was selected as one of eight *"success stories"* and invited by the German Federal Ministry of Education and Research (BMBF) to present its research and network activities on 28/29 January 2014 during the official launch of the new European Framework Programme for Research and Innovation, Horizon 2020, at Berlin. The launch event was attended by about 1000 guests from politics, research funding agencies, research institutions, industry and press, including high level speakers like the German Federal Minister for Education and Research, Johanna Wanka, and the EU-Commissioner for Research, Innovation and Science, Máire Geoghegan-Quinn. The CCQED exhibition stand received broad attendance and very positive feedback.

Keeping the technological infrastructure on a state-of-the-art level is a key prerequisite for successful experimental research. In this context, the year 2014 was brought good news. First,

supported by substantial funding of the Excellence Cluster Nanosystems Initiative Munich (NIM), we were able replace our electron beam writer. The new 100 kV nB5 Electron Beam Lithography System of NanoBeam Ltd., UK, with total cost exceeding 1 Mio. Euro has been delivered in October 2014. It has been installed inside the WMI clean room facility and meanwhile is already fully operational (see page 71). Second, the Bavarian Ministry for Science and Arts was granting up to 4.92 Mio. Euro to WMI for redevelopment measures regarding technical infrastructure, safety requirements and energy efficiency. The building project will also include the construction of a new stairwell, providing direct access to the new WMI Quantum Laboratories in the basement of the WMI building.

One of our most important assets is the large number of talented and dedicated students. Together with the scientific, technical and administrative staff they make our successful research possible by their hard work and persistence. In 2014, the total number of student helpers, bachelor, master/diploma and Ph.D. students was again exceeding the high value of 50. In total, 16 bachelor, 17 master/diploma, 1 Ph.D. and 1 habilitation theses were completed in 2014, while 18 master/diploma and 19 Ph.D. students are still ongoing with their work (see page 98). In the same way, an important prerequisite of success in science is the continuous support by various funding agencies. In this context we gratefully acknowledge financial support from the BAdW, the DFG, the Bavarian Ministry for Science and Arts, the BMBF and the EU. A further key to our success in research is the recruitment of outstanding, scientifically independent group leaders with complementary research interests and technical expertise, a process which is supported and monitored by the scientific advisory board of WMI. We are strongly committed to support and promote young scientists in their career.

I hope that our Annual Report 2014 inspires your interest in WMI. I take this opportunity to thank all the colleagues, guests, students, post–docs and cooperating partners, who contributed to our research and teaching activities within the last year, and last but not least all our friends and sponsors for their interest, trust and continuous support.

Rudolf Gross

Garching, December 2014

the majority of the WMI team members

Contents

The Walther–Meißner–Institute

General Information

The Walther–Meißner–Institute for Low Temperature Research (WMI) is operated by the Commission for Low Temperature Research of the Bavarian Academy of Sciences and Humanities (BAdW). The commission was founded in 1946 on Walther Meißner's initiative, who was president of BAdW from 1946 to 1950. The Commissions (Research Groups) of the Academy are set up in order to carry out long–term projects, which are too ambitious for the lifetime or capacity of any single researcher, or which require the collaboration of specialists in various disciplines. At present, the Bavarian Academy of Sciences and Humanities consists of 36 Commissions with more than 300 employees.

The Commission for Low Temperature Research of BAdW started its research activities in 1946 in the Herrsching barracks. After the retirement of Walther Meißner in 1952, Heinz Maier-Leibnitz, who followed Walther Meißner on the Chair for Technical Physics of the Technische Universität München, became the new head of the Commission for Low Temperature Research. In 1967, the commission moved to the Garching research campus after the construction of the new "Zentralinstitut für Tieftemperaturforschung (ZTTF)" was completed (director: Prof. Heinz Maier-Leibnitz, technical director: Prof. Franz Xaver Eder). Until 1972, the theory group of the Institute Laue Langevin was hosted at the ZTTF. In 1980, Prof. Dr. Klaus Andres became the new director of the ZTTF again associated with the Chair for Technical Physics (E23) at the Technische Universität München, followed by Prof. Dr. Rudolf Gross in 2000. In 1982, the ZTTF was renamed into Walther-Meißner-Institute for Low Temperature Research (WMI) on the occasion of Walther Meißner's 100. birthday.

Starting from 2000, the so far unused basement of the WMI building was made available for technical infrastructure (airconditioning, particulate airfilters, pure water system etc. for clean room) and additional laboratory space. Fortunately, in 2008 WMI succeeded in getting extra money from the state government within the so-called "Konjunkturpaket II". This money has been used to establish the new "WMI Quantum Science Laboratory" in the basement of the building, providing about $150\,m^2$ additional laboratory space particularly suited for low temperature facilities and ultra-sensitive studies on solid state quantum systems. The WMI Quantum Science Laboratory was fully operational early in 2011 and meanwhile is hosting three new mK systems.

As already mentioned, it is a long tradition that WMI hosts the Chair for Technical Physics (E 23) of the Technische Universität München (TUM) with the director of the WMI being a full professor at the Faculty of Physics of TUM. However, there are also close ties with the Ludwig-Maximilians-Universität (LMU). Between 2004 and 2010, WMI hosted a scanning probe division with the head of this division being a professor at the Ludwig-Maximilians-Universität (LMU). In this way a tight collaboration has been established between WMI and research groups of both Munich universities, joining technological and human resources in the fields of experimental and theoretical solid-state and condensed matter physics, low temperature techniques, materials science as well as thin film and nanotechnology. Noteworthy, the WMI supplies liquid helium to more than 25 research groups at both Munich universities and provides the technological basis for low temperature research.

Research Activities

The research activities of the Walther–Meißner–Institute are focused on low temperature condensed matter physics (see reports below). The research program is devoted to both **funda-**

mental and **applied research** and also addresses **materials science, thin film and nanotechnology** aspects. With respect to **basic research** the main focus of the WMI is on

- superconductivity and superfluidity,
- magnetism, spin transport, spin mechanics and spin caloritronics,
- quantum phenomena and quantum coherence in mesoscopic systems and solid state nanostructures,
- circuit quantum electrodynamics and circuit electro-nanomechanics,
- ordering and emergent phenomena in correlated electron systems,
- and the general properties of metallic systems at low and very low temperatures.

The WMI also conducts **applied research** in the fields of

- solid-state quantum information processing systems,
- superconducting and spintronic devices,
- oxide electronics,
- multi-functional and multiferroic materials,
- and the development of low and ultra-low temperature systems and techniques.

With respect to **materials science, thin film and nanotechnology** the research program is focused on

- the synthesis of superconducting and magnetic materials,
- the single crystal growth of oxide materials,
- the thin film technology of complex oxide heterostructures including multifunctional and multiferroic material systems,
- and the fabrication of superconducting, magnetic, and hybrid nanostructures.

The WMI also develops and operates systems and techniques for low and ultra–low temperature experiments. A successful development have been dry mK-systems that can be operated without liquid helium by using a pulse-tube refrigerator for precooling. In the early 2000s, these systems have been successfully commercialized by the company VeriCold Technologies GmbH at Ismaning, Germany, which was taken over by Oxford Instruments in 2007. As further typical examples we mention a nuclear demagnetization cryostat for temperature down to below 100 µK, or very flexible dilution refrigerator inserts for temperatures down to about 20 mK fitting into a 2 inch bore. These systems have been engineered and fabricated at WMI. Within the last years, several dilution refrigerators have been provided to other research groups for various low temperature experiments. WMI also operates a helium liquifier with an annual capacity of above 180.000 liters and supplies both Munich universities with liquid helium. To optimize the transfer of liquid helium into transport containers, WMI has developed a pumping system for liquid helium that is commercialized in collaboration with a company.

To a large extent the research activities of WMI are integrated into national and international research projects such as Clusters of Excellence, Collaborative Research Centers, Research Units, or EU projects. The individual research groups of WMI offer a wide range of attractive research opportunities for bachelor and master students, Ph.D. students and postdoctoral fellows.

Experimental Facilities and Resources

The WMI is equipped with state of the art facilities for the preparation and characterization of superconducting and magnetic materials as well as for various low and ultra–low temperature experiments. The main experimental and technological resources of WMI are listed in the following.

Materials Preparation and Fabrication of Nanostructures

- Laser Molecular Beam Epitaxy (L-MBE) system for oxide heterostructures (equipped with in–situ RHEED, Omicron AFM/STM system, atomic oxygen/nitrogen source, infrared-laser heating system, metallization)
- molecular beam epitaxy (MBE) system for metallic systems
- UHV magnetron sputtering systems for metals (e.g. Nb, Al, NiPd, ...)
- magnetron sputtering system for oxide heteroepitaxy (equipped with four sputtering guns and an oxygen ion gun)
- reactive ion etching (RIE) system, Plasmalab 80 Plus with ICP plasma source, Oxford Instruments Plasma Technology
- ion beam etching (IBE) system equipped with a LN_2 cooled sample holder
- polishing machine for substrate preparation
- ultrasonic bonding machine
- 50 m^2 class 1000 clean room facility
- optical lithography (Süss maskaligner MJB 3 and projection lithography)
- 100 kV nB5 Electron Beam Lithography System by NanoBeam Limited, UK, with 6 inch laser stage
- four-mirror image furnace for crystal growth

Characterization

- 2–circle x–ray diffractometer (Bruker D8 Advance, sample temperature up to 1 600°C)
- high resolution 4–circle x–ray diffractometer with Göbel mirror and Ge monochromator (Bruker D8 Discover)
- Philips XL 30 SFEG scanning electron microscope with EDX analysis
- UHV room temperature AFM/STM system
- 2048 u high resolution mass spectrometer (Fa. Pfeiffer, cross-beam ion source, SEM)
- Low Energy Electron Diffraction (SPECTA-LEED, Fa. Omicron)
- two Raman spectroscopy systems (1.5 to 300 K, in-situ sample preparation)
- SQUID magnetometer (Quantum Design, 1.5 to 700 K, up to 7 T)
- several high field magnet systems (up to 17 T Tesla) with variable temperature inserts
- 7 T split coil magnet systems with optical access and variable temperature insert
- 3D vector magnet (2/2/6 Tesla) with variable temperature inserts
- experimental set–ups for the measurement of noise including low noise SQUID amplifiers and signal analyzers
- high-frequency network analyzers (up to 40 GHz) and various microwave components (sources, mixers, circulators, attenuators) for the determination of high frequency parameters
- ultra-sensitive microwave receiver for state tomography of quantum microwaves (dual path method with FPGA signal processing)
- high-frequency cryogenic probing station (up to 20 GHz, $T > 4$ K)
- magnetooptical Kerr effect (MOKE) system
- ferromagnetic resonance (FMR) system

Low temperature systems and techniques

- several ^{3}He/^{4}He dilution refrigerator inserts for temperatures down to 10 mK
- "dry" mK-cooler based on a dilution refrigerator with pulse-tube precooling and equipped with a large number of microwave lines and cold electronics (e.g. amplifiers, circulators, attenuators) for ultra-sensitive experiments on solid state quantum systems

- "dry" dilution refrigerator with a base temperature of about 10 mK equipped with a 3D vector magnet (1/1/6 Tesla)
- ultra–low temperature facility for temperatures down to below 100 µK based on a nuclear demagnetization cryostat
- experimental set–ups for the measurement of specific heat, magnetization, thermal expansion as well as electrical and thermal transport properties as a function of temperature, magnetic field and pressure

Joint Research Projects

nim
nanosystems initiative munich

SFB 631

TRR 80

QED
CIRCUIT AND CAVITY
QUANTUM ELECTRODYNAMICS

PROMISCE

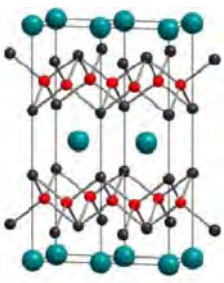

SPP 1458

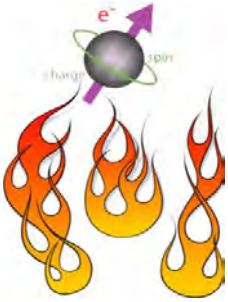

SPP 1538

The Cluster of Excellence "Nanosystems Initiative Munich – NIM"

Rudolf Gross, Frank Deppe, Sebastian T.B. Gönnenwein, Hans Hübl, Achim Marx[1]

The excellence cluster ***Nanosystems Initiative Munich (NIM)*** is one of the key coordinated research projects of Walther-Meißner-Institute (WMI). NIM comprises internationally recognized expertise in all relevant research areas of nanosciences, ranging from quantum nanophysics to the creation and study of nanosystems for biophysics and the life sciences. It joins research groups from LMU Munich, TU Munich, WMI, the University of Augsburg, the Munich University of Applied Science, the Max-Planck-Institutes for Biochemistry and Quantum Optics, and the German Science Museum. WMI is a founding member of NIM and significantly contributes to NIM's overall scientific vision to integrate nanometer sized building blocks as well as bio-molecular assemblies into entire functional systems.

After a successful first funding period (2006 – 2012), a second five-year funding period (2012 – 2017) was granted. For this second funding period, NIM's research activities are organized in five research areas (RAs): RA I – ***Quantum Nanophysics***, RA II – ***Hybrid Nanosystems***, RA III – ***Nanosystems for Energy Conversion***, RA IV – ***Biomolecular Nanosystems***, and RA V – ***Biomedical Nanotechnologies***. The major contributions of WMI are to RA I: ***Quantum Nanophysics*** and RA II: ***Hybrid Nanosystems***. Research area I is coordinated by R. Gross of WMI. At WMI, several scientists (Deppe, Gönnenwein, Gross, Hübl, Marx) actively contribute to the ambitious research program of NIM. In 2014, Frank Deppe has been appointed associate member and Hans Hübl became principal investigator of NIM. Several Ph.D. students of WMI are members of the NIM Graduate School.

In 2014, WMI was particularly profiting from NIM. Substantial financial support of NIM allowed us to replace our old electron beam writer, which has been a key instrument for the fabrication of solid state nanostructures. Superconducting quantum bits and quantum circuits, electro-nanomechanical devices or magnetic nanostructures are at the core of our NIM related research projects. Our previous electron beam lithography system based on a FEI electron beam microscope XL30 SFEG and a Raith Elphy Plus lithography unit served as central facility to define lateral nanostructures since 2000. However, over the past years both the demands for writing time and the technological requirements (structure size, write field size, write field alignment, writing speed, throughput, reliability) have strongly increased because of the growing number of research projects based on the availability of respective nanostructures. Therefore, the replacement of the old electron beam writer by a state-of-the-art electron beam lithography systems was overdue. The new 100 kV nB5 Electron Beam Lithography System of NanoBeam Ltd., UK, with total cost exceeding 1 Mio. Euro has been delivered in October 2014. Meanwhile the systems is installed inside the WMI clean room facility and is fully operational (see report

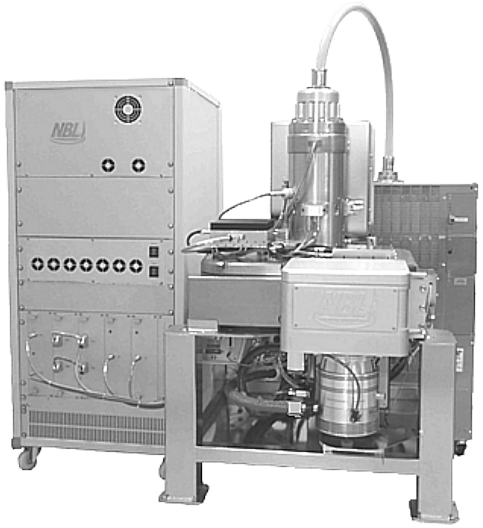

Figure 1: Photograph of the nB5 electron beam lithography system.

[1]This work is supported by the German Excellence Initiative via the Nanosystems Initiative Munich (NIM).

on page 71). With this powerful instrument WMI has significantly improved its technological capabilities for nanofabrication.

The research activities of WMI strongly profit from NIM. Some of our key results are presented in the subsequent reports. They range from the field of superconducting quantum circuits [1–9], hybrid quantum systems [10, 11], electro-nanomechanical systems [12–16], to spin dynamics, spin caloritronics and the study of physics related to pure spin currents [17–23].

Besides the support of young scientists a particular goal of NIM is to provide seed funding for new research directions and to help to establish new coordinated research efforts. To this end, the year 2014 was quite successful. Several NIM PIs provided significant support in setting up the following new projects and networks:

(i) Ph.D. School of Excellence "Exploring Quantum Matter (ExQM)"

In order to unite the unique competences in quantum physics in Munich and extend them into an international excellence network of doctoral training centres with partners at the Austrian Academy of Sciences in Vienna and Innsbruck, at ETH Zurich, ICFO Barcelona, Imperial College London, Caltech, and Harvard, the International Ph.D. School of Excellence (IDK) entitled ***"Exploring Quantum Matter (ExQM)"*** was founded within the Elite-Netzwerk Bayern early in 2014. The participating institutions are the Technical University of Munich (TUM), the Ludwig-Maximilians University of Munich (LMU), the Max-Planck Institute for Quantum Optics (MPQ), and the Walther-Meißner-Institute of BAdW. The research topics of ExQM include (i) quantum simulation of many-body systems, (ii) quantum phase transitions, (iii) open quantum systems, (iv) cavity an circuit QED, and (v) numerical and tensor methods. The training of Ph.D. students is supported by the development of new-media tools tailored to research requirements (e.g. visualization, outreach, interaction with partners).

A particular focus of WMI within ExQM is ***"Scalable networks of solid-state quantum circuits"***, which are becoming increasingly attractive for quantum simulations. For example, networks of nonlinear superconducting transmission line resonators or optical nanocavities can be used as scalable quantum simulators for the Bose-Hubbard Hamiltonian. The resonators are made nonlinear by a controllable coupling to superconducting or semiconductor quantum bits, thereby forming harmonic oscillators with tunable Kerr nonlinearity. Networks of these entities would be particularly well suited for accessing the strongly correlated regime and for investigating quantum many-body dynamics of interacting particles under the influence of driving and dissipation. Solid state quantum circuits with multiple drives are another attracting system (e.g. superconducting quantum bits strongly coupled to a resonator field mode and subjected to multiple classical drives can be used for quantum simulations of relativistic quantum physics such as the dynamics of the Dirac equation).

(ii) Munich Quantum Center (MQC)

Since decades, the Munich area is hosting a large number of institutions and researchers playing a leading role in the study of quantum physics. Based on this long tradition and vivid atmosphere, the Munich Quantum Center (MQC) was founded in 2014. MQC is gathering 21 research groups belonging to different institutions, including the Ludwig-Maximilians University of Munich (LMU), the Technical University of Munich (TUM), the Max-Planck Institute for Quantum Optics (MPQ) and the Walther-Meißner-Institute (WMI). MQC aims to provide

a unique platform to communicate advances and developments achieved in our teams, thus reflecting and stressing the coherence and common points and directions existing behind our research activity.

The MQC member institutions cover a large variety of topics ranging from mathematical foundations, quantum information, computational methods, quantum nanosystems, quantum optics, and quantum many-body physics to superconducting devices. In MQC, mathematicians and theoretical and experimental physicists analyze physical systems exhibiting intriguing quantum mechanical properties and design new methods for leveraging and controlling such systems, thus paving the way for the development of quantum technologies.

References

[1] A. Baust, E. Hoffmann, M. Haeberlein, M. J. Schwarz, P. Eder, E. P. Menzel, K. Fedorov, J. Goetz, F. Wulschner, E. Xie, L. Zhong, F. Quijandria, B. Peropadre, D. Zueco, J.-J. Garcia Ripoll, E. Solano, F. Deppe, A. Marx, and R. Gross (2014). arXiv:1405.1969.

[2] G. Reithmaier, F. Flassig, P. Hasch, S. Lichtmannecker, K. Müller, J. VučkoviÄĞ, R. Gross, M. Kaniber, and J. J. Finley, Applied Physics Letters **105**, – (2014).

[3] R. D. Candia, E. P. Menzel, L. Zhong, F. Deppe, A. Marx, R. Gross, and E. Solano, New Journal of Physics **16**, 015001 (2014).

[4] M. Fischer. *On-chip Superconducting Microwave Interferometer*. Master thesis, TU München (2014).

[5] C. M. F. Schneider. *On-chip Superconducting Beam Splitter*. Master thesis, TU München (2014).

[6] F. Deppe. *Microwave quantum science with superconducting circuits*. Habilitation thesis, TU München (2014).

[7] M. J. Schwarz. *Gradiometric tunable-gap flux qubits in a circuit QED architecture*. Ph.D. thesis, TU München (2015).

[8] L. Zhong, E. P. Menzel, R. D. Candia, P. Eder, M. Ihmig, A. Baust, M. Haeberlein, E. Hoffmann, K. Inomata, T. Yamamoto, Y. Nakamura, E. Solano, F. Deppe, A. Marx, and R. Gross, New Journal of Physics **15**, 125013 (2013).

[9] E. Menzel, R. Di Candia, F. Deppe, P. Eder, L. Zhong, M. Ihmig, M. Haeberlein, A. Baust, E. Hoffmann, D. Ballester, K. Inomata, T. Yamamoto, Y. Nakamura, E. Solano, A. Marx, and R. Gross, Phys. Rev. Lett. **109**, 250502 (2012).

[10] F. Hoehne, C. Huck, M. S. Brandt, and H. Huebl, Phys. Rev. B **89**, 161305 (2014).

[11] H. Huebl, C. W. Zollitsch, J. Lotze, F. Hocke, M. Greifenstein, A. Marx, R. Gross, and S. T. B. Goennenwein, Phys. Rev. Lett. **111**, 127003 (2013).

[12] M. Pernpeintner, T. Faust, F. Hocke, J. P. Kotthaus, E. M. Weig, H. Huebl, and R. Gross, Appl. Phys. Lett. **105**, 123106 (2014).

[13] F. Hocke, M. Pernpeintner, X. Zhou, A. Schliesser, T. J. Kippenberg, H. Huebl, and R. Gross, Applied Physics Letters **105**, – (2014).

[14] F. Hocke. *Microwave Circuit-electrodynamics in a Nanomechanical Hybrid System*. Dissertation, Technische Universität München (2013).

[15] X. Zhou, F. Hocke, A. Schliesser, A. Marx, H. Huebl, R. Gross, and T. J. Kippenberg, Nat. Phys. **9**, 179 (2013).

[16] F. Hocke, X. Zhou, A. Schliesser, T. J. Kippenberg, H. Huebl, and R. Gross, New J. Phys. **14**, 123037 (2012).

[17] J. Lotze, H. Huebl, R. Gross, and S. T. B. Goennenwein, Phys. Rev. B **90**, 174419 (2014).

[18] A. Kamra, F. P. Witek, S. Meyer, H. Huebl, S. Geprägs, R. Gross, G. E. W. Bauer, and S. T. B. Goennenwein, Phys. Rev. B **90**, 214419 (2014).

[19] N. Roschewsky, M. Schreier, A. Kamra, F. Schade, K. Ganzhorn, S. Meyer, H. Huebl, S. Geprägs, R. Gross, and S. T. B. Goennenwein, Appl. Phys. Lett. **104**, 202410 (2014).

[20] M. Schreier, A. Kamra, M. Weiler, J. Xiao, G. E. W. Bauer, R. Gross, and S. T. B. Goennenwein, Phys. Rev. B **88**, 094410 (2013).

[21] M. Althammer, S. Meyer, H. Nakayama, M. Schreier, S. Altmannshofer, M. Weiler, H. Huebl, S. Geprägs, M. Opel, R. Gross, D. Meier, C. Klewe, T. Kuschel, J.-M. Schmalhorst, G. Reiss, L. Shen, A. Gupta, Y.-T. Chen, G. E. W. Bauer, E. Saitoh, and S. T. B. Goennenwein, Phys. Rev. B **87**, 224401 (2013).

[22] Y.-T. Chen, S. Takahashi, H. Nakayama, M. Althammer, S. T. B. Goennenwein, E. Saitoh, and G. E. W. Bauer, Phys. Rev. B **87**, 144411 (2013).

[23] H. Nakayama, M. Althammer, Y.-T. Chen, K. Uchida, Y. Kajiwara, D. Kikuchi, T. Ohtani, S. Geprägs, M. Opel, S. Takahashi, R. Gross, G. E. W. Bauer, S. T. B. Goennenwein, and E. Saitoh, Phys. Rev. Lett. **110**, 206601 (2013).

The Collaborative Research Center 631

Rudolf Gross, Frank Deppe, Hans Hübl, Achim Marx[1]

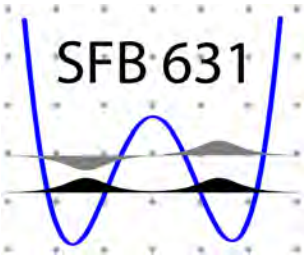

The ***Collaborative Research Center 631*** on "Solid State Quantum Information Processing" was established in 2003 and extended for a second and a third four-year funding period in 2007 and 2011, respectively. Since the start of CRC 631 more than a decade ago, quantum information science has developed into a fascinating and one of the most rapidly growing fields of science and technology, joining scientists from physics, mathematics, computer and materials science, and engineering. It is concerned with both fundamental questions and technological developments, aiming at the realization of a useful quantum information hardware. The third funding period of the highly successful CRC 631 will end in June 2015. It was providing the basis for several subsequent research projects, including the excellence cluster *Nanosystems Initiative Munich (NIM)*, the EU projects *"Quantum Propagating Microwaves in Strongly Coupled Environments – PROMISCE"* and *"Cavity and Circuit Quantum Electrodynamics – CCQED"*, as well as the International Ph.D. School of Excellence (IDK) entitled *"Exploring Quantum Matter (ExQM)"*.

The Walther-Meißner-Institute (WMI) is one of the main actors within CRC 631. WMI is not only involved in the projects on *Superconducting Quantum Circuits as Basic Elements for Quantum Information Processing* (A3: Gross, Hübl, Marx), on *Cavity Quantum Electrodynamics with Superconducting Devices* (A8: Gross, Marx, Deppe) and on *Fundamentals of Quantum Logic Gates in Silicon* (C3: Hübl), but also provides the coordination of the center from the beginning (spokesman: Rudolf Gross). Meanwhile, solid state quantum systems are one of the key research fields of WMI. Besides superconducting quantum bits and quantum circuits, our research activities include also quantum spin and nanomechanical systems, as well as circuits combining different degrees of freedom in hybrid quantum systems. Our research within CRC 631 does not only provide the foundations of quantum information systems and quantum technology, but also addresses key fundamental questions regarding quantum coherence, quantum dynamics and decoherence processes in solid state quantum systems.

The recent scientific and technological achievements of WMI related to CRC 631 are summarized in the reports by

- Wulschner *et al.*: Circuit quantum electrodynamics with transmon qubits, see page 19,
- Deppe *et al.*: Circuit quantum electrodynamics with a gradiometric tunable-gap flux qubits, see page 21,
- Baust *et al.*: Ultrastrong coupling in two-resonator circuit QED, see page 23,
- Zollitsch *et al.*: Coupling phosphorus donors to a superconducting resonator, see page 27,
- Menzel *et al.*: Superconducting on-chip microwave interferometer, see page 53,
- Wulschner *et al.*: Coupling and decoupling of microwave resonators via an RF-SQUID, see page 55,
- Xie *et al.*: Circuit quantum electrodynamics with three-dimensional cavities, see page 58,
- Fedorov *et al.*: Characterization of Josephson parametric amplifiers, see page 60,
- Goetz *et al.*: Characterization of superconducting transmission line resonators, see page 62,

[1]This work is supported by the German Research Foundation through SFB 631.

and therefore will not be further discussed here. Our results range from the fabrication and study of superconducting quantum bits and quantum circuits [1–5], quantum spin systems [6], hybrid quantum systems [7] to the rapidly growing field of quantum microwave communication [8–12]. In these fields the WMI team closely collaborates with the theory groups at the Universidad del País Vasco - Euskal Herriko Unibertsitatea at Bilbao (Solano), the University of Augsburg (Hänggi), and the Instituto de Física Fundamental at Madrid (Garcia-Ripoll), as well as the experimental groups at the NTT Basic Research Laboratories (Semba), the Nanoelectronics Research Laboratories at NEC Corporation, Japan (Tsai, Yamamoto), and the University of Tokyo (Nakamura).

In a fruitful collaboration with the Finley group at Walter Schottky Institute, we deposited NbN thin films by DC magnetron sputtering on [100] GaAs substrates, optimized their quality, and demonstrated their use for efficient single photon detection in the near-infrared [13–15]. Meanwhile the superconducting single photon detectors (SSPDs) have been successfully used for the efficient on-chip time resolved detection of quantum dot emission. Recently, we succeeded in the on-chip generation of quantum light from individual, resonantly excited self-assembled InGaAs quantum dots, their efficient routing over mm length scales via GaAs ridge waveguides and their in-situ detection using evanescently coupled integrated NbN-SSPDs fabricated on the same chip [16].

References

[1] A. Baust, E. Hoffmann, M. Haeberlein, M. J. Schwarz, P. Eder, E. P. Menzel, K. Fedorov, J. Goetz, F. Wulschner, E. Xie, L. Zhong, F. Quijandria, B. Peropadre, D. Zueco, J.-J. Garcia Ripoll, E. Solano, F. Deppe, A. Marx, and R. Gross (2014). arXiv:1405.1969.

[2] F. Deppe. *Microwave quantum science with superconducting circuits*. Habilitation thesis, TU München (2014).

[3] M. J. Schwarz. *Gradiometric tunable-gap flux qubits in a circuit QED architecture*. Ph.d. thesis, TU München (2015).

[4] E. Hoffmann. *Experiments on Two-Resonator Circuit Quantum Electrodynamics: A Superconducting Quantum Switch*. Ph.d. thesis, TU München (2013).

[5] E. P. Menzel. *Propagating Quantum Microwaves: Dual-path State Reconstruction and Path Entanglement*. Ph.d. thesis, TU München (2013).

[6] F. Hoehne, C. Huck, M. S. Brandt, and H. Huebl, Phys. Rev. B **89**, 161305 (2014).

[7] H. Huebl, C. W. Zollitsch, J. Lotze, F. Hocke, M. Greifenstein, A. Marx, R. Gross, and S. T. B. Goennenwein, Phys. Rev. Lett. **111**, 127003 (2013).

[8] R. D. Candia, E. P. Menzel, L. Zhong, F. Deppe, A. Marx, R. Gross, and E. Solano, New Journal of Physics **16**, 015001 (2014).

[9] L. Zhong, E. P. Menzel, R. D. Candia, P. Eder, M. Ihmig, A. Baust, M. Haeberlein, E. Hoffmann, K. Inomata, T. Yamamoto, Y. Nakamura, E. Solano, F. Deppe, A. Marx, and R. Gross, New Journal of Physics **15**, 125013 (2013).

[10] M. Fischer. *On-chip Superconducting Microwave Interferometer*. Master thesis, TU München (2014).

[11] C. M. F. Schneider. *On-chip Superconducting Beam Splitter*. Master thesis, TU München (2014).

[12] E. Menzel, R. Di Candia, F. Deppe, P. Eder, L. Zhong, M. Ihmig, M. Haeberlein, A. Baust, E. Hoffmann, D. Ballester, K. Inomata, T. Yamamoto, Y. Nakamura, E. Solano, A. Marx, and R. Gross, Phys. Rev. Lett. **109**, 250502 (2012).

[13] G. Reithmaier, F. Flassig, P. Hasch, S. Lichtmannecker, K. Müller, J. Vučković, R. Gross, M. Kaniber, and J. J. Finley, Applied Physics Letters **105**, – (2014).

[14] G. Reithmaier, J. Senf, S. Lichtmannecker, T. Reichert, F. Flassig, A. Voss, R. Gross, and J. J. Finley, Journal of Applied Physics **113**, 143507 (2013).

[15] G. Reithmaier, S. Lichtmannecker, T. Reichert, P. Hasch, K. Mueller, M. Bichler, R. Gross, and J. J. Finley, Scientific Reports **3**, – (2013).

[16] G. Reithmaier, M. Kaniber, F. Flassig, S. Lichtmannecker, A. , K. AndrejewMüller, J. Vučković, R. Gross, and J. J. Finley (2014). arXiv:1408.2275.

Basic Research

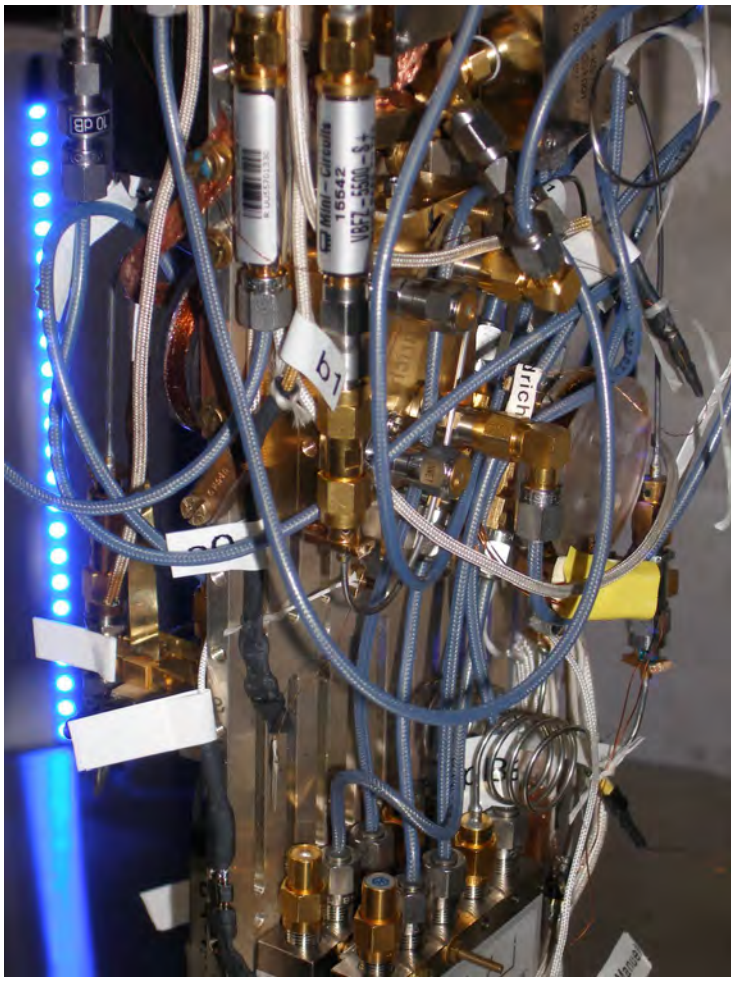

Installation of microwave cables and components on the mK part of a dilution refrigerator system used for experiments on solid state quantum systems.

Circuit quantum electrodynamics with transmon qubits

F. Wulschner, J. Puertas Martinez, E. P. Menzel, F. Deppe, A. Marx, R. Gross[1]

Superconducting quantum bits are basic building blocks for circuit QED systems. Applications in the fields of quantum computation and quantum simulation require long coherence times. We have fabricated and characterized superconducting transmon qubits which are designed to operate at a high ratio of Josephson coupling energy and charging energy. Due to their low sensitivity to charge noise [1] transmon qubits show good coherence properties [2]. A transmon qubit typically consists of a DC-SQUID, which provides a flux tunable nonlinear inductance $L_J(\Phi)$, where Φ is the externally applied flux and a shunt capacitor with capacitance C. The transmon qubit can be described as an anharmonic oscillator with first transition frequency $\omega_q(\Phi) = 1/\sqrt{L_J(\Phi)C}$. This transition frequency usually is designed to be in the order of some gigahertz. Due to the non-linearity of the SQUID inductance higher level transitions are shifted to lower frequencies by some hundred megahertz. When the level line width is much smaller then the anharmonicity of the level spacing, the system can be considered as an effective two level system (qubit). For read-out and manipulation of the transmon qubit, it is routinely coupled to a coplanar waveguide resonator as depicted in Fig. 1. When the qubit transition frequency matches the resonator frequency an avoided level crossing with a level splitting of g/π is obtained.

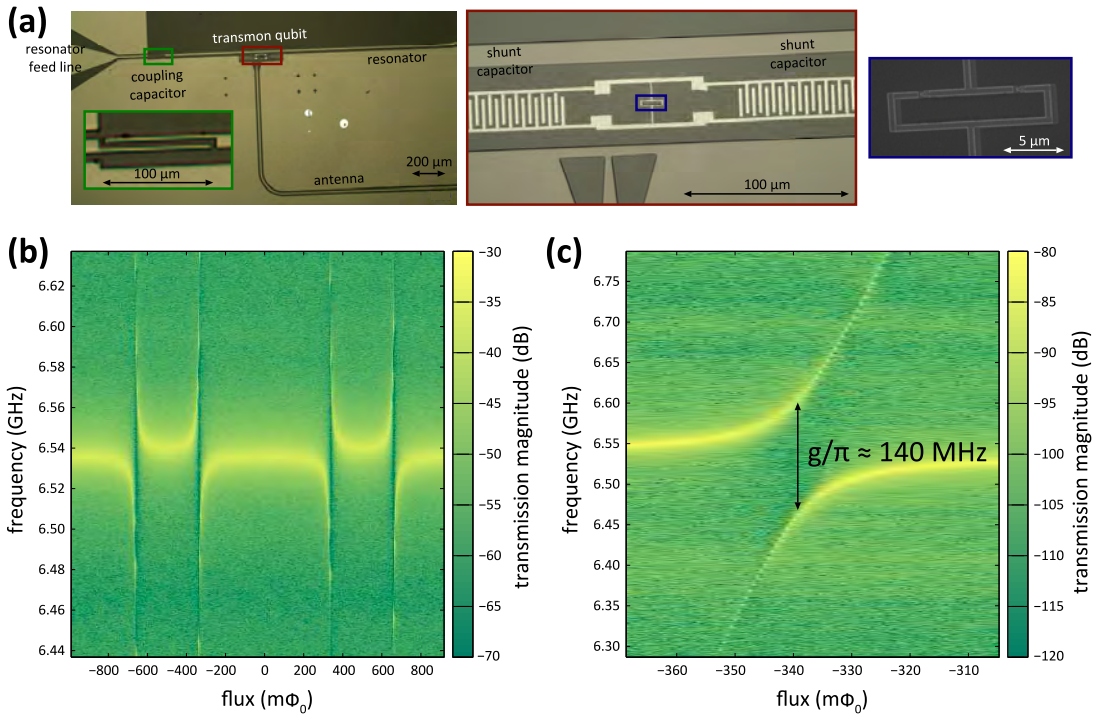

Figure 1: Transmon qubit coupled to a coplanar stripline resonator. (a) Optical micrograph of the sample and scanning electron micrograph of the DC SQUID (right, blue frame). (b) Resonator transmission (color coded) as a function of the applied magnetic flux and probe frequency. (c) Close-up of (b) in the region of an anti-crossing indicating coherent qubit-resonator coupling.

In our experiment we couple the transmon qubit to a coplanar stripline resonator. In contrast to a coplanar waveguide resonator, this resonator type has a ground plane only on one side. The niobium resonator is fabricated on a silicon substrate and has a bare resonance frequency

[1]We acknowledge financial support by the German Research Foundation through SFB 631, the German Excellence Initiative through the Nanosystems Initiative Munich (NIM), and the EU projects CCQED and PROMISCE.

of $\omega_r/2\pi = 6.539\,\text{GHz}$. The transmon qubit is located at a voltage anti-node of the resonator. This allows us to drive the transmon by the electrical field component of the resonator ground mode.

Figure 1(b) shows the transmission magnitude of the resonator-qubit system as a function of the applied flux and probe frequency. The periodicity of the transmission spectrum with the flux quantum Φ_0 is due to the periodic modulation of the SQUID inductance. Figure 1(c) shows a close-up of the anti-crossing region. From this data we extract a qubit-resonator coupling of $g/\pi \simeq 140\,\text{MHz}$. The two well separated peaks in the transmission spectrum confirms the operation of the device in the strong coupling regime.

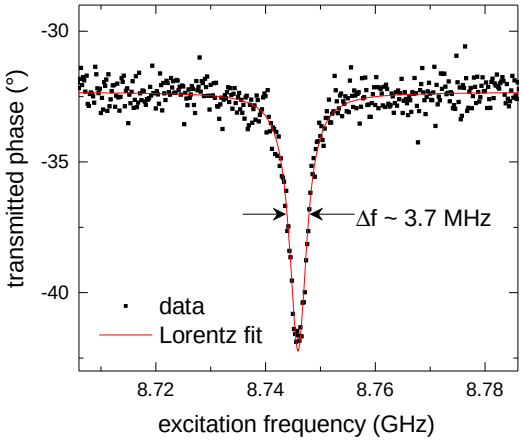

Figure 2: Phase of the resonator transmission depending on the frequency of the qubit excitation tone. When the excitation tone frequency matches the qubit frequency the resonance frequency and the phase shift.

The analysis of the resonator linewidth performed for a large qubit-resonator detuning $\Delta = \omega_r - \omega_q \gg g$ provides information on the qubit coherence time. In this regime, the qubit transition frequency is shifted by the number of cavity photons (Stark shift). Alternatively, the Stark shift can be interpreted as a dispersive shift of the resonator transition frequency depending on the qubit state. Thus, a measurement of the cavity transmission frequency allows to investigate the qubit state. We monitor transmission amplitude and phase of the resonator, because for small excitation amplitude the response scales linearly with the qubit occupation probability. Figure 2 shows the response of the resonator phase depending on the qubit drive frequency. For this data set we find a linewidth $\Delta f = 3.7\,\text{MHz}$, which is much smaller than the measured anharmonicity of 600 MHz (data not shown). Hence, we can safely treat our system as a two-level system. For a second sample with larger transmon qubit capacitance (less sensitive to charge noise) we observe a narrower linewidth of $\Delta f = 740\,\text{kHz}$ (see Fig. 3). From this data we deduce a qubit coherence time of $T_2 = 1/(\pi\Delta f) \simeq 0.43\,\mu\text{s}$.

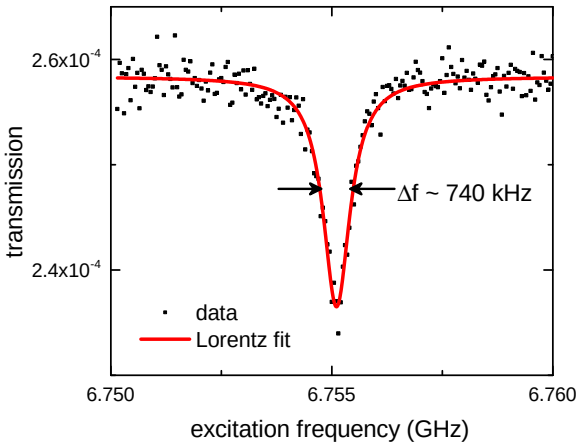

Figure 3: Transmission amplitude of the resonator probe tone depending on the frequency of the qubit excitation tone of a second sample. The linewidth of this sample is reduced to 740 kHz, which we attribute to the larger qubit capacitance.

In conclusion, we have established a transmon qubit fabrication process at WMI and performed qubit spectroscopy. The measured linewidths in the megahertz range are a promising starting point for time domain spectroscopy experiments.

References

[1] J. Koch, T. M. Yu, J. Gambetta, A. A. Houck, D. I. Schuster, J. Majer, A. Blais, M. H. Devoret, S. M. Girvin, and R. J. Schoelkopf, Phys. Rev. A **76**, 042319 (2007).

[2] J. A. Schreier, A. A. Houck, J. Koch, D. I. Schuster, B. R. Johnson, J. M. Chow, J. M. Gambetta, J. Majer, L. Frunzio, M. H. Devoret, S. M. Girvin, and R. J. Schoelkopf, Phys. Rev. B **77**, 180502 (2008).

Circuit quantum electrodynamics with a gradiometric tunable-gap flux qubit

F. Deppe, M. J. Schwarz, J. Goetz, M. Haeberlein, A Marx, R. Gross [1]

In circuit quantum electrodynamics or quantum simulation experiments, superconducting quantum bits must combine good coherence with high in situ tunability. Often, a large anharmonicity is also desirable. Other than the poplar transmon qubit, the gradiometric tunable-gap flux qubit meets all three of these requirements. In previous publications [1] and annual reports [2], we characterized such a qubit via a DC superconducting quantum interference device (SQUID) readout, finding a tunability of several gigahertz of the qubit transition frequency at the point of optimum phase coherence. Here, we demonstrate the first implementation of a gradiometric tunable-gap flux qubit into a transmission line resonator.

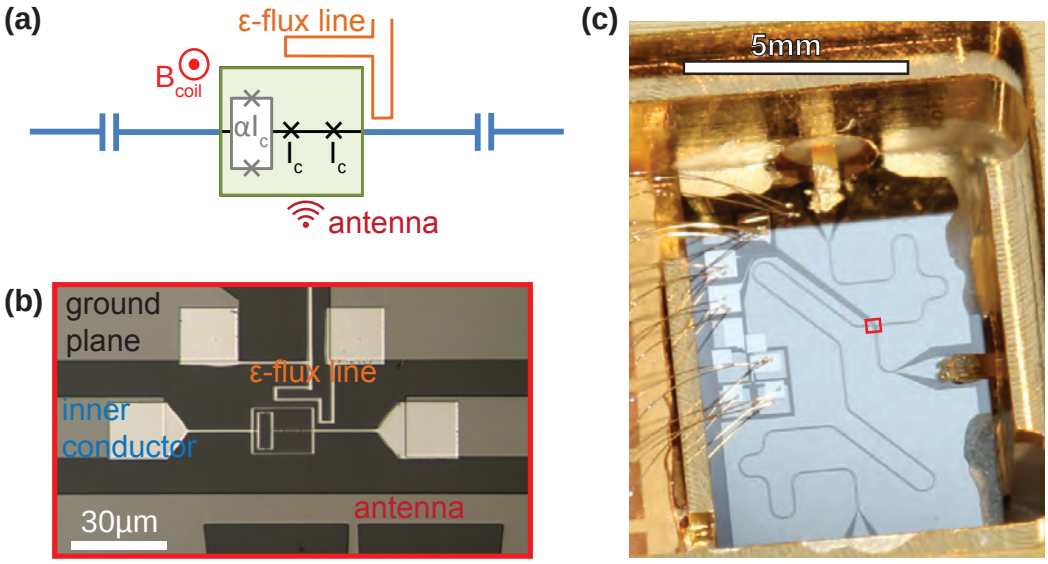

Figure 1: Gradiometric tunable-gap flux qubit coupled to a coplanar waveguide resonator. Graph taken from Ref. [3]. (a) Schematic sample layout. (b) Optical micrograph of the sample. (c) Photograph of the sample chip inside the gold-plated copper sample holder.

The sample layout is shown in Fig. 1. Our geometric tuable-gap flux qubit has the same geometry as the one discussed in Ref. [1] and Ref [2] and is fabricated with aluminum technology and shadow evaporation. We connect this qubit galvanically to the center conductor of a niobium coplanar waveguide transmission line resonator. The qubit is located at 1/4 of the resonator length, i.e., it couples significantly to the lowest three current modes but is decoupled from the fourth. Although the asymmetric ϵ-flux line shown in Fig. 1(a) works perfectly fine, we conveniently change the flux bias with the external coil for this sample because the gradiometer quality is only on the order of 10.

The qubit gap is tuned by varying the flux through the α-SQUID shown in Fig. 1(a) and Fig. 1(b) via the external coil. Typical transmission spectroscopy data for two different qubit gaps ($\Delta/h \simeq 5.52\,\mathrm{GHz}$ and $\Delta/h \simeq 3.54\,\mathrm{GHz}$) are shown in Fig. 2. We clearly see anticrossing-like structures when the qubit hyperbola intersects a resonator mode. Else, a flux-dependent dispersive shift is observed. Typical coupling strengths are, as expected, in the order of

[1] We acknowledge financial support by the German Research Foundation through SFB 631, the German Excellence Initiative through the Nanosystems Initiative Munich (NIM), and the EU projects CCQED and PROMISCE.

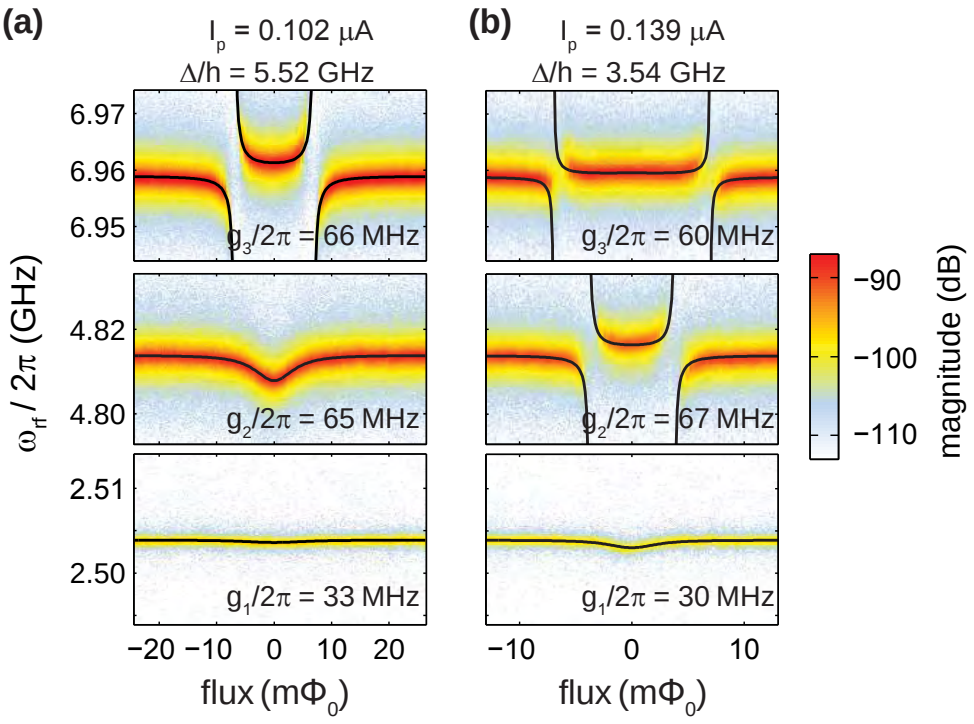

Figure 2: Continuous-wave spectroscopy of the tunable-gap gradiometric flux qubit coupled to a coplanar waveguide resonator. Graph modified from Ref. [4]. (a) Resonator transmission (color code) as a function of probe frequency ω_{rf} and the deviation of the applied flux from $\Phi_0/2$ for the three lowest modes and $\Delta/h \simeq 5.5\,\mathrm{GHz}$. (b) As (c), but for $\Delta/h \simeq 3.6\,\mathrm{GHz}$.

60 MHz. All in all, we find that we can tune the qubit gap frequency between unmeasurably small values and 5.6 GHz, which corresponds to the range $0.55 \leq \alpha \leq 1.05$. We attribute the fact that we do not reach $\alpha = 0.5$ and the limited gradiometer quality to an asymmetric α-SQUID, where the two junctions have noticeably different critical currents.

Finally, we perform first time-domain experiments on the qubit at the operation point $\omega_{\mathrm{q}}/2\pi = \Delta/h \simeq 5.5\,\mathrm{GHz}$. We find $T_1 \simeq 300\,\mathrm{ns}$ (data not shown, see Ref. [3] and Ref. [4]). The shorter Rabi decay times of approximately 100 ns indicate a dephasing-limited situation. In conclusion, we successfully demonstrate the operation of a tunable-gap gradiometric flux qubit in a circuit QED architechture in frequency and time domain.

References

[1] M. J. Schwarz, J. Goetz, Z. Jiang, T. Niemczyk, F. Deppe, A. Marx, and R. Gross, New J. Phys. **15**, 045001 (2013).
[2] M. J. Schwarz, J. Goetz, Z. Jiang, F. Deppe, A. Marx, and R. Gross, WMI Ann. Rep. **2012**, 75–76 (2012).
[3] M. J. Schwarz. *Gradiometric tunable-gap flux qubits in a circuit QED architecture*. Ph.D. thesis, Technische Universität München (2015).
[4] F. Deppe. *Microwave quantum science with superconducting circuits*. Habilitationsschrift, Technische Universität München (2014).

Ultrastrong coupling in two-resonator circuit QED

A. Baust, E. Hoffmann, M. Haeberlein, P. Eder, E. Menzel, F. Deppe, A. Marx, R. Gross[1]
D. Zueco[2], *J.-J. Garcia-Ripoll*[3], *L. García-Álvarez, G. Romero, E. Solano*[4]

Circuit quantum electrodynamics (QED) [1] has not only become a versatile toolbox for quantum information processing, but is also a powerful platform for the investigation of light-matter interaction. In contrast to the field of cavity QED, where the interaction between atoms and the light field confined in a three-dimensional optical cavity is studied, the building blocks of the circuit QED architecture are quantum bits acting as 'artificial atoms' and quasi-one-dimensional superconducting transmission line resonators. Since the mode volumes of the latter are small compared to those of three-dimensional optical cavities and the dipole moments of the artificial atoms are orders of magnitude larger compared to those of their natural counterparts, the coupling energies between atom and light field obtained in circuit QED setups can become a significant fraction of the system energy. Remarkably, even the regime of ultrastrong coupling can be reached where the Jaynes-Cummings approximation breaks down and the interaction between light and matter can only be described correctly by the quantum Rabi model which takes the counterrotating terms into account [2].

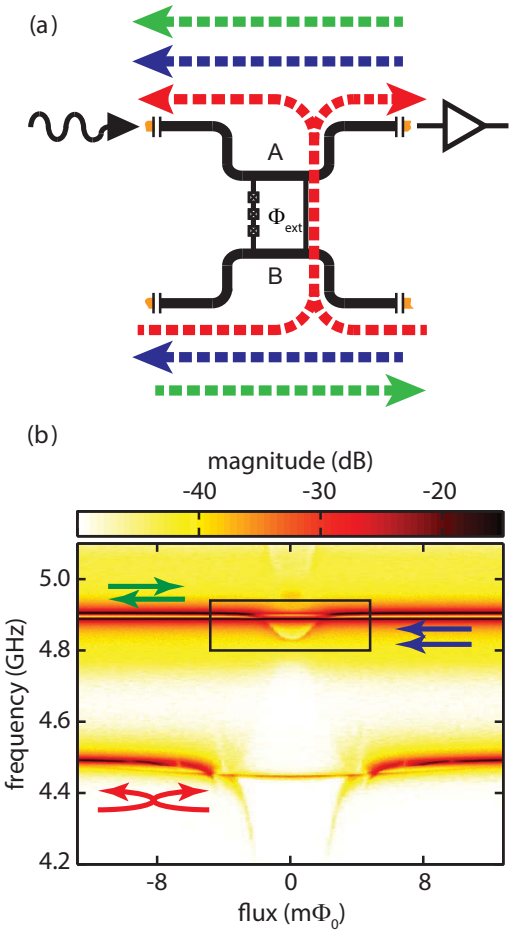

Figure 1: (a) Measurement setup. The blue (green) dashed lines symbolize the parallel (antiparallel) modes. The red lines symbolize the mode going across the qubit arm without Josephson junctions. (b) Transmission measured through one resonator. The three resonant modes are identified with the modes shown in (a).

We investigate a circuit QED system consisting of two coplanar stripline resonators, A and B, with fundamental mode frequencies $\omega_R = 4.896\,\mathrm{GHz}$ and a three Josephson junction flux qubit coupled galvanically to the signal lines of both resonators, cf. Fig. 1(a) and Ref. [3]. We mount the sample inside a gold plated copper box to the base temperature stage of a dilution refrigerator. For both resonators, one port each is connected to a highly attenuated input line and the respective second port is connected to an output line featuring circulators and cryogenic and room temperature amplifiers.

We measure the transmission through one of the two resonators depending on the magnetic flux applied to the qubit loop using a vector network analyzer. The results are shown in Fig. 1(b). Three resonant modes are observed. We identify the modes at 4.888 GHz and 4.905 GHz with the parallel and antiparallel modes as shown in Fig. 1(a). An additional

[1]We acknowledge financial support by the German Research Foundation through SFB 631, the German Excellence Initiative through the Nanosystems Initiative Munich (NIM), and the EU projects CCQED and PROMISCE.
[2]CSIC-Universidad de Zaragoza, Spain.
[3]Instituto de Física Fundamental-CSIC, Madrid, Spain
[4]Universidad del Pais Vasco UPV/EHU and Ikerbasque, Spain.

mode (denoted u) is found at 4.50 GHz which can be explained by parallel oscillations across the qubit. The mode current flows predominantly along the qubit arm without Josephson junctions, cf. Fig. 1(a). The large kinetic inductance of the latter yields a very high coupling strength of the mode u to the qubit.

To perform a quantitative analysis, we fit the eigenmodes of the Hamiltonian to the spectroscopy data, taking into account the coupling of all three modes to the qubit and the mutual resonator-resonator coupling. For the mode u, we find that the ratio between coupling strength and frequency, the *relative coupling strength*, reaches 15 %. Remarkably, this value exceeds the coupling strengths observed in Ref. [2] even though the coupling in our scenario is determined solely by the geometrical properties of the qubit arm and no additional element such as a Josephson junction is used to enhance the coupling.

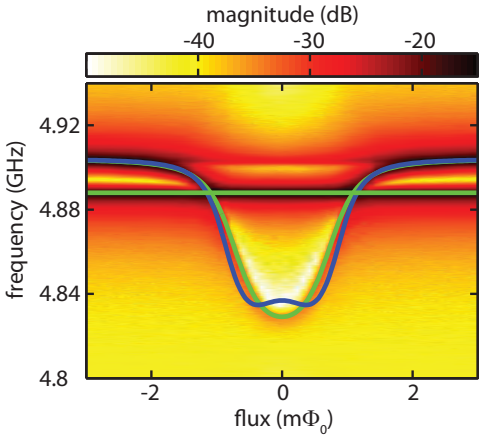

Figure 2: Breakdown of the Jaynes-Cummings model. Green lines: Fit of the full (Rabi) Hamiltonian to the data. Blue line: Prediction by the Jaynes-Cummings model.

In Fig. 2 we present a detailed view of the transmission spectrum from Fig. 1(b) (black rectangle). As can be seen, the data and the theoretical description by the full (Rabi) Hamiltonian (green lines) agree very well. Contrarily, the blue line shows the mode spectrum as expected from the Jaynes-Cummings approximation where the counterrotating terms $\sigma_+ u^\dagger$ and $\sigma_- u$ with the qubit ladder operators σ_+ and σ_- and the mode creation (annihilation) operators $u^\dagger$ (u) are neglected. A pronounced qualitative deviation of the spectroscopy data from the Jaynes-Cummings model is clearly observed. Consequently, this confirms that the counterrotating terms cannot be neglected and that the regime of ultrastrong coupling between the mode u and the qubit is reached. The discrepancy between the description of the data in the scope of the Rabi and the Jaynes-Cummings model is in good qualitative agreement with the observation of the Bloch-Siegert-shift in a system comprised of a four Josephson junction flux qubit coupled to an LC-resonator [4].

In conclusion, we observe physics beyond the Jaynes-Cummings model in a circuit QED architecture comprised of a flux qubit galvanically coupled to two resonators. Our findings demonstrate that ultrastrong coupling can be reached without using the inductance of an additional coupling Josephson junction. In future experiments, a further increase of the coupling strength may give access to the regime of *deep strong coupling*, where the relative coupling strength exceeds unity and new effects such as finite photon population of the ground state will give even deeper insight into the physics of light-matter interaction.

References

[1] A. Wallraff, D. I. Schuster, A. Blais, L. Frunzio, R.-S. Huang, J. Majer, S. Kumar, S. M. Girvin, and R. J. Schoelkopf, Nature **431**, 162–167 (2004).

[2] T. Niemczyk, F. Deppe, H. Huebl, E. P. Menzel, F. Hocke, M. J. Schwarz, J. J. Garcia-Ripoll, D. Zueco, T. Hümmer, E. Solano, A. Marx, and R. Gross, Nature Phys. **6**, 772–776 (2010).

[3] A. Baust, E. Hoffmann, M. Haeberlein, M. J. Schwarz, P. Eder, E. P. Menzel, K. Fedorov, J. Goetz, F. Wulschner, E. Xie, L. Zhong, F. Quijandria, B. Peropadre, D. Zueco, J.-J. Garcia Ripoll, E. Solano, F. Deppe, A. Marx, and R. Gross (2014). arXiv:1405.1969.

[4] P. Forn-Diaz, J. Lisenfeld, D. Marcos, J. J. Garcia-Ripoll, E. Solano, C. J. P. M. Harmans, and J. E. Mooij, Phys. Rev. Lett. **105**, 237001 (2010).

Circuit electromechanics with a non-metalized nanobeam

M. Pernpeintner, F. Hocke, R. Gross, H. Huebl [1]
T. Faust, J. P. Kotthaus [2], *E. M. Weig* [3]

In the field of cavity optomechanics, micro- or nanoscale mechanical resonators are coupled to an optical cavity allowing to transfer information from the mechanical to the optical domain and vice versa [1]. Transferring this approach from the optical to the microwave regime gives rise to the field of circuit electro-nanomechanics [2]. Here, typically metallized mechanical resonators are capacitively coupled to superconducting microwave resonators enabling e. g. ground state cooling [3] or the control of microwave signals [4]. Complementary, the integration of insulating material systems is expected to improve the mechanical quality factors as additional dissipation stemming from the metallization of the mechanical resonator becomes suppressed. To this end, the dielectric coupling of non-metallized Si_3N_4 nanoresonators has been established as an alternative transduction and control scheme for high-Q nano-electromechanical systems in recent years [5]. Here, we demonstrate an integrated electro-nanomechanical system where a doubly-clamped, highly tensile-stressed Si_3N_4 nanobeam is dielectrically coupled to a $\lambda/2$ superconducting niobium microwave resonator. The $l = 20\,\mu m$ long and $w = 170\,nm$ wide nanobeam is located between the niobium centerline and the ground plane with a gap of 150 nm between beam and electrodes, as shown in Figs. 1(a)-(c). For sample fabrication, we use several e-beam lithography steps as well as reactive ion etching and thin film deposition via magnetron sputtering. Finally, we release the beam using a buffered hydroflouric acid etching step.

To experimentally characterize the electro-nanomechanical hybrid system, we employ the homodyne measurement setup depicted in Fig. 1(d). The microwave resonator is driven by a microwave source at its resonance frequency $\omega_c/2\pi$. The sample is mounted on a piezoelectric actuator driven by the output of a vector network analyzer (VNA). This allows us to excite the fundamental flexural out-of-plane mode of the nanobeam to a high amplitude state. For phase sensitive detection with the VNA, the output microwave signal is down-converted using an I-Q-demodulator.

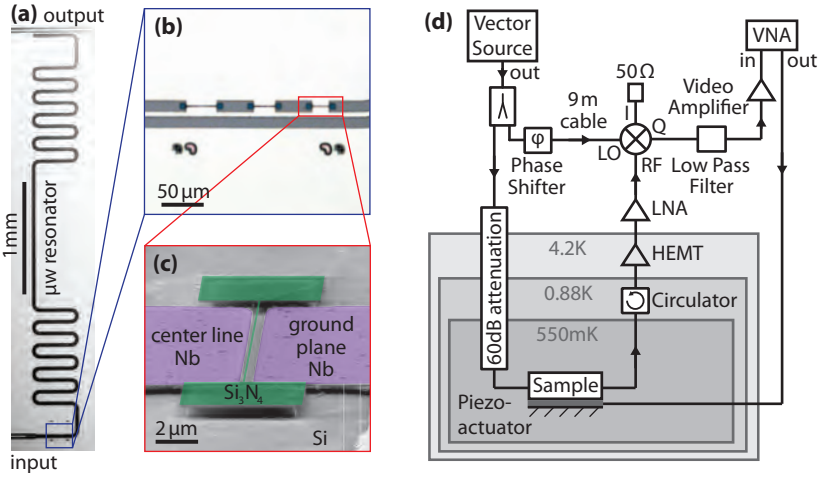

Figure 1: (a)-(c) Optical micrograph and false color scanning electron micrograph of the nano-electromechanical hybrid sample. (d) Measurement setup.

When driving the microwave cavity and the beam simultaneously, the microwave drive tone with frequency $\omega_d/2\pi$ is modulated by the beam's motion, resulting in the generation of sidebands at $\omega_d \pm \Omega_m$. For low drive power, the nanobeam follows the behavior expected for a harmonic oscillator. The measured quality factor of $Q = 480{,}000$ at $T \simeq 550\,mK$ exceeds those

[1] Financial support by the Excellence Cluster Nanosystems Initiative Munich (NIM) is gratefully acknowledged.
[2] Center for NanoScience and Fakultät für Physik, Ludwig-Maximilians-Universität, München, Germany
[3] Center for NanoScience and Fakultät für Physik, Ludwig-Maximilians-Universität, München, Germany and Department of Physics, University of Konstanz, Konstanz, Germany

of comparable nanobeams with Nb metallization [6] by more than a factor of three. Upon increasing the drive power, nonlinear effects modify the dynamics of the beam, leading to the Duffing equation of motion. Hereby, the nonlinearity can be calculated from the material parameters of the beam [7]. The resulting amplitude spectrum shows a characteristic sharkfin-like shape as shown in Fig. 2(a). Upon increasing drive power, the maximum of the amplitude spectrum shifts to higher frequencies. This behaviour is described by the so-called backbone curve $x_{0,\mathrm{max}}^2 = (8\Omega_\mathrm{m}/3\alpha)(\Omega_\mathrm{eff} - \Omega_\mathrm{m})$ [8]. As a consequence, we can relate the amplitude x_0 of the beam to spectral information, which is straightforwardly accessible.

To relate the measured sideband signal P_hom to the vibrational amplitude x_0 of the beam, we use frequency noise calibration, which allows us to determine the transfer function $K(\Omega) = P_\mathrm{hom}\Omega^2/(G^2 x_0^2)$. Here, G denotes the electromechanical coupling. Using literature material parameters, we obtain $G/2\pi = 312\,\mathrm{Hz/nm}$ and an electromechanical vacuum coupling of $g_0/2\pi = 11.5\,\mathrm{mHz}$. Compared to similar nano-electromechanical hybrid systems with metallized beams (see, e.g., [4]), the coupling is about two orders of magnitude smaller, as it solely relies on the dielectric interaction between nanobeam and niobium electrodes. Comparing the experimentally determined coupling constant with finite element based model calculations shows good quantitative agreement (for further details see [9]).

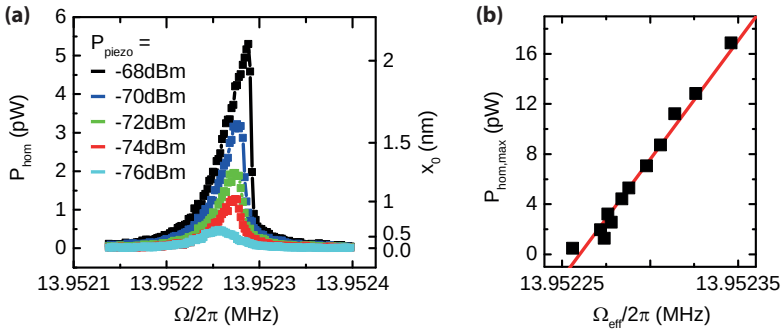

Figure 2: (a) Homodyne power spectrum (left axis) resp. mechanical amplitude spectrum (right axis) of the nanobeam for varying external drive power. (b) Maximum homodyne power as a function of the effective resonance frequency (the so-called backbone curve).

This work opens the path for further studies of mechanical losses in silicon nitride at mK temperatures, extending previous work on the damping mechanisms in Si_3N_4 nanobeams [10, 11]. Moreover, the concept of dielectrically coupling a pure Si_3N_4 nanobeam to a high-Q microwave resonator is promising especially for sensing devices, e. g. for the detection of single molecules, which require high frequency resolution and thus low damping constants.

References

[1] M. Aspelmeyer, T. J. Kippenberg, and F. Marquardt (eds.) *Cavity Optomechanics - Nano- and Micromechanical Resonators Interacting with Light* (Springer, Berlin, 2014).
[2] C. A. Regal, J. D. Teufel, and K. W. Lehnert, Nature Phys. **4**, 555 (2008).
[3] J. D. Teufel, D. Li, M. S. Allman, K. Cicak, A. J. Sirois, J. D. Whittaker, and R. W. Simmonds, Nature **471**, 204 (2011).
[4] X. Zhou, F. Hocke, A. Schliesser, A. Marx, H. Huebl, R. Gross, and T. J. Kippenberg, Nature Phys. **9**, 179 (2013).
[5] Q. P. Unterreithmeier, E. M. Weig, and J. P. Kotthaus, Nature **458**, 1001 (2009).
[6] F. Hocke. *Microwave circuit-electromechanics in a nanomechanical hybrid system*. Ph.D. thesis, Technische Universität München, Walther-Meißner-Institut für Tieftemperaturforschung (2013).
[7] Q. P. Unterreithmeier, S. Manus, and J. P. Kotthaus, Appl. Phys. Lett. **94**, 263104 (2009).
[8] A. H. Nayfeh, and D. T. Mook. *Nonlinear Oscillations* (John Wiley & Sons, New York, 1979).
[9] M. Pernpeintner, T. Faust, F. Hocke, J. P. Kotthaus, E. M. Weig, H. Huebl, and R. Gross, Appl. Phys. Lett. **105**, 123106 (2014).
[10] Q. P. Unterreithmeier, T. Faust, and J. P. Kotthaus, Phys. Rev. Lett. **105**, 027205 (2010).
[11] T. Faust, J. Rieger, M. J. Seitner, J. P. Kotthaus, and E. M. Weig, Phys. Rev. B **89**, 100102 (2014).

Coupling phosphorus donors to a superconducting resonator

C. W. Zollitsch, K. Müller, S. T. B. Goennenwein, R. Gross, H. Huebl [1]
M. S. Brandt [2,3]

In the field of quantum information storage, spin ensembles are promising candidates due to their long electron and nuclear spin coherence times of 0.5 s [1] and 39 min [2], respectively. Their combination with microwave resonators in the strong coupling regime lays the basis of controlled information transfer between subsystems, i.e., quantum state storage [3]. Here, we report on the coupling of a superconducting coplanar microwave resonator made of niobium to an ensemble of phosphorus donors in an isotopically purified ^{28}Si host material. We find that the observed coupling g_{eff} is of the same order as the loss rate of the spin system γ demonstrating the onset of strong coupling. Additionally, the low-temperature electron spin resonance spectroscopy technique established now at WMI is an ideal platform for the investigation of material science physics.

Figure 1(a) shows a color encoded continuous wave transmission spectrum of a superconducting coplanar niobium microwave resonator coupled to an ensemble of phosphorus donors. The experiments are performed at 50 mK and an incident microwave power of 1 fW. We find a high transmission in absence of electron spin resonance. In contrast, at the electron spin resonance fields the microwave absorption is increased appearing as white dips in the field dependent resonator transmission. This allows for a clear identification of the phosphorus donor spin ensemble via their characteristic hyperfine splitting of 4.2 mT. Please note that the spectra show an excellent signal-to-noise ratio demonstrating the high sensitivity of our spectrometer.

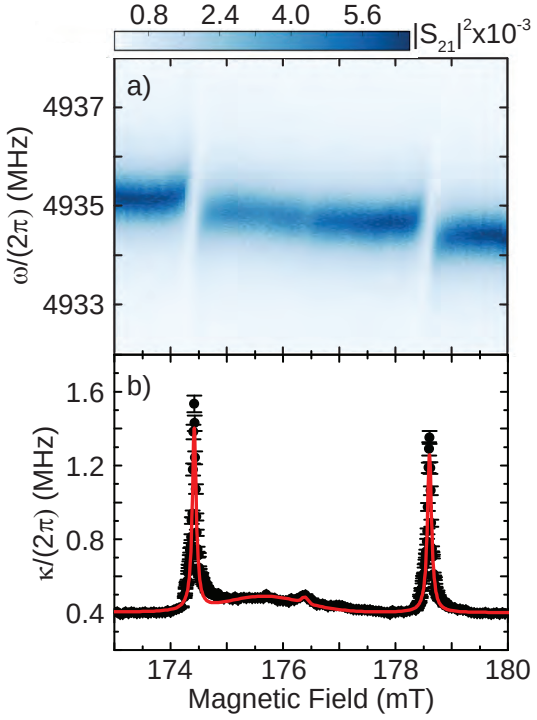

Figure 1: (a) Magnetic field dependent microwave transmission spectroscopy of a superconducting resonator coupled to a phosphorus donor spin ensemble in silicon. The resonance line at 174.4 mT (178.6 mT) correspond to the $m_{\mathrm{I}} = +1/2$ ($m_{\mathrm{I}} = -1/2$) electron spin resonance transition. Panel (b) shows the extracted HWHM κ of the resonator as a function of the magnetic field. The red curve represents a fit to the dispersive model (1).

Next, we analyze the coupled resonator-spin system in terms of the coupling rate g_{eff} and the characteristic loss rates κ and γ of the microwave resonator and the spin system, respectively. To this end, we fit a Lorentzian line to the frequency dependent transmission data and extract the half width at half maximum κ (Fig. 1(b)). Far of spin resonance, the linewidth corresponds to the total loss rate of the microwave resonator κ_0, while under spin resonance conditions the situation is more complicated. In this case, the microwave photons present in the resonator are coupled to the spin system via the coupling rate g_{eff}. Therefore, they have an additional escape channel via the intrinsic spin relaxation mechanisms. Using a dispersive model [4] allows for a quantitative analysis of the contributing escape rates.

[1]The authors acknowledge financial support from the German Research Foundation (DFG) via the project SFB 631 and the German Excellence Initiative via the Nanosystems Initiative Munich (NIM).
[2]Walter Schottky Institut, Technische Universität München
[3]Physik-Department, Technische Universität München

The total escape rate reads as

$$\kappa = \kappa_0 + \frac{g_{\mathrm{eff}}^2 \gamma}{(\omega_{\mathrm{res}} - \omega_{\mathrm{S}})^2 + \gamma^2}, \tag{1}$$

with $\omega_{\mathrm{res}}/2\pi$ and $\omega_{\mathrm{S}}/2\pi$ being the resonance frequency of the microwave resonator and the spin transition, respectively. For the particular spectrum shown in Fig. 1(a), we find $\kappa_0/2\pi =$ 400 kHz and a low (high) field spin resonance $\gamma/2\pi = 1.18$ MHz (1.25 MHz). Additionally, we determine the coupling rate for the low (high) field spin resonance to $g_{\mathrm{eff}}/2\pi = 1.08$ MHz (1.04 MHz).

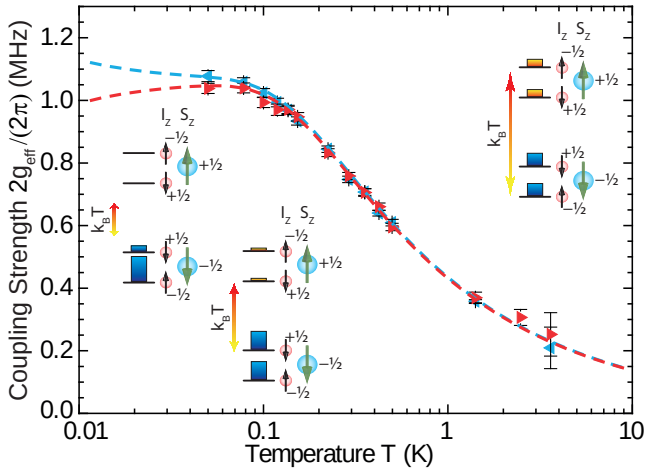

Figure 2: Coupling strength for the low field $m_{\mathrm{I}} = +1/2$ (blue symbols) and high field $m_{\mathrm{I}} = -1/2$ (red symbols) spin resonance lines as a function of temperature. The dashed lines model the coupling rate considering the thermal polarization of the respective transition. The insets sketch the population of the four energy levels of the phosphorus donor spins in three temperature regimes.

We studied the coupling strength as a function of temperature up to 3.5 K (see Fig. 2). For temperatures below 100 mK, the coupling strengths differ for the two phosphorus lines, whereas above 100 mK the coupling strengths coincide and follow the same temperature dependence. We explain this behavior with the thermal spin polarization. The coupling strength is given by $g_{\mathrm{eff}} = g_0\sqrt{NP}$ [5], with g_0 the single photon single spin coupling rate, N the number of spins, and P the thermal polarization of the respective spin resonance line. The latter is derived from the population difference of the particular electron spin resonance transition. We find, that the high (above 100 mK) temperature limit is well covered by a simple spin 1/2 approximation. Additionally, our model confirms that at low temperatures the finite asymmetry of the coupling rates is due to the onset of thermal polarization of the two low lying hyperfine split states.

In summary, we investigated the temperature dependent coupling of a superconducting coplanar microwave resonator to an ensemble of phosphorus donor spins and find excellent agreement between the experimental data and our model based on the thermal polarization of the spin ensemble. The high sensitivity of our electron spin resonance spectroscopy setup makes this technique particularly interesting for material science research.

References

[1] J. T. Muhonen, J. P. Dehollain, A. Laucht, F. E. Hudson, R. Kalra, T. Sekiguchi, K. M. Itoh, D. N. Jamieson, J. C. McCallum, A. S. Dzurak, and A. Morello, Nature Nano. advance online puplication (2014).
[2] K. Saeedi, S. Simmons, J. Z. Salvail, P. Dluhy, H. Riemann, N. V. Abrosimov, P. Becker, H.-J. Pohl, J. J. L. Morton, and M. L. W. Thewalt, Science **342**, 830 (2013).
[3] Y. Kubo, I. Diniz, A. Dewes, V. Jacques, A. Dréau, J.-F. Roch, A. Auffeves, D. Vion, D. Esteve, and P. Bertet, Phys. Rev. A **85**, 012333 (2012).
[4] M. Albert, J. P. Marler, P. F. Herskind, A. Dantan, and M. Drewsen, Phys. Rev. A **85**, 023818 (2012).
[5] K. Sandner, H. Ritsch, R. Amsüss, C. Koller, T. Nöbauer, S. Putz, J. Schmiedmayer, and J. Majer, Phys. Rev. A **85**, 053806 (2012).

Spin Hall magnetoimpedance

J. Lotze, H. Huebl, R. Gross, S. T. B. Goennenwein [1]

The spin Hall effect (SHE) [1] describes the interconversion of charge and spin currents in electrical conductors with finite spin-orbit coupling. Therefore, spin Hall physics is of key importance for a broad variety of spin current-based and spin-caloritronic phenomena, such as the spin Seebeck effect [2], spin pumping [3], and spin Hall magnetoresistance [4–6]. Hereby, it is generally assumed that phenomena related to spin Hall physics are independent of frequency up to tens or hundreds of GHz, since the SHE hinges on spin-orbit coupling. However, an experimental investigation of this conjecture had not been put forward.

In order to critically test the presumed frequency-independence of spin Hall physics in the GHz frequency range, spin Hall magnetoresistance (SMR) experiments as a function of frequency appear particularly attractive. The SMR arises in ferromagnetic insulator/normal metal (FMI/N) bilayers [6]. Because of the SHE, a pure spin current originates from the charge current flowing in the normal metal. Depending on the orientation of the magnetization of the FMI with respect to the spin polarization of the spin current, this spin current either can or cannot propagate across the interface into the insulating ferromagnetic layer. This results in a characteristic dependence of the resistance of the normal metal on the magnetization orientation in the adjacent magnetic insulator, although no electrical current flows through the FMI [4, 5]. Owing to this mechanism, the SMR exhibits a characteristic dependence on the magnetization orientation in the FMI, which is qualitatively different from anisotropic magnetoresistance in bulk polycrystalline FM metals [4, 5]. The SMR furthermore depends quadratically on the spin Hall angle (which parameterizes the SHE-based spin to charge current conversion efficiency), such that it is a very sensitive probe for spin Hall physics.

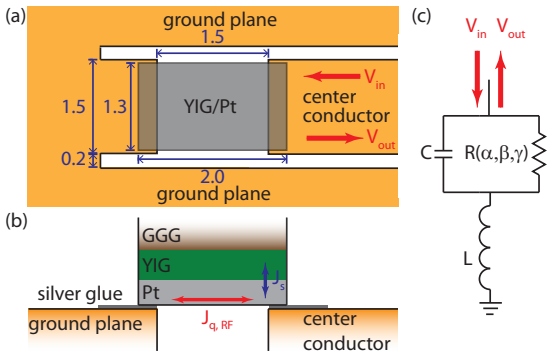

Figure 1: Top view (a) and cross-sectional drawing along the center conductor (b) of a YIG/Pt bilayer bridging a gap in the Cu center conductor of a coplanar waveguide (CPW) structure. The spatial dimensions shown are given in mm. (c) The equivalent electrical circuit model used to describe the YIG/Pt bilayer on the CPW.

To measure the impedance of a YIG(55 nm)/Pt(4 nm) sample grown at WMI up to GHz frequencies, we integrate it into a coplanar waveguide (CPW) structure. The CPW structure was patterned onto a printed circuit board (PCB) as shown in Fig. 1(a,b). The ac current is injected using a surface mount mini-SMP connector at one end of the CPW structure. The CPW is short-circuited at the other end. The center conductor is interrupted by a $1.5 \times 1.5\,\mathrm{mm}^2$ square gap in the PCB. The YIG/Pt bilayer is attached to the CPW structure with the Pt facing down toward the copper of the CPW centerline using silver glue. The YIG/Pt sample thus is bridging this gap, as shown in Fig. 1(a,b). Since the sample integrated into the CPW structure constitutes a load that is not equal to the system impedance $Z_0 = 50\,\Omega$, part of the ac current is reflected at the sample. Measuring this reflection allows us to extract the resistance of the sample. To perform measurements as a function of the magnitude and direction of an external magnetic field, the CPW/sample chip is inserted into a rotatable electromagnet. We mounted the sample chip in three different ways: In the in-plane (ip) configuration, the magnetic field

[1] Financial support by the German Research Foundation via Priority Programme SPP 1538 "Spin Caloric Transport" (Project No. GO 944/4-1) and the Nanosystems Initiative Munich (NIM) is gratefully acknowledged.

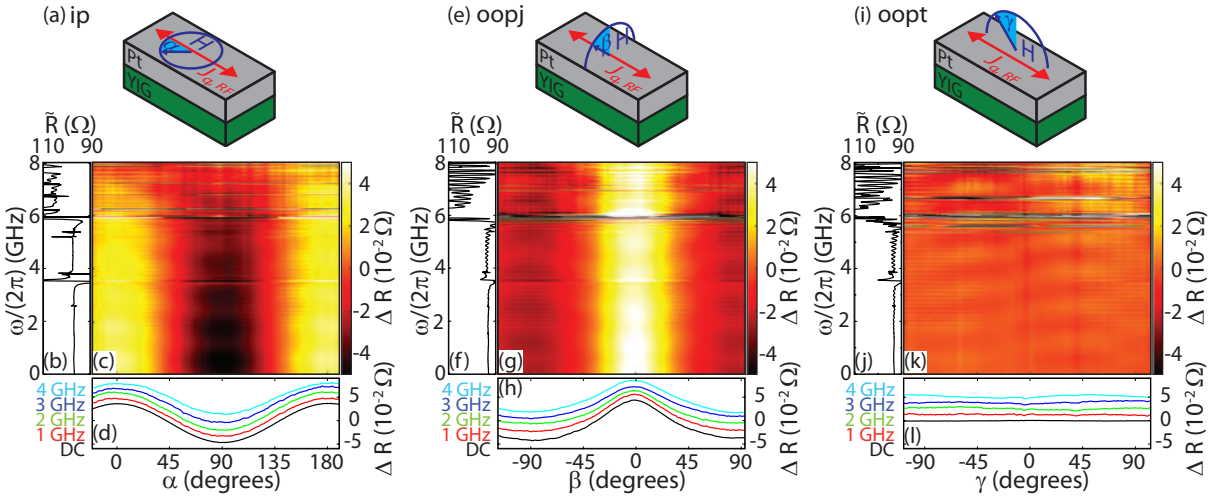

Figure 2: Frequency dependent resistance for the ip, oopj, and oopt rotation planes. Panels (a,e,i) show a sketch of the YIG/Pt bilayer and the external magnetic field relative to the applied bias current direction. Panels (b,f,j) show $\tilde{R}$ according to Eq. (5) for frequencies between dc and 8 GHz for the respective magnetic field rotations. Panels (c,g,k) show the resistance modulation ΔR with respect to ac current frequency and the corresponding magnetic field rotation angles at a constant external magnetic field of $\mu_0|\mathbf{H}| = 0.6$ T. Panels (d,h,l) show ΔR as a function of the respective rotation angles at different, fixed frequencies: dc (black line), 1 GHz (red line), 2 GHz (green line), 3 GHz (blue line), 4 GHz (light blue line). The ΔR curves are offset for clarity.

is always within the plane of the YIG/Pt bilayer. In the oopj configuration the rotation axis of the magnetic field is parallel to the current direction. In the oopt configuration, the rotation axis lies in the film plane, perpendicular to the current direction. The rotation angles α, β, and γ for the ip, oopj, and oopt configurations are defined in Fig. 2(a,e,i), respectively. We investigate the resistance of the sample as a function of magnetization orientation in two ways: We first measure the dc resistance of the sample by driving a dc current over our sample and recording the voltage drop. In a second set of experiments, we measured the complex reflection coefficient S_{11} with a vector network analyzer as a function of frequency $\omega/(2\pi)$ up to 8 GHz. Assuming the electrical circuit model presented in Fig. 1(c) for our sample, we extract the resistance of the sample as a function of frequency and magnetic field orientation from the S_{11} data.

For a (dc) SMR-like behavior, we expect the following dependence of the resistance R on the magnetization orientation [4]:

$$R_{\mathrm{ip}}(\alpha) = R_0 + R_1 \cos^2 \alpha\,, \tag{1}$$

$$R_{\mathrm{oopj}}(\beta) = R_0 + R_1 \cos^2 \beta\,, \text{ and} \tag{2}$$

$$R_{\mathrm{oopt}} = R_0 + R_1\,. \tag{3}$$

The MR ratio

$$\frac{R_1}{R_0} = \frac{2\theta_{\mathrm{SH}}^2 \lambda_{\mathrm{SD}}^2 \rho t^{-1} G_{\mathrm{r}} \tanh^2(\frac{t}{2\lambda_{\mathrm{SD}}})}{1 + 2\lambda_{\mathrm{SD}} \rho G_{\mathrm{r}} \coth(\frac{t}{\lambda_{\mathrm{SD}}})} \tag{4}$$

depends on the spin Hall angle θ_{SH}, the resistivity ρ of the Pt, the spin diffusion length λ_{SD}, the real part of the spin mixing interface conductance G_{r}, [5] and the thickness t of the Pt film. In Fig. 2, we show the ac magnetoresistance obtained from our measurements for the three rotation planes. This figure is organized as follows: there are 4 panels for the three rotation planes, respectively: in (a,e,i) we show a sketch of each measurement geometry for the three rotation planes and define the rotation angle with respect to the external magnetic field. In

(b,f,j) we show the frequency dependent resistance

$$\widetilde{R}(\omega) = \frac{1}{N}\sum_{i=1}^{N} R(\omega, \{\alpha_i, \beta_i, \gamma_i\}) \tag{5}$$

averaged over all N magnetization orientations studied in a given magnetic field rotation plane as a function of ac current frequency. Panels (c,g,k) show the resistance modulation

$$\Delta R(\omega, \{\alpha, \beta, \gamma\}) = R(\omega, \{\alpha, \beta, \gamma\}) - \widetilde{R}(\omega)\,, \tag{6}$$

as a function of both frequency and magnetic field angle in a false color plot, while ΔR traces recorded at selected frequencies are depicted in panels (d,h,l).

We first analyze the change in dc resistance as a function of the magnetization orientation. The black lines in Fig. 2(d,h,l) show the change in resistance $\Delta R(dc)$ for $\mu_0|\mathbf{H}| = 0.6\,\mathrm{T}$ as a function of the angle. The characteristic $\cos^2(\alpha)$-dependence of Eq. (1) is clearly evident in Fig. 2(d) as well as the expected $\cos^2(\beta)$ type modulation of Eq. (2) for the oopj rotation in Fig. 2(h). Last but not least, for a rotation of the magnetic field in the oopt rotation plane the resistance is constant (Fig. 2(l)), as expected from Eq. (3). Thus the observed angular dependence is the one expected from the SMR effect according to Eqs. (1)-(3). The dc resistance $R_0 = 97\,\Omega$ and a resistance modulation amplitude $R_1 = max(\Delta R) - min(\Delta R) = 0.083\,\Omega$ yield a MR ratio of $R_1/R_0 = 8.6 \times 10^{-4}$. Using the parameters $\theta_{\mathrm{SH}} = 0.11$, $\lambda_{\mathrm{SD}} = 1.5\,\mathrm{nm}$, $G_{\mathrm{r}} = 4 \times 10^{14}\,\Omega^{-1}\,\mathrm{m}^2$ [4] and the thickness of the Pt film of $t = 4\,\mathrm{nm}$, one expects a dc SMR magnitude of $R_1/R_0 = 7.7 \times 10^{-4}$ from Eq. (4), in good agreement to the MR ratio measured experimentally.

In summary, we find that the phenomenology of the magnetoresistance observed does not change within experimental accuracy when making the transition from dc to ac bias currents. For the ip rotation (Fig. 2(c)), we find a resistance modulation $\propto \cos^2(\alpha)$, regardless of the ac current frequency up to at least 3 GHz. Similarly, the oopj data (Fig. 2(g)) show a $\cos^2(\beta)$ dependence, while for the oopt orientation (Fig. 2(k)) the resistance is independent of magnetization orientation. In Fig. 2(d,h,l), we compare the change in resistance as a function of the applied magnetic field angle for an applied dc as well as 1, 2, 3, and 4 GHz ac currents. Clearly, the shape of the curves and the amplitude of the modulation is the same, irrespective of frequency. Qualitatively, this modulation even persists at frequencies higher than 3 GHz. Our data therefore provide clear evidence that the phenomenology of the SMR can be described up to frequencies of at least 3 GHz with real, frequency independent values for L, C, R, as well as θ_{SH}, with only R depending on magnetization orientation [7]. The spin Hall physics is therefore frequency-independent up to at least several GHz. From a more applied perspective, our experiments show that the SMR can be used to read out the orientation in a ferromagnetic insulator such as YIG electrically in about 50 ps.

References

[1] J. E. Hirsch, Phys. Rev. Lett. **83**, 1834 (1999).
[2] M. Weiler, M. Althammer, F. D. Czeschka, H. Huebl, M. S. Wagner, M. Opel, I.-M. Imort, G. Reiss, A. Thomas, R. Gross, and S. T. B. Goennenwein, Phys. Rev. Lett. **108**, 106602 (2012).
[3] F. D. Czeschka, L. Dreher, M. S. Brandt, M. Weiler, M. Althammer, I.-M. Imort, G. Reiss, A. Thomas, W. Schoch, W. Limmer, H. Huebl, R. Gross, and S. T. B. Goennenwein, Phys. Rev. Lett. **107**, 046601 (2011).
[4] M. Althammer, S. Meyer, H. Nakayama, M. Schreier, S. Altmannshofer, M. Weiler, H. Huebl, S. Geprägs, M. Opel, R. Gross, D. Meier, C. Klewe, T. Kuschel, J.-M. Schmalhorst, G. Reiss, L. Shen, A. Gupta, Y.-T. Chen, G. E. W. Bauer, E. Saitoh, and S. T. B. Goennenwein, Phys. Rev. B **87**, 224401 (2013).
[5] Y.-T. Chen, S. Takahashi, H. Nakayama, M. Althammer, S. T. B. Goennenwein, E. Saitoh, and G. E. W. Bauer, Phys. Rev. B **87**, 144411 (2013).
[6] H. Nakayama, M. Althammer, Y.-T. Chen, K. Uchida, Y. Kajiwara, D. Kikuchi, T. Ohtani, S. Geprägs, M. Opel, S. Takahashi, R. Gross, G. E. W. Bauer, S. T. B. Goennenwein, and E. Saitoh, Phys. Rev. Lett. **110**, 206601 (2013).
[7] J. Lotze, H. Huebl, R. Gross, and S. T. B. Goennenwein, Phys. Rev. B **90**, 174419 (2014).

Temperature dependence of the spin Seebeck effect in $Gd_3Fe_5O_{12}$/Pt bilayer

S. Geprägs, F. Della Coletta, S. Meyer, A. Kamra, M. Althammer, H. Huebl, R. Gross, S. T. B. Goennenwein [1]
A. Kehlberger, T. Schulz, C. Mix, G. Jakob, M. Kläui [2]

Magnons are the fundamental excitations in a magnetically ordered system. In the presence of a temperature gradient, the magnon population at the hot end of a magnetic material is larger than at the cold end, resulting in an effective magnon flow along the thermal gradient [1]. Since magnons carry spin angular momentum, a thermal gradient thus will drive a pure magnonic spin current in a ferromagnetic insulator, a phenomenon referred to as the spin Seebeck effect (SSE) [1, 2]. Lately, the SSE has attracted much attention, due to open fundamental physics questions regarding its origin on the one hand [3–6], and due to its application potential on the other hand [7]. So far most SSE experiments were performed in yttrium iron garnet/platinum ($Y_3Fe_5O_{12}$, YIG/Pt) hybrids. For YIG it was shown that the two Fe sub-lattices lead to a complex spin wave dispersion relation [8]. Even more complex magnon spectra are expected using $Gd_3Fe_5O_{12}$ (GdIG) where Gd carries an additional magnetic moment, anticipating more complex and rich SSE physics [9].

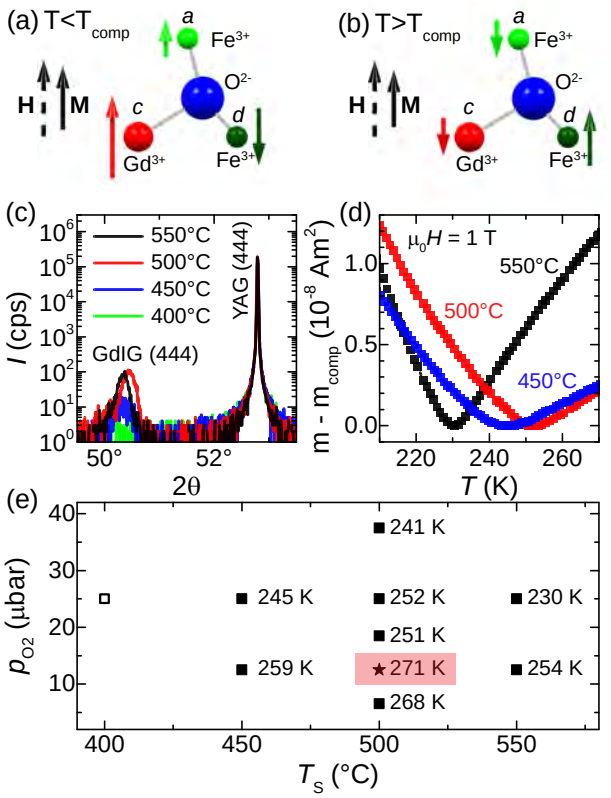

Figure 1: (a),(b) The three different magnetic sub-lattices of GdIG are shown for temperatures below ($T < T_{comp}$) and above ($T > T_{comp}$) the magnetic compensation point. In the presence of a finite magnetic field, the net magnetization **M** points along the external magnetic field **H**. (c) $2\theta - \omega$-scan and (d) normalized temperature-dependent magnetic moment for GdIG thin films fabricated at different substrate temperatures T_S using a constant oxygen pressures p_{O_2} of 25 µbar. (e) p_{O_2}-T_S phase diagram for GdIG thin films. The numbers denote the temperature of the magnetic compensation point T_{comp}.

In order to investigate the longitudinal SSE in GdIG/Pt bilayers, the growth process of single GdIG thin films on (111)-oriented $Y_3Al_5O_{12}$ (YAG) substrates was optimized beforehand. To this end, GdIG thin films were grown by pulsed laser deposition (PLD) from a stoichiometric, polycrystalline target in a pure oxygen atmosphere using a KrF excimer laser with a wavelength of 248 nm and a repetition rate of 10 Hz. First, the substrate temperature T_S during the deposition process was varied between 400 °C and 550 °C, while keeping the oxygen pressure p_{O_2} as well as the laser fluence ρ at the target constant at 25 µbar and 2 Jcm^{-2}, respectively. X-ray diffraction measurements reveal no crystalline growth for substrate temperatures lower

[1]Financial support from the German Research Foundation via SPP 1538 "Spin Caloric Transport", Project No. "GO 944/4-1", and the German Excellence Initiative via the Nanosystems Initiative Munich (NIM) is gratefully acknowledged.
[2]Institute of Physics, University of Mainz, 55099 Mainz, Germany

than 450 °C [cf. Fig. 1(c)]. To investigate the magnetic properties of these thin films SQUID magnetometry measurements were performed. The temperature dependence of the magnetic moment is shown in Fig. 1(d). The magnetization first decreases with decreasing temperature, reaches a minimum, and then increases again.

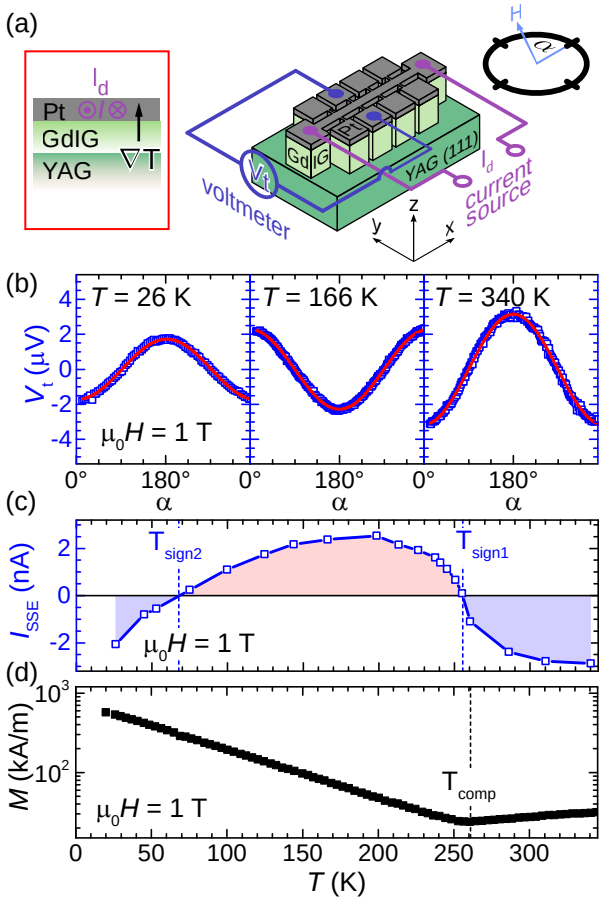

Figure 2: (a) Experimental setup used to measure the longitudinal SSE. (b) Magnetic field orientation dependent transverse voltage V_t recorded for three different temperatures. The red lines represent $\cos(\alpha)$-fits to the data. (c) SSE signal I_{SSE} as a function of temperature obtained from the angle-dependent measurements taking the temperature dependent Pt resistance R(T) into account. Two sign changes are visible at $T_{sign1} \approx 256\,K$ and $T_{sign2} \approx 68\,K$. (d) Temperature-dependent magnetization of the GdIG/Pt bilayer used for the SSE experiments.

As sketched in Figs. 1(a) and (b), GdIG is a ferrimagnet with three magnetic sub-lattices composed of tetrahedrally coordinated Fe^{3+} ions (*d* sites), octahedrally coordinated Fe^{3+} ions (*a* sites), and dodecahedrally coordinated Gd^{3+} ions (*c* sites). The two Fe sub-lattices are strongly antiferromagnetically coupled resulting in a small net Fe moment and a Néel temperature of about $T_N = 550\,K$, while the Gd moments are more weakly exchange coupled to the Fe *a* sub-lattices. As a consequence the Gd magnetization is strongly temperature dependent. At high temperatures, the *d* site Fe ions dominate the net magnetization of GdIG. As the temperature is reduced, the magnetization of the Gd sub-lattice strongly increases, and together with the Fe magnetization at the *a* site eventually overwhelms the Fe magnetization at the *d* site. At the so-called magnetic compensation temperature, the magnetization of the *a* site of Fe and the *c* site of Gd is equal in magnitude but antiparallel to the magnetization of the *d* site of Fe, such that the remanent magnetization of GdIG becomes zero. Since our magnetometry experiments were performed in a finite external magnetic field of magnitude 1 T, the net GdIG magnetization does not vanish, but rather goes through a minimum at T_{comp}.

As obvious from Fig. 1(d), the temperature of the magnetic compensation T_{comp} in GdIG strongly depends on the substrate temperature during the deposition process. The highest T_{comp} was obtained for GdIG thin films grown at 500 °C. The growth process was further optimized varying the oxygen pressure p_{O_2}, the laser fluence ρ at the target, and the laser repetition rate f [cf. Fig. 1(e)]. Best structural and magnetic properties of GdIG thin films were obtained by using $T_s = 500\,°C$, $p_{O_2} = 12.5\,\mu bar$, $\rho = 2\,Jcm^{-2}$, and $f = 10\,Hz$. Using these growth parameters, GdIG/Pt bilayers were fabricated by covering the GdIG thin films *in-situ*, without breaking the vacuum, with 4 nm of Pt deposited via electron beam evaporation.

The longitudinal SSE was recorded as a function of temperature, using a current heating method [10]. To this end, the GdIG/Pt bilayer is micropatterned into a Hall bar structure using optical lithography and Argon ion beam milling [cf. Fig. 2(a)]. The sample is then in-

serted into a 3D vector magnet cryostat. We generate the temperature gradient across the GdIG/Pt interface required for SSE experiments by sourcing a large current $I_d = 6\,\mathrm{mA}$ along the Pt microstructure, and exploit the temperature-dependent resistance of the Pt for on-chip thermometry. The transverse voltage V_t is recorded as a function of the in-plane external magnetic field direction α using a fixed magnetic field magnitude of 1 T. As an example the angle-resolved V_t signal measured at three different temperatures (26 K, 166 K, and 340 K) is shown in Fig. 2(b). As a function of the in-plane external magnetic field direction α, the voltage signal V_t shows a $\cos(\alpha)$-dependence, which is characteristic for the SSE [cf. red lines in Fig. 2(b)]. Interestingly, there are two sign changes. At $T = 340\,\mathrm{K}$ the SSE voltage V_t at $\alpha = 0°$ is negative, while it is positive for $T = 166\,\mathrm{K}$, and negative again for $T = 26\,\mathrm{K}$. In order to characterize the temperature-dependent evolution of the SSE signal in more detail, the SSE amplitude is calculated from $I_{SSE} = V_{SSE}(T)/R(T)$ with $V_{SSE} = \frac{1}{2}\left[V_t(+I_d) + V_t(-I_d)\right]$ taking the temperature dependence of the Pt resistance $R(T)$ into account. The SSE signal first is negative at high temperatures, then becomes positive in a temperature interval $68\,\mathrm{K} \lesssim T \lesssim 256\,\mathrm{K}$, and is negative again for $T \lesssim 68\,\mathrm{K}$. The first sign change at 256 K can be correlated to the magnetic compensation temperature T_{comp} [cf. Fig. 2(c)]. At this temperature, the sub-lattice magnetization orientations reverses, which causes a reversal of the spin current polarization. The second sign change at 68 K is caused by a competition between a soft-mode magnon composed of Gd spins and a gapped-mode magnon mainly composed of Fe spins taking different interface (*s-d* or *s-f*) exchange couplings into account. However, the physical origin of the second sign change is still under investigation [9].

In summary, we have experimentally investigated the temperature dependence of the longitudinal SSE effect in GdIG/Pt bilayers. Two consecutive sign changes of the SSE signal were found with decreasing temperature. The first sign change occurs around the magnetic compensation point T_{comp} of GdIG indicating the dominant role of the Fe sub-lattices in this temperature range. The second, more gradual sign change, of the SSE signal at around $T_{sign2} \approx 68\,\mathrm{K}$ is caused by competing magnons composed of Gd or Fe spins, respectively. Our results thus show that magnons from different magnetic sub-lattices can quantitatively alter the SSE and that the thermal spin currents do not simply replicate the total magnetization.

References

[1] K. Uchida, J. Xiao, H. Adachi, J. Ohe, S. Takahashi, J. Ieda, T. Ota, Y. Kajiwara, H. Umezawa, H. Kawai, G. E. W. Bauer, S. Maekawa, and E. Saitoh, Nature Mater. **9**, 894 (2010).

[2] G. E. W. Bauer, E. Saitoh, and B. J. van Wees, Nature Mater. **11**, 391 (2012).

[3] K. Uchida, T. Nonaka, T. Ota, and E. Saitoh, Appl. Phys. Lett. **97**, 172505 (2010).

[4] M. Schreier, A. Kamra, M. Weiler, J. Xiao, G. E. W. Bauer, R. Gross, and S. T. B. Goennenwein, Phys. Rev. B **88**, 094410 (2013).

[5] N. Roschewsky, M. Schreier, A. Kamra, F. Schade, K. Ganzhorn, S. Meyer, H. Huebl, S. Geprägs, R. Gross, and S. T. B. Goennenwein, Appl. Phys. Lett. **104**, 202410 (2014).

[6] K. Ganzhorn. *Experimental Study of Spin Currents in Compensated Rare Earth Garnets*. Master's thesis, Technische Universität München (2014).

[7] A. Kirihara, K. Uchida, Y. Kajiwara, M. Ishida, Y. Nakamura, T. Manako, E. Saitoh, and S. Yorozu, Nature Mater. **11**, 686 (2012).

[8] V. Cherepanov, I. Kolokolov, and V. L'vov, Phys. Rep. **229**, 81 (1993).

[9] S. Geprägs, A. Kehlberger, T. Schulz, C. Mix, F. Della Coletta, S. Meyer, A. Kamra, M. Althammer, G. Jakob, H. Huebl, R. Gross, S. T. B. Goennenwein, and M. Kläui. Origin of the spin Seebeck effect probed by temperature dependent measurements in $Gd_3Fe_5O_{12}$. arXiv:1405.4971 (2014).

[10] M. Schreier, N. Roschewsky, E. Dobler, S. Meyer, H. Huebl, R. Gross, and S. T. B. Goennenwein, Appl. Phys. Lett. **103**, 242404 (2013).

Time resolved spin Seebeck effect experiments

N. Roschewsky, M. Schreier, A. Kamra, F. Schade, K. Ganzhorn, S. Meyer, H. Huebl, S. Geprägs, R. Gross, S. T. B. Goennenwein [1]

The possibility to drive pure spin angular momentum currents across ferromagnet/metal interfaces by means of thermal gradients is referred to as "spin Seebeck effect" in the literature [1]. While such experiments are nowadays widely established, the microscopic mechanisms behind the thermal spin current generation are still controversially discussed [2–6]. Until today, the majority of the spin Seebeck experiments is performed using static (DC) or low-frequency thermal gradients to drive the spin angular momentum current [7–9]. In contrast, time-resolved measurements could provide important information on the nonequilibrium situation present in such experiments and allow us to identify the time constants relevant for the spin Seebeck effect. More specifically, a number of theoretical models [5, 6] assume that the magnon-phonon thermalization time is equal to the relaxation time of the uniform magnetization precession mode $\tau_{\mathrm{mp}}^{k=0}$. If this assumption is valid, one would expect a frequency dependent roll-off of the dynamical spin Seebeck effect response when the thermal gradient driving the effect is modulated at frequencies larger than $(\tau_{\mathrm{mp}}^{k=0})^{-1}$.

At WMI we have performed transient thermopower (time-resolved spin Seebeck effect) measurements in YIG/Pt thin film bilayers in the so-called longitudinal spin Seebeck configuration [8]. In our experiments we use an intensity modulated, focused laser beam to generate a temperature gradient perpendicular to the YIG/Pt bilayer (Fig. 1) [7]. The focused laser beam mainly excites the electron system of the metal, which thermalizes with the phonon and magnon systems by electron-phonon and phonon-magnon interaction. A steady state situation is reached after a time $t \approx \tau^*$, representing the slowest time constant in the system. In our measurements, we use a square waveform modulation of the laser intensity at frequency f_{mod}, resulting in a periodic heating at this frequency. Then, via the spin Seebeck effect, the sample acts as a voltage source with a periodic output signal of amplitude $V_{0,\mathrm{SSE}}$. Our time resolved spin Seebeck measurements are performed with an effective bandwidth of 50 MHz of the detection electronics, but are ultimately limited to a bandwidth of typically less than 30 MHz by the characteristic RC-type low-pass behavior of the samples. The latter suppressed the detected $V_{0,\mathrm{SSE}}$ above a characteristic frequency which is not related to spin Seebeck physics. In our experiments, we measured the spin Seebeck voltage as a function of the laser modulation frequency for three different samples YIG(a)/Pt(b), with the numbers a and b in parentheses indicating the individual layer thicknesses in nanometers.

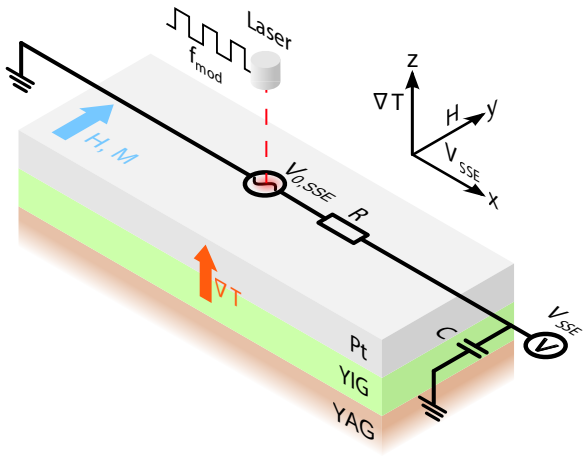

Figure 1: An intensity modulated red laser generates a temperature gradient ∇T along the YIG/Pt surface normal. The ensuing spin current across the YIG/Pt interface is converted into a charge current by the inverse spin Hall effect. For open circuit conditions a voltage drop along the Pt layer is measured. The voltage detection is ultimately limited by the low-pass behavior of the sample and the measurement electronics, which are sketched as an equivalent circuit diagram.

[1] Financial support from the German Research Foundation via SPP 1538 "Spin Caloric Transport", Project No. GO 944/4-1 is gratefully acknowledged

As shown by Fig. 2, the YIG(48)/Pt(4.9) sample ($R = 876\,\Omega$) has the lowest 3 dB cutoff frequency $f_c \simeq 1.57$ MHz, while the YIG(61)/Pt(19.5) sample ($R = 309\,\Omega$) exhibits a slightly larger one (3.08 MHz). The third sample [YIG(55)/Pt(16.8)] was designed to exhibit a small resistance ($R = 47\,\Omega$) which results in a 3 dB cutoff frequency of about 37 MHz. The solid lines in Fig. 2 are the fitted first-order low-pass decays of the individual samples. From these fits we can extract the common shunt capacitance $C = 125(39)$ pF of our measurement setup. Clearly, we observe no significant deviation of the spin Seebeck voltage from the expected first-order low-pass behavior up to a modulation frequency as high as 30 MHz. As any additional intrinsic time constant (e.g. by a long phonon-magnon interaction time) would lead to a steeper drop in the measured voltage, we conclude that the relevant intrinsic time constants τ^* for the spin Seebeck effect must be shorter than about $\tau = (2\pi f)^{-1} \approx 5$ ns. Assuming that the phonon-magnon interaction time in our YIG thin films is comparable to the bulk value, our experimental findings rule out small wavenumber magnons and the uniform precession mode ($k = 0$) as the dominant source of the spin Seebeck effect spin current, since their interaction times with phonons are of the order of several hundred nanoseconds ($\tau_{mp}^{k\approx 0} \approx 300$ ns) [10]. Indeed, recent theoretical considerations [6, 11] suggest that thermal (large k) and not the $k = 0$ magnons are responsible for the spin Seebeck effect. This suggestion is in agreement with our experiments since these magnons are predicted [6, 11] to thermalize with phonons much faster than their $k = 0$ counterparts.

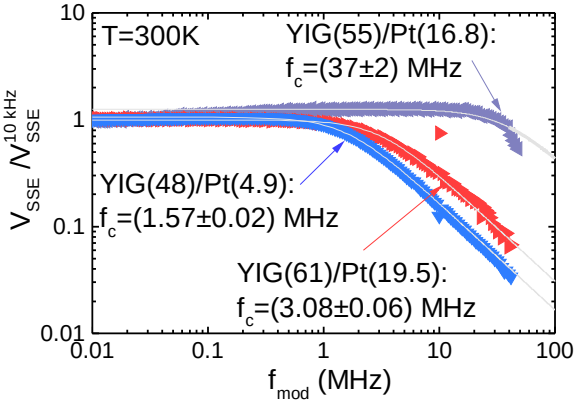

Figure 2: Normalized spin Seebeck voltage as a function of the laser modulation frequency f_{mod} for three different samples. In all samples V_{SSE} is essentially frequency independent up to about 1 MHz. The roll-off in V_{SSE} observed for $f_{mod} \gtrsim 1$ MHz is quantitatively described by a low-pass transfer function, using a shunt capacitance of $C = 125(39)$ pF and the resistance R of the respective samples. The corresponding 3 dB low-pass cutoff frequency f_c is quoted for each sample.

The upper bound of the phono-magnon interaction time derived from our experiments [12] is of key relevance for future theoretical studies and experiments as well as potential applications of the spin Seebeck effect. Nevertheless, further experiments with improved time resolution are necessary to substantiate the role of thermal magnons for the spin Seebeck effect.

References

[1] G. E. W. Bauer, E. Saitoh, and B. J. van Wees, Nature Mater. **11**, 391–399 (2012).
[2] H. Adachi, J.-i. Ohe, S. Takahashi, and S. Maekawa, Phys. Rev. B **83**, 094410 (2011).
[3] H. Adachi, K. Uchida, E. Saitoh, and S. Maekawa, Rep. Prog. Phys. **76**, 036501 (2013).
[4] K. S. Tikhonov, J. Sinova, and A. M. Finkel'stein, Nat Commun **4** (2013).
[5] J. Xiao, G. E. W. Bauer, K. Uchida, E. Saitoh, and S. Maekawa, Phys. Rev. B **81**, 214418 (2010).
[6] S. Hoffman, K. Sato, and Y. Tserkovnyak, Phys. Rev. B **88**, 64408 (2013).
[7] M. Weiler, M. Althammer, F. D. Czeschka, H. Huebl, M. S. Wagner, M. Opel, I.-M. Imort, G. Reiss, A. Thomas, R. Gross, and S. T. B. Goennenwein, Phys. Rev. Lett. **108**, 106602 (2012).
[8] K. Uchida, H. Adachi, T. Ota, H. Nakayama, S. Maekawa, and E. Saitoh, Appl. Phys. Lett. **97**, 172505 (2010).
[9] D. Qu, S. Y. Huang, J. Hu, R. Wu, and C. L. Chien, Phys. Rev. Lett. **110**, 067206 (2013).
[10] E. Spencer, and R. C. LeCraw, IEE Proc-B **109**, 66–70 (1962).
[11] M. Schreier, A. Kamra, M. Weiler, J. Xiao, G. E. W. Bauer, R. Gross, and S. T. B. Goennenwein, Phys. Rev. B **88**, 094410 (2013).
[12] N. Roschewsky, M. Schreier, A. Kamra, F. Schade, K. Ganzhorn, S. Meyer, H. Huebl, S. Geprägs, R. Gross, and S. T. B. Goennenwein, Appl. Phys. Lett. **104**, 202410 (2014).

Comparative study of X-ray magnetic circular dichroism and X-ray resonant magnetic reflectivity in Pt on ferrimagnetic insulators

F. Della Coletta, M. Opel, S. Geprägs, S. T. B. Goennenwein, R. Gross [1]
C. Klewe, T. Kuschel [2]
K. Ollefs, F. Wilhelm, A. Rogalev [3]

The interplay between charge and spin currents in paramagnetic metals or at interfaces to ferromagnetic insulators results in novel spintronic effects, such as the spin Hall effect (SHE) [1] or the recently discovered spin Hall magnetoresistance (SMR) effect [2]. The latter manifests itself in an unexpected dependence of the resistivity of Pt (representing the most widely used spin Hall material) on the magnetization of an adjacent ferrimagnetic insulating $Y_3Fe_5O_{12}$ (YIG) layer. While different groups agree in reporting such an unexpected magnetoresistance in YIG/Pt hybrids [2–4], its interpretation is still a matter of controversy. Two conflictive models are discussed. One relies on the aforementioned SHE in Pt, accompanied by the reflection or absorption of spin currents at the interface [2, 3]. The second proposes a *conventional* anisotropic magnetoresistance (AMR) of Pt in proximity to a ferromagnet [4], well known for all-metallic Fe/Pt or Ni/Pt [5]. The fundamental difference between both models is either the presence of the SHE or the presumption of a static interface proximity spin polarization, both in Pt. In a previous element-selective investigation of YIG/Pt, we found no evidence for such a magnetic proximity effect in Pt for thicknesses of the Pt layer down to 3 nm [6]. To further clarify this issue, we here experimentally compare the X-ray magnetic circular dichroism (XMCD) and the X-ray resonant magnetic reflectivity (XRMR) [7] at the Pt L_3 absorption edge in a comprehensive set of samples: YIG/Pt(3.2 nm), NFO($NiFe_2O_4$)/Pt(3 nm), Fe/Pt(3.2 nm).[4] Both methods provide element-selective information on the magnetic properties of Pt alone, in which the XRMR signal is independent of the thickness of the Pt layer [7]. To detect a static proximity spin polarization in Pt, we switch the magnetic field between ± 0.4 T. To be sensitive to a *dynamic* SHE-induced spin polarization, we also reversed the electrical current applied to Pt between ± 0.1 mA at zero field. All XMCD/XRMR measurements were performed in the newly developed reflectometer at the beamline ID12 of the European Synchrotron Radiation Facility.

To check our methods and experimental setup, we first investigate an all-metallic Fe/Pt reference sample. In the X-ray absorption spectrum (XAS), it displays a normalized whiteline intensity of 1.30 at the Pt L_3 edge (Fig. 1a), consistent with non-oxidized, metallic Pt [9]. The normalized XMCD measured at a switching magnetic field of ± 0.4 T reaches 4%, providing evidence for a magnetic proximity effect in Fe/Pt in agreement with earlier reports [5, 6]. In XRMR, we observe an asymmetry of the data for ± 0.4 T (Fig. 1b) that fits well to a spin polarized layer in Pt close to the interface to Fe [7]. In proximity to the ferrimagnetic insulators YIG and NFO, however, we do not detect any XRMR asymmetry in YIG/Pt or NFO/Pt within the resolution of the experiment (Fig. 1c). We do not observe any significant deviation from zero up to a scattering vector of 0.4 $Å^{-1}$, neither when applying a switching magnetic field of ± 0.4 T to probe a static spin polarization in Pt (red and blue) nor when reversing the electrical current between ± 0.1 mA to probe a dynamic spin polarization in Pt as a result of the SHE (orange). The observation comes along with a zero XMCD signal for all samples, although

[1] This work was supported by the European Synchrotron Radiation Facility (ESRF) via HC-1500 and the German Research Foundation (DFG) via SPP 1538 "Spin Caloric Transport" (projects GO 944/4 and RE 1052/24).

[2] Center for Spinelectronic Materials and Devices, Bielefeld University, 33501 Bielefeld, Germany
[3] European Synchrotron Radiation Facility (ESRF), 38043 Grenoble Cedex 9, France

[4] YIG/Pt was fabricated by pulsed laser deposition (YIG) with *in-situ* electron-beam evaporation (Pt) at WMI [2], NFO/Pt by reactive dc magnetron sputtering at Bielefeld University [8], and Fe/Pt by electron-beam evaporation at WMI [6]. YIG and NFO are ferrimagnetic insulators.

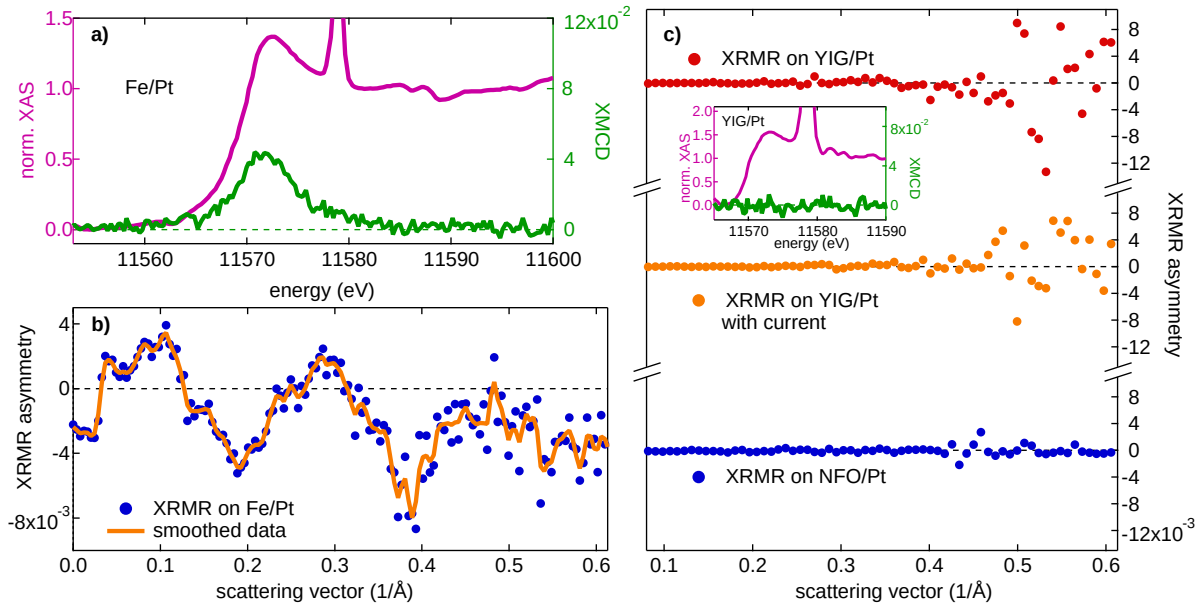

Figure 1: (a) Normalized X-ray absorption spectrum (XAS, purple, left axis) and X-ray magnetic circular dichroism (XMCD, green, right axis), measured with alternating magnetic field, from the Fe/Pt reference sample as a function of the incoming photon energy. (b) X-ray resonant magnetic reflectivity (XRMR) asymmetry spectrum (blue circles), measured with alternating magnetic field at the maximum of the XMCD (11572 eV), from Fe/Pt as a function of the scattering vector. The orange line represents smoothed data. (c) XRMR asymmetry from NFO/Pt (blue) and YIG/Pt (red), measured with alternating magnetic field. XRMR asymmetry from YIG/Pt (orange), measured with alternating electric current. The inset shows the XAS (purple) and the XMCD (green) from YIG/Pt.

they show an XAS whiteline intensity close to metallic Pt, as exemplarily displayed for YIG/Pt in the inset of Fig. 1c. For scattering vectors larger than 0.5 $Å^{-1}$, the low photon intensity leads to an increased relative noise level that prevents an unambiguous analysis of the XRMR data.

In conclusion, we find no indication for an induced magnetic moment in Pt on YIG or Pt on NFO, in contrast to Pt on Fe. At the Pt L_3 edge, both the XMCD (sensitive to the complete Pt layer thickness) and the XRMR (sensitive only to the interface) are zero within experimental error. We cannot confirm a magnetic proximity effect [4] in paramagnetic Pt on ferrimagnetic insulators. The unexpectedly observed magnetoresistance effect in YIG/Pt and NFO/Pt should therefore be interpreted in the framework of the SMR model [2, 3].

References

[1] J. E. Hirsch, Phys. Rev. Lett. **83**, 1834–1837 (1999).
[2] H. Nakayama, M. Althammer, Y.-T. Chen, K. Uchida, Y. Kajiwara, D. Kikuchi, T. Ohtani, S. Geprägs, M. Opel, S. Takahashi, R. Gross, G. E. W. Bauer, S. T. B. Goennenwein, and E. Saitoh, Phys. Rev. Lett. **110**, 206601 (2013).
[3] S. Meyer, M. Althammer, M. Schreier, S. Geprägs, M. Opel, R. Gross, S. Goennenwein, H. Nakayama, E. Saitoh, Y.-T. Chen, and G. Bauer, WMI Ann. Rep. **2013**, 57–59 (2013).
[4] Y. M. Lu, Y. Choi, C. M. Ortega, X. M. Cheng, J. W. Cai, S. Y. Huang, L. Sun, and C. L. Chien, Phys. Rev. Lett. **110**, 147207 (2013).
[5] F. Wilhelm, P. Poulopoulos, G. Ceballos, H. Wende, K. Baberschke, P. Srivastava, D. Benea, H. Ebert, M. Angelakeris, N. K. Flevaris, D. Niarchos, A. Rogalev, and N. B. Brookes, Phys. Rev. Lett. **85**, 413–416 (2000).
[6] S. Geprägs, S. Meyer, S. Altmannshofer, M. Opel, F. Wilhelm, A. Rogalev, R. Gross, and S. T. B. Goennenwein, Appl. Phys. Lett. **101**, 262407 (2012).
[7] T. Kuschel, C. Klewe, J.-M. Schmalhorst, F. Bertram, O. Schuckmann, T. Schemme, J. Wollschläger, S. Francoual, J. Strempfer, A. Gupta, M. Meinert, G. Götz, D. Meier, and G. Reiss. arXiv:1411.0113 (2014).
[8] C. Klewe, M. Meinert, A. Boehnke, K. Kuepper, E. Arenholz, A. Gupta, J.-M. Schmalhorst, T. Kuschel, and G. Reiss, J. Appl. Phys. **115**, 123903 (2014).
[9] A. V. Kolobov, F. Wilhelm, A. Rogalev, T. Shima, and J. Tominaga, Appl. Phys. Lett. **86**, 121909 (2005).

Analytic BCS description of unconventional superconductivity

D. Einzel

Introduction

In a series of papers [1–4] the author has investigated analytic approaches to the description of the temperature dependence of thermostatic (entropy, specific heat capacity) and local response functions (spin susceptibility, normal fluid and superfluid density tensor, magnetic penetration depth) in unconventional superconductors. These papers were restricted to analytic results either in the Ginzburg–Landau (GL) and low temperature regime [1], respectively, or an approximate interpolative treatment for intermediate temperatures [2, 3]. A new method for solving the gap equation in closed form was presented in ref. [4], where in particular the role of the quasiparticle Yosida function $y_{\hat{\mathbf{p}}}$ for an analytic two–fluid description of unconventional superconductivity was studied. It is the purpose of this contribution to simplify the treatment provided in ref. [4] by introducing an analytic form for a temperature–dependent Yosida function $y_{\hat{\mathbf{p}}}$, from which all thermostatic and local response functions can be derived by a simple Fermi surface integration. The results should be particularly convenient for the needs of experimental physicists.

Superconductors in global and local equilibrium

The equilibrium state of an unconventional superconductor can be specified by the Bogoliubov–Valatin quasiparticle (BVQP) energy [5–8]

$$E_{\mathbf{p}} = \sqrt{\xi_{\mathbf{p}}^2 + \Delta_{\hat{\mathbf{p}}}^2} \tag{1}$$

The structure of the energy gap is [1, 3] ($f_{\hat{\mathbf{p}}}$ describes the possible orbital anisotropy):

$$\Delta_{\hat{\mathbf{p}}} = \Delta_0(T)\alpha_f f_{\hat{\mathbf{p}}} \;\; ; \;\; \alpha_f = 1/\langle f_{\hat{\mathbf{p}}}^2 \rangle_{\rm FS}^{\frac{1}{2}} \tag{2}$$

For conventional superconductors $f_{\hat{\mathbf{p}}} = 1$ whereas for unconventional superconductors one has a vanishing Fermi surface average $\langle f_{\hat{\mathbf{p}}} \rangle_{\rm FS} = 0$. Below, we list a few examples for the orbital anisotropy function $f_{\hat{\mathbf{p}}}$:

$$f_{\mathbf{p}} = \alpha_f \begin{cases} 1 & ; \;\; \alpha_f = 1 & ; \;\; \text{3d (pseudo-)isotropic, BCS [5], BW [9]} \\ \cos\theta = x & ; \;\; \alpha_f = \sqrt{3} & ; \;\; \text{3d polar [10]} \\ \sin\theta = \sqrt{1-x^2} & ; \;\; \alpha_f = \sqrt{3/2} & ; \;\; \text{3d axial, ABM [11–14]} \\ \cos\theta\sin\theta = x\sqrt{1-x^2} & ; \;\; \alpha_f = \sqrt{15/2} & ; \;\; \text{3d } d\text{–wave hybrid, E}_{1g} \text{ [15, 16]} \\ \cos\theta\sin^2\theta = x(1-x^2) & ; \;\; \alpha_f = \sqrt{105/8} & ; \;\; \text{3d } f\text{–wave hybrid, E}_{2u} \text{ [17]} \\ \cos 2\phi & ; \;\; \alpha_f = \sqrt{2} & ; \;\; \text{2d } d\text{–wave, } d_{x^2-y^2} \text{ [18]} \end{cases} \tag{3}$$

Let us introduce the dimensionless order parameter $z = \Delta_0(T)/k_{\rm B}T$ and the Yosida functions

$$\begin{aligned} y_{\hat{\mathbf{p}}}(z) &= \int_0^\infty \frac{dt}{\cosh^2\sqrt{t^2 + \frac{z^2}{4}f_{\hat{\mathbf{p}}^2}}} \\ y_{\hat{\mathbf{p}}}^\sigma(z) &= \frac{12}{\pi^2}\int_0^\infty \frac{dt t^2}{\cosh^2\sqrt{t^2 + \frac{z^2}{4}f_{\hat{\mathbf{p}}}^2}} \equiv 1 - \frac{3f_{\hat{\mathbf{p}}}^2}{\pi^2}\int_0^z dz' z' y_{\hat{\mathbf{p}}}(z') \end{aligned} \tag{4}$$

with the aid of which the relevant macroscopic observables can be expressed as Fermi surface averages in the following way:

- BVQP entropy density σ

$$\frac{\sigma(z)}{\sigma_{\mathrm{N}}} = \left\langle y^{\sigma}_{\hat{\mathbf{p}}}(z) \right\rangle_{\mathrm{FS}} \tag{5}$$

- BVQP specific heat capacity c_V

$$\frac{c_V(z)}{c_{\mathrm{N}}} = \left\langle y^{\sigma}_{\hat{\mathbf{p}}}(z) \right\rangle_{\mathrm{FS}} + \frac{3z^2}{\pi^2} \frac{\left\langle f^2_{\hat{\mathbf{p}}} y_{\hat{\mathbf{p}}}(z) \right\rangle_{\mathrm{FS}}}{\left\langle f^2_{\hat{\mathbf{p}}} \left[1 - y_{\hat{\mathbf{p}}}(z)\right] \right\rangle_{\mathrm{FS}}} \tag{6}$$

- BVQP spin susceptibility χ_s

$$\frac{\chi_s(z)}{\chi_{\mathrm{N}}} = \left\langle y_{\hat{\mathbf{p}}}(z) \right\rangle_{\mathrm{FS}} \tag{7}$$

- Magnetic penetration depth (London, BCS) λ_{L}

$$\begin{aligned} \lambda^2_{\mathrm{L}\parallel,\perp}(z) &= \frac{mc^2}{4\pi n e^2 \left[1 - y_{\parallel,\perp}(z)\right]} \\ y_{\parallel,\perp}(z) &= 3 \left\langle \left\{ x^2, \frac{1-x^2}{2} \right\} y_{\hat{\mathbf{p}}}(z) \right\rangle_{\mathrm{FS}} \equiv \frac{n^n_{\parallel,\perp}(z)}{n} \end{aligned} \tag{8}$$

The Fermi surface averages are performed according to

$$\langle \ldots \rangle_{\mathrm{FS}} = \frac{1}{2} \int_0^{\pi} d\theta \sin\theta \int_0^{2\pi} \frac{d\phi}{2\pi} \ldots \stackrel{x=\cos\theta}{=} \int_0^1 dx \int_0^{2\pi} \frac{d\phi}{2\pi} \ldots \tag{9}$$

The gap function $\Delta_0(z)$ of unconventional superconductors can be expressed in closed form as follows [4]:

$$\frac{\Delta_0(z)}{k_{\mathrm{B}} T_{\mathrm{c}}} = z \mathrm{e}^{-\left\langle f^2_{\hat{\mathbf{p}}} b_{\hat{\mathbf{p}}}(z) \right\rangle_{\mathrm{FS}}} \tag{10}$$

Here the generating function $b_{\hat{\mathbf{p}}}(z)$ is related to the quasiparticle Yosida function through [4]:

$$y_{\hat{\mathbf{p}}}(z) = 1 - z \frac{d b_{\hat{\mathbf{p}}(z)}}{dz} \tag{11}$$

The conversion from the z– to the T/T_{c}–scale is possible via the identity [4]:

$$\frac{T}{T_{\mathrm{c}}} = \mathrm{e}^{-\left\langle f^2_{\hat{\mathbf{p}}} b_{\hat{\mathbf{p}}}(z) \right\rangle_{\mathrm{FS}}} \tag{12}$$

The functions $b_{\hat{\mathbf{p}}}(z)$, $y_{\hat{\mathbf{p}}}(z)$ and $y^{\sigma}_{\hat{\mathbf{p}}}(z)$ are therefore seen to exclusively describe the thermostatics and the local response of unconventional superconductors. They read in the GL regime ($\zeta_{\hat{\mathbf{p}}} = z^2 f^2_{\hat{\mathbf{p}}} / \pi^2$):

$$\lim_{z\to 0} b_{\hat{\mathbf{p}}}(z) = \frac{7\zeta(3)}{8} \zeta_{\hat{\mathbf{p}}} \;\; ; \;\; \lim_{z\to 0} y_{\hat{\mathbf{p}}}(z) = 1 - \frac{7\zeta(3)}{4} \zeta_{\hat{\mathbf{p}}} \;\; ; \;\; \lim_{z\to 0} y^{\sigma}_{\hat{\mathbf{p}}}(z) = 1 - \frac{3}{2}\zeta_{\hat{\mathbf{p}}} + \frac{21\zeta(3)}{16} \zeta^2_{\hat{\mathbf{p}}} \tag{13}$$

In the opposite low temperature limit $T \to 0$ one finds [1]:

$$\delta_{\mathrm{sc}} = \frac{\Delta_0(0)}{k_{\mathrm{B}} T_{\mathrm{c}}} = \frac{\pi}{\mathrm{e}^{\gamma}} \mathrm{e}^{-\left\langle f^2_{\hat{\mathbf{p}}} \ln f_{\hat{\mathbf{p}}} \right\rangle_{\mathrm{FS}}} \tag{14}$$

Approximate forms of the functions $b_{\hat{\mathbf{p}}}(z)$ and $y_{\hat{\mathbf{p}}}(z)$

We start with an approximation for the generating function $b_{\hat{\mathbf{p}}}(z)$:

$$b^{\mathrm{E}}_{\hat{\mathbf{p}}}(z) \;=\; -\ln\left[\frac{\delta_{\mathrm{sc}}}{z f_{\hat{\mathbf{p}}} a}\tanh\frac{z f_{\hat{\mathbf{p}}} a}{\delta_{\mathrm{sc}}}\right] \;\;;\;\; a = \frac{a_0 + \sinh^2\frac{z}{\delta_{\mathrm{sc}}}}{\cosh^2\frac{z}{\delta_{\mathrm{sc}}}} \tag{15}$$

Here we have defined $a_0 = \sqrt{21\zeta(3)/8\mathrm{e}^{2\gamma}} = 0.9973454\ldots$, $\zeta(3)$ and γ denote the Riemann ζ function and Euler's constant [19], respectively. The function $a = a(z)$ interpolates smoothly between the GL limit (where $a = a_0$) and the low–T limit (where $a = 1$). The approximate form of the gap function $\Delta^{\mathrm{E}}_0(T)$ reads:

$$\frac{\Delta^{\mathrm{E}}_0(z)}{k_{\mathrm{B}}T_{\mathrm{c}}} = z\mathrm{e}^{-\left\langle f^2_{\hat{\mathbf{p}}} b^{\mathrm{E}}_{\hat{\mathbf{p}}}(z)\right\rangle_{\mathrm{FS}}} = \frac{\delta_{\mathrm{sc}}}{a}\mathrm{e}^{-c_{\mathrm{E}}(z)} \;\;;\;\; c_{\mathrm{E}}(z) = -\left\langle f^2_{\hat{\mathbf{p}}}\ln\tanh\frac{z f_{\hat{\mathbf{p}}} a}{\delta_{\mathrm{sc}}}\right\rangle_{\mathrm{FS}} \tag{16}$$

and, due to the form of $a(z)$, is seen to display both the correct GL and low temperature limiting behavior, respectively. For a physical motivation of the approximate form $\Delta^{\mathrm{E}}_0(T)$, we point out that for isotropic gaps ($f_{\hat{\mathbf{p}}} = 1$) Eq. (16) assumes the simple form [20]

$$\Delta^{\mathrm{E}}_0(T) = \Delta_0(0)\tanh\left[\left(\Delta^{\mathrm{E}}_0(T)/\Delta_0(0)\right)(T_{\mathrm{c}}/T)\right] \tag{17}$$

From $b^{\mathrm{E}}_{\hat{\mathbf{p}}}(z)$ we may readily obtain the subsequent approximation for the Yosida function $y_{\hat{\mathbf{p}}}(z)$:

$$y^{\mathrm{E}}_{\hat{\mathbf{p}}}(z) = 1 - z\frac{b^{\mathrm{E}}_{\hat{\mathbf{p}}}(z)}{dz} = \frac{2z f_{\hat{\mathbf{p}}} a}{\delta_{\mathrm{sc}}\sinh\frac{2z f_{\hat{\mathbf{p}}} a}{\delta_{\mathrm{sc}}}} \tag{18}$$

as well as an approximation for $y^{\sigma}_{\hat{\mathbf{p}}}(z)$ (c.f. Eq. (4))

$$y^{\sigma\mathrm{E}}_{\hat{\mathbf{p}}}(z) = 1 - \frac{3f^2_{\hat{\mathbf{p}}}}{\pi^2}\int_0^z dz' z' y^{\mathrm{E}}_{\hat{\mathbf{p}}}(z') \tag{19}$$

In the GL regime, the functions $b^{\mathrm{E}}_{\hat{\mathbf{p}}}(z)$, $y^{\mathrm{E}}_{\hat{\mathbf{p}}}(z)$ and $y^{\mathrm{E}\sigma}_{\hat{\mathbf{p}}}(z)$ are seen to agree with their exact counterparts (13) to leading order in the quantity $\zeta_{\hat{\mathbf{p}}}$. In the opposite limit of low temperatures the result for $\Delta^{\mathrm{E}}_0(0)$ agrees with the exact result (14). The accuracy of the approximation can be checked using the spin susceptibility of unconventional superconductors in the low temperature limit as an example. The exact result for the low–T power laws can be summarized as [1]:

$$\lim_{z\to\infty}\frac{\chi_s(z)}{\chi_{\mathrm{N}}} = \lim_{z\to\infty}\left\langle y_{\hat{\mathbf{p}}}(z)\right\rangle_{\mathrm{FS}} = c_f\left(\frac{1}{\alpha_f z}\right)^{\mu_f} \tag{20}$$

In some detail, the results for the coefficients c_f read [1] $c_f = \pi^2/3$ (axial), $c_f = \pi\ln 2$ (polar, hybrid–d), $c_f = 3\pi\ln 2/2$ (hybrid–f) and $c_f = 2\ln 2$ ($d_{x^2-y^2}$). The corresponding temperature exponents are $\mu_f = 2$ (axial) and $\mu_f = 1$ (polar, hybrid–d, hybrid–f, $d_{x^2-y^2}$). The spin susceptibility obtained from $y^{\mathrm{E}}_{\hat{\mathbf{p}}}(z)$ can be written in the asymptotic low temperature limiting form:

$$\lim_{z\to\infty}\frac{\chi^{\mathrm{E}}_s(z)}{\chi_{\mathrm{N}}} = \lim_{z\to\infty}\left\langle y^{\mathrm{E}}_{\hat{\mathbf{p}}}(z)\right\rangle_{\mathrm{FS}} = c_f\left(\frac{d_{\mu_f}}{\alpha_f z}\right)^{\mu_f} \tag{21}$$

The numerical values for the correction factors d_{μ_f} read for the spin susceptibility:

$$\begin{aligned} d_1 &= \pi\delta_{\mathrm{sc}}/8\ln 2 = 0.999315720\ldots \\ d_2 &= (3/2\mathrm{e}^{\gamma})\sqrt{7\zeta(3)/6} = 0.9973454\cdots \equiv (0.994697847\ldots)^{\frac{1}{2}} \equiv a_0 \end{aligned}$$

The accuracy of the approximations for the spin susceptibility is thus seen to depend exclusively on the exponent μ_f of the power law under consideration. It is excellent (0.07%) in the case $\mu_f = 1$ (line nodes dominating) and very good (0.5%) in the case $\mu_f = 2$ (point nodes).

In order to visualize the intriguing accuracy of the approximate forms for $y_{\hat{\mathbf{p}}}(z)$ and $y^{\sigma}_{\hat{\mathbf{p}}}(z)$, we have plotted in Fig. 1 the normalized spin susceptibility $\chi_s(z)/\chi_N = \langle y_{\hat{\mathbf{p}}}(z)\rangle_{FS}$ (left panel) and the normalized entropy density $\sigma(z)/\sigma_N = \langle y^{\sigma}_{\hat{\mathbf{p}}}(z)\rangle_{FS}$ (right panel) for the polar state characterized by $f_{\hat{\mathbf{p}}} = \cos\theta$ (c.f. Eq. (3)) as a function of $z = \Delta_0/k_BT$. While the full lines represent the exact numerical results (7) and (5), the grey dashed lines correspond to an evaluation of $\langle y^{E}_{\hat{\mathbf{p}}}(z)\rangle_{FS}$ and $\langle y^{E\sigma}_{\hat{\mathbf{p}}}(z)\rangle_{FS}$, respectively. Finally, the black dashed lines correspond to the exact asymptotic low–T (large–z) power–law behavior of $\chi_s(z)/\chi_N = \pi\ln 2/\sqrt{3}z$ and $\sigma(z)/\sigma_N = 27\zeta(3)/4\pi\sqrt{3}z$, respectively.

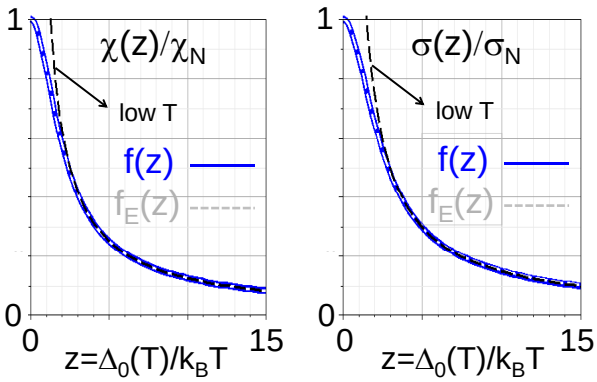

Figure 1: The temperature–dependent BCS functions $f(z) = \chi(z)/\chi_N$ (left panel) and $f(z) = \sigma(z)/\sigma_N$ (right panel) for superconductors with line nodes (here represented by the polar state), plotted vs. $z = \Delta_0(T)/k_BT$. Also shown are their approximate forms $f_E(z)$ and their low–T limiting forms as dashed lines.

Summary and conclusion

For the convenience of experimental physicists, we have presented for the first time analytic expressions for the energy gap function $\Delta_0(z)$ and the two quasiparticle Yosida functions $y_{\hat{\mathbf{p}}}(z)$ and $y^{\sigma}_{\hat{\mathbf{p}}}(z)$. From these all relevant thermostatic and local response functions can be determined for unconventional weakly coupled BCS superconductors as a function of $z = \Delta_0/k_BT$ and T/T_c by simple Fermi surface averaging. In this spirit, Eqs. (15), (18) and (19) form the central results of this contribution. The approximations for the response functions are surprisingly accurate, as could be exemplified in the case of the BVQP spin susceptibility. For lack of space, we can not show here the results for the specific heat capacity, the normal fluid density tensor and the associated components of the magnetic penetration depth. These results will be topic of a forthcoming publication. Generally speaking, the results of this paper can not only be extended to apply to multi–band superconductors [21] like MgB_2, and iron arsenide systems [22, 23], they can also be applied to the huge class of unconventional superconductors, such as organic molecular metals [24, 25], Heavy Fermion systems [26, 27], cuprates [28], Sr_2RuO_4, [29] and non–centrosymmetric superconductors [30, 31], most of which are, even at present, still the subject of extensive research.

References

[1] D. Einzel, J. Low Temp. Phys. **126**, 867–879 (2002).
[2] D. Einzel, J. Low Temp. Phys. **130**, 493–508 (2003).
[3] D. Einzel, J. Low Temp. Phys. **131**, 1–24 (2003).
[4] D. Einzel, M. Englbrecht, and P. Schmidt. The relevance of the Yosida function for a microscopic two–fluid description of superconductivity. Submitted for publication in J. Low Temp. Phys. (2014).
[5] J. Bardeen, L. N. Cooper, and J. R. Schrieffer, Phys. Rev. **108**, 1175–1204 (1957).
[6] N. N. Bogoliubov, Sov. Phys. JETP **7**, 41 (1958).
[7] N. N. Bogoliubov, Nuovo Cimento **7**, 794 (1958).
[8] J. G. Valatin, Nuovo Cimento **7**, 843 (1958).
[9] R. Balian, and N. R. Werthamer, Phys. Rev. **131**, 1553–1564 (1963).
[10] C. Pethick, and D. Pines, Phys. Rev, Lett. **57**, 118–121 (1986).
[11] P. W. Anderson, and P. Morel, Phys. Rev. **123**, 1911–1934 (1961).
[12] D. Einzel, P. J. Hirschfeld, F. Gross, B. S. Chandrasekhar, K. Andres, H. R. Ott, J. Beuers, Z. Fisk, and J. L. Smith, Phys. Rev. Lett. **56**, 2513–2516 (1986).
[13] F. Gross, B. S. Chandrasekhar, D. Einzel, K. Andres, P. J. Hirschfeld, H. R. Ott, J. Beuers, Z. Fisk, and J. L. Smith, Z. Phys. B **64**, 175–188 (1986).

[14] F. Groß-Alltag, B. S. Chandrasekhar, D. Einzel, P. J. Hirschfeld, and K. Andres, Z. Phys. B **82**, 243–255 (1991).
[15] P. J. Hirschfeld, P. Wölfle, and D. Einzel, Phys. Rev. B **37**, 83 –97 (1988).
[16] K. A. Park, and R. Joynt, Phys. Rev. Lett. **74**, 4734–4737 (1995).
[17] J. A. Sauls, J. Low Temp. Phys. **95**, 153–168 (1994).
[18] M. Sigrist, and T. M. Rice, Z. Phys. B **68**, 9–14 (1987).
[19] M. Abramowitz, and I. A. Stegun (eds.) *Handbook of Mathematical Functions* (Dover Inc., New York, 1965).
[20] D. J. Thouless, Phys. Rev. **117**, 1256–1260 (1960).
[21] M. Zehetmayer, Supercond. Sci. Technol. **26**, 1–36 (2013).
[22] H. Oh, J. Moon, D. Shin, C.-Y. Moon, and H. J. Choi, Progress in Superconductivity **13**, 65–84 (2011).
[23] P. J. Hirschfeld, M. M. Korshunov, and I. I. Mazin, Rep. Prog. Phys. **74**, 1–44 (2011).
[24] N. Toyota, M. Lang, and J. Müller (eds.) *Low-Dimensional Molecular metals* (Springer Series in Solid State Siences 154, berlin, Heidelberg, 2007).
[25] A. Ardavan, S. Brown, S. Kagoshima, K. Kanoda, K. Kuroki, H. Mori, M. Ogata, S. Uji, and J. Wosnitza, J. Phys. Soc. Jpn. **81**, 011004–1–27 (2012).
[26] R. Joynt, and L. Taillefer, Rev. Mod. Phys. **74**, 235–294 (2002).
[27] C. Pfleiderer, Rev. Mod. Phys. **81**, 1551–1624 (2009).
[28] M. R. Norman, and C. Pépin, Rep. Prog. Phys. **66**, 1547–1610 (2003).
[29] A. Mackenzie, and Y. Maeno, Rev. Mod. Phys. **75**, 657–712 (2003).
[30] M. Sigrist, AIP Conference Proceedings **1162**, 55 (2009).
[31] E. Bauer, and M. Sigrist (eds.) *Non–centrosymmetric superconductors* (Springer, Lecture Notes in Physics 847, Heidelberg, 2012).

Perspectives of high-T_c superconductivity

R. Hackl, A. Baum, T. Böhm, F. Kretzschmar, M. Rehm, A. Walter [1]
T. P. Devereaux, [2,3] *B. Moritz,* [4] *A. F. Kemper* [5]

Superconductors have always been discovered by materials scientists who usually followed empirical rules or considerations [1–3], while the prediction of new compounds and their superconducting properties such as the transition temperature T_c turned out to be elusive. Only in elements and already existing conventional superconductors like MgB_2 the derivation of T_c from first principles was successful recently [4, 5]. In the case of compounds with transition temperatures in the 50–150 K range, having other phases in close proximity to superconductivity, first-principles calculations are still far from being feasible [6]. So empirical considerations remain to be the only guide in the maze of uncountable possible materials [7]. One of these new rules, replacing those formulated by Matthias, derives from the striking fact that superconductivity with high T_c occurs in materials with magnetic phases close by. To make things even more complicated (or interesting) other instabilities continue to pop up [8–10] without unveiling their relationship to superconductivity.

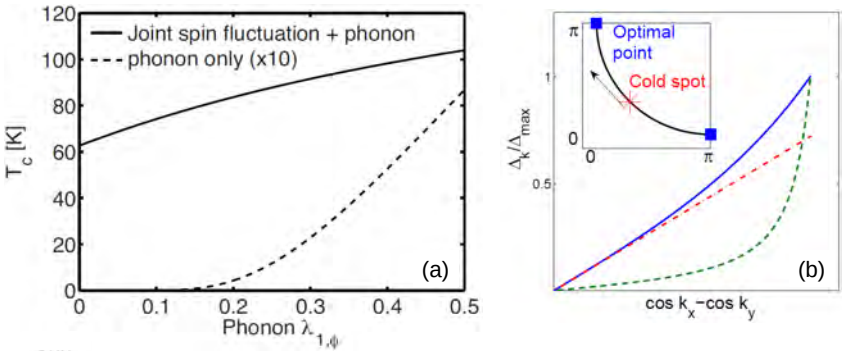

Figure 1: Effects of multichannel superconductivity. (a) Predicted enhancement of T_c in cuprates for a combination of spin-fluctuation and electron-phonon (e-p) coupling [11]. The joint T_c (solid line) increases by 40 K whereas the T_c from e-p coupling alone reaches only 8 K (dashes). (b) Anisotropic enhancement of the energy gap in the presence of nematic critical fluctuations [12]. The solid and dashed lines represent the weak and strong coupling limits, respectively, for the $d_{x^2-y^2}$ gap of the cuprates.

While all these considerations focus essentially on bulk materials with a single mechanism inducing Cooper pairing there are various proposals suggesting multichannel superconductivity. This discussion has in fact a long history [13] but was fueled recently by the discovery of large energy gaps and transition temperatures in monolayer FeSe on $SrTiO_3$ substrates [14, 15]. Here the interface plays an important role in that phonons in $SrTiO_3$ may enhance the moderate T_c of FeSe [16]. However, a similar boost by phonons was suggested also for bulk cuprates in order to explain the material dependence of the maximal transition temperature [11]. So multichannel superconduc-

[1] The project is funded by the German Research Foundation (DFG) via the Priority Program SPP 1458 (Grant-No. HA 2071/7-2) and partially via the Transregional Collaborative Research Center TRR 80. Additional support came from the Bavarian Californian Technology Center (BaCaTeC, project no. A5 [2012-2]). R.H. thanks the Stanford Institute for Materials and Energy Sciences (SIMES), SLAC National Accelerator Laboratory, and the Geballe Laboratory for Advanced Materials (GLAM), Stanford University, for hospitality in the period September 2 to November 26, 2014.

[2] Stanford Institute for Materials and Energy Sciences, SLAC National Accelerator Laboratory, 2575 Sand Hill Road, Menlo Park, CA 94025, USA. Work in the Stanford Institute for Materials and Energy Sciences (SIMES) at Stanford and SLAC was supported by the US Department of Energy, Office of Basic Energy Sciences, Division of Materials Sciences and Engineering, under Contract No. DE-AC02-76SF00515.

[3] Geballe Laboratory for Advanced Materials & Dept. of Applied Physics, Stanford University, CA 94305, USA.

[4] Stanford Institute for Materials and Energy Sciences, SLAC National Accelerator Laboratory, 2575 Sand Hill Road, Menlo Park, CA 94025, USA

[5] Lawrence Berkeley National Laboratory, 1 Cyclotron Road, Berkeley, CA 94720, USA

tivity is not necessarily an exotic phenomenon and may be of particular relevance in systems where unconventional mechanisms dominate since phonons, for instance, are omnipresent.

Fig. 1 (a) shows the effect of electron-phonon (e-p) coupling on the maximal transition temperature in cuprates [11]. The basic coupling mechanism is assumed to result from spin fluctuations and to induce superconductivity at $T_c = 62\,\mathrm{K}$ with coupling constants $\lambda_{\mathrm{spin}} = 0.5$ and $\lambda_{\mathrm{e-p}} = 0$. If $\lambda_{\mathrm{e-p}}$ is cranked up to match λ_{spin} the total T_c reaches 103 K. Similarly, close to a quantum critical point nematic, i.e., quadrupolar, fluctuations at $\mathbf{q} = 0$ were shown to enhance T_c [12]. The explanation of the results in FeSe follows exactly these lines with the only exception that the phonon enhancement originates from the $SrTiO_3$ lattice and not from the bulk [16]. This reasoning brings hetero-structures back into focus of the search for new materials, as suggested for the first time some 50 years ago [17, 18], and, in a way, highlights contact points and potential synergies between two of the coordinated programs the WMI participates in: the Priority Program "Pnictide Superconductors" (SPP 1458) and the Collaborative Research Center "From Correlations to Functionalities" (TRR 80).

Can one experimentally access different mechanisms and their contributions? In isotropic systems the McMillan-Rowell inversion was a very successful instrument for determining the e-p coupling spectra in lead [19] and various other strong-coupling conventional systems. In anisotropic systems having more than one mechanism the minimum requirement is a technique that facilitates momentum resolution. Beyond that there is no general recipe. One possible approach was demonstrated recently: Raman light scattering from electrons can provide an effective tool for identifying and quantifying competing pairing channels through the observation and analysis of various modes in the superconducting state [20–22]. Usually, one can observe the gap via pair breaking effects. If the pairing potential is anisotropic, in-gap modes can appear as a consequence of competing interaction channels. They are similar in origin to excitons in semiconductors [23–25], and the distance from the gap edge encodes the relative strength of the subdominant channel to the ground state. Fig. 2 shows a schematic representation of how a typical Raman spectrum is composed. The left two panels visualize the usual pair-breaking effect being a coherent superposition of the normal (creating a particle-hole pair across the gap) and the anomalous (breaking a Cooper pair) part of the Nambu-Green function. The right panel shows schematically how a broken Cooper pair can reform into an exciton having a symmetry orthogonal to that of the ground state. Formally the response results from a vertex correction and can be derived by solving a Bethe-Salpeter equation [25, 26].

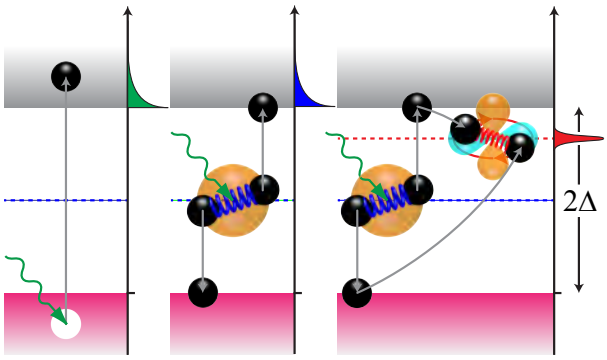

Figure 2: Schematics of excitation levels in the presence of different pairing channels. The left two panels show the usual pair-breaking effect, the right panel shows the effect of exciton formation in a superconductor that is a higher-order correction to the pair-breaking effect.

The experimental result summarized here is far from answering the question as to multi-channel pairing in the Fe-based superconductors but may (i) outline paths towards a better understanding of pairing mechanisms in complex systems and (ii) pave the way for new studies of materials engineering in unconventional superconductors.

References

[1] B. Matthias, Phys. Rev. **97**, 74–76 (1955).

[2] J. G. Bednorz, and K. A. Müller, Z. Phys. B **64**, 189 (1986).
[3] W. E. Pickett, Physica B **296**, 112–119 (2001). Proceedings of the Symposium on Wave Propagation and Electronic Structure in Disordered Systems.
[4] M. Lüders, M. A. L. Marques, N. N. Lathiotakis, A. Floris, G. Profeta, L. Fast, A. Continenza, S. Massidda, and E. K. U. Gross, Phys. Rev. B **72**, 024545 (2005).
[5] A. Floris, G. Profeta, N. N. Lathiotakis, M. Luders, M. A. L. Marques, C. Franchini, E. K. U. Gross, A. Continenza, and S. Massidda, Phys. Rev. Lett. **94**, 037004 (2005).
[6] E. K. U. Gross. Private communication (2012).
[7] I. I. Mazin, Nature **464**, 183 (2010).
[8] J. Tranquada, B. Sternlieb, J. Axe, Y. Nakamura, and S. Uchida, Nature **375**, 561 (1995).
[9] G. Ghiringhelli, M. Le Tacon, M. Minola, S. Blanco-Canosa, C. Mazzoli, N. B. Brookes, G. M. De Luca, A. Frano, D. G. Hawthorn, F. He, T. Loew, M. M. Sala, D. C. Peets, M. Salluzzo, E. Schierle, R. Sutarto, G. A. Sawatzky, E. Weschke, B. Keimer, and L. Braicovich, Science **337**, 821–825 (2012).
[10] R. M. Fernandes, A. V. Chubukov, and J. Schmalian, Nature Phys. **10**, 97 (2014).
[11] S. Johnston, F. Vernay, B. Moritz, Z.-X. Shen, N. Nagaosa, J. Zaanen, and T. P. Devereaux, Phys. Rev. B **82**, 064513 (2010).
[12] S. Lederer, Y. Schattner, E. Berg, and S. A. Kivelson (2014). arXiv:1406.1193.
[13] H. Suhl, B. T. Matthias, and L. R. Walker, Phys. Rev. Lett. **3**, 552–554 (1959).
[14] Q.-Y. Wang, Z. Li, W.-H. Zhang, Z.-C. Zhang, J.-S. Zhang, W. Li, H. Ding, Y.-B. Ou, P. Deng, K. Chang, J. Wen, C.-L. Song, K. He, J.-F. Jia, S.-H. Ji, Y.-Y. Wang, L.-L. Wang, X. Chen, X.-C. Ma, and Q.-K. Xue, Chin. Phys. Lett. **29**, 037402 (2012).
[15] W. Zhang, Z. Li, F. Li, H. Zhang, J. Peng, C. Tang, Q. Wang, K. He, X. Chen, L. Wang, X. Ma, and Q.-K. Xue, Phys. Rev. B **89**, 060506 (2014).
[16] J. J. Lee, F. T. Schmitt, R. G. Moore, S. Johnston, Y.-T. Cui, W. Li, M. Yi, Z. K. Liu, M. Hashimoto, Y. Zhang, D. H. Lu, T. P. Devereaux, D.-H. Lee, and Z.-X. Shen, Nature **515**, 245 (2014).
[17] W. A. Little, Phys. Rev. **134**, A1416 (1964).
[18] D. Allender, J. Bray, and J. Bardeen, Phys. Rev. B **7**, 1020 (1973).
[19] W. L. McMillan, and J. M. Rowell, Phys. Rev. Lett. **14**, 108 (1965).
[20] F. Kretzschmar, B. Muschler, T. Böhm, A. Baum, R. Hackl, H.-H. Wen, V. Tsurkan, J. Deisenhofer, and A. Loidl, Phys. Rev. Lett. **110**, 187002 (2013).
[21] T. Böhm, F. Kretzschmar, R. Hackl, A. F. Kemper, and T. P. Devereaux, WMI Ann. Rep. **2013**, 39–40 (2013).
[22] T. Böhm, A. F. Kemper, B. Moritz, F. Kretzschmar, B. Muschler, H.-M. Eiter, R. Hackl, T. P. Devereaux, D. J. Scalapino, and H.-H. Wen (2014). Accepted for publication in Phys. Rev. X, arXiv:1409.6815.
[23] A. Bardasis, and J. R. Schrieffer, Phys. Rev. **121**, 1050–1062 (1961).
[24] M. V. Klein, and S. B. Dierker, Phys. Rev. B **29**, 4976 (1984).
[25] H. Monien, and A. Zawadowski, Phys. Rev. B **41**, 8798 (1990).
[26] D. J. Scalapino, and T. P. Devereaux, Phys. Rev. B **80**, 140512 (2009).

Phase diagrams and superconductivity of κ-$(BETS)_2FeBr_4$

L. Schaidhammer, M. Kunz, W. Biberacher, M. V. Kartsovnik [1]
N. D. Kushch [2]

Last year we reported on the properties of the antiferromagnetic (AFM) phase of the organic charge transfer salt κ-$(BETS)_2FeCl_4$ in a magnetic field [1]. Here we present our studies on the sister compound κ-$(BETS)_2FeBr_4$, which shows stronger magnetic interactions and, therefore, has a higher Néel temperature $T_N = 2.5\,K$. In addition, this compound undergoes a superconducting (SC) transition with a critical temperature $T_c = 1.4\,K$. Therefore, the effect of the stronger magnetism and its interplay with the SC state were studied.

For the experiment plate-like samples of κ-$(BETS)_2FeBr_4$ were contacted in the interlayer magnetoresistance geometry, mounted on a two-axes rotator and cooled down in a ^{3}He system in a SC magnet. For the measurements under pressure the samples were pressurised in a small clamp cell using the silicon oil GKZh as pressure medium. At ambient pressure the B-T phase diagram for fields along the crystallographic a- and c-directions was already studied by Konoike *et al.* [2] by means of resistance measurements. We obtained the phase boundary for magnetic field along the b-direction (perpendicular to the conducting layers) by torque and resistance measurements and completed the phase diagram along the a-direction by resistance measurements. In Fig. 1 our data (filled symbols) is compared with the data from [2] (empty symbols). The triangles were obtained from resistance and the diamonds from torque measurements. The inset shows the temperature dependence of resistance for zero field. As we can see, the phase line for $B \parallel b$-axis almost coincides with $B \parallel c$-axis. Thus, the behaviour is different from that of κ-$(BETS)_2FeCl_4$ where a considerable b-c anisotropy was observed [1]. For $B \parallel a$-axis only one transition from the SC to normal metallic state is visible, suggesting that both the SC and AFM states are broken at the same time. As only one feature is visible, there is no sign for a spin-flop state unlike in κ-$(BETS)_2FeCl_4$ [1].

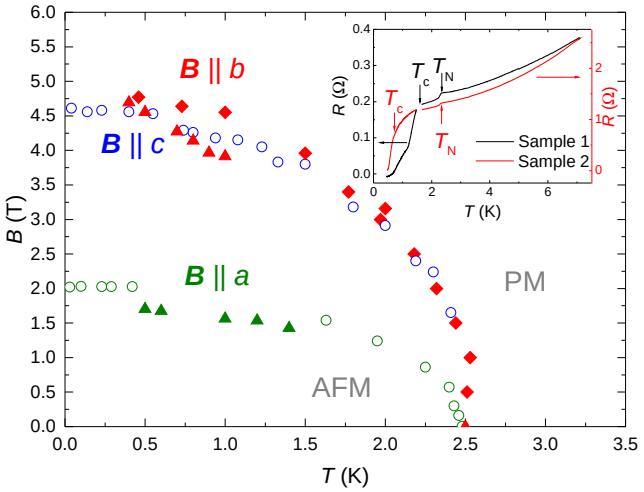

Figure 1: Phase diagram of κ-$(BETS)_2FeBr_4$ for different field directions. Symbols are explained in the text. The inset shows $R(T)$ at zero field for two different samples.

We further measured the B-T phase diagram under hydrostatic pressure to evaluate the pressure dependence of the AFM state. Otsuka *et al.* [3] already studied the pressure dependence of the Néel temperature T_N and the critical temperature T_c showing that the later decreases with increasing pressure and vanishes at 4 kbar, while the AFM state is enhanced at higher pressures. Our studies now reveal the full phase diagrams for all crystal axes. The phase diagrams for the a (red triangles) and c directions (black circles) are shown in Fig. 2 for pressures $p = 1.9\,kbar$ (empty symbols) and 4.5 kbar (filled symbols). For $B \parallel b$-axis the transition was not visible in a large part of the phase diagram and is therefore not shown. The SC state was already completely suppressed at $p = 1.9\,kbar$ in the sample studied (sample 2 in the inset of Fig. 1).

[1] This work was supported by the German Research Foundation via Grant-No. KA 1652/4-1.
[2] Institute of Problems of Chemical Physics, 142432 Chernogolovka, Russia

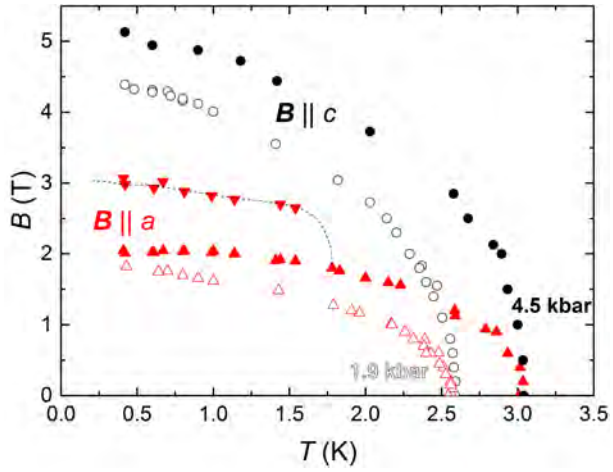

Figure 2: Phase diagram of κ-$(BETS)_2FeBr_4$ for $B \| a, c$ at two different pressures. Symbols are explained in the text.

At $p = 1.9$ kbar the phase diagram is almost the same as at ambient pressure. At 4.5 kbar the AFM state is considerably enhanced: Both T_N and critical fields shift to higher values. While for $B \parallel c$-axis the shift of the phase boundary looks very regular, there is a considerable change in the behaviour of the AFM state for $B \parallel a$. Here the temperature dependence of the transition field is strongly flattened for $T < 1.5$ K. Further, at this pressure a second feature starts to appear in field sweeps below 1.5 K (inverted triangles), which could indicate a spin-flop phase. However, we were not able to verify the phase boundary line by temperature sweeps.

We have also investigated the SC and FISC states of κ-$(BETS)_2FeBr_4$. Fig. 3 shows a field sweep for $B \parallel a$ where both the combined SC and AFM transition at 1.7 T and the FISC region centered at 12 T are visible. The sample does not become fully superconducting in the middle of the FISC state at this temperature. However, this, as well as the general behaviour, is in agreement with the reported results [2], where a zero resistance state was only observed at $T < 0.3$ K.

In the top left inset of Fig. 3 an angular sweep at $B = 12$ T and $T = 0.5$ K is shown. It shows how narrow the FISC angular range is. A similar angular sweep within the bc-plane was performed while the magnetic torque of the sample was measured (see the bottom right inset of Fig. 3). While the black curve recorded at 1.4 K shows no feature at field parallel to the layers, the red curve with $T = 0.5$ K shows a loop-like feature around parallel orientation, which we correlate with the FISC state setting in below 1 K. The feature is seen in a very narrow angular range ($\pm 0.1°$) in torque. Therefore, we assume that it might be due to a lock-in transition. This is, to our knowledge, the first thermodynamic evidence for a FISC transition in κ-$(BETS)_2FeBr_4$.

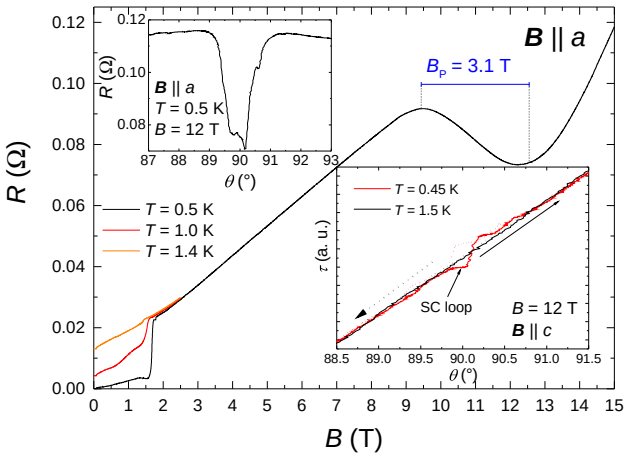

Figure 3: $R(B)$ for $B \| a$-axis at different Temperatures. The top left inset shows $R(\theta)$ in the ac-plane. The bottom right inset shows $\tau(\theta)$ in the bc-plane for different temperatures.

References

[1] M. Kunz, W. Biberacher, K. Neumaier, N. D. Kushch, and M. V. Kartsovnik, WMI Ann. Rep. **2013**, 52–53 (2013).

[2] T. Konoike, S. Uji, T. Terashima, M. Nishimura, S. Yasuzuka, K. Enomoto, H. Fujiwara, B. Zhang, and H. Kobayashi, Phys. Rev. B **70**, 094514 (2004).

[3] T. Otsuka, H. Cui, H. Fujiwara, H. Kobayashi, E. Fujiwara, and A. Kobayashi, J. Mater. Chem. **14**, 1682–1685 (2004).

Quantum and angular magnetoresistance oscillations κ-(BETS)$_2$FeBr$_4$

L. Schaidhammer, M. Kunz, W. Biberacher, M. V. Kartsovnik [1]
N. D. Kushch [2]

The organic metal κ-(BETS)$_2$FeBr$_4$ is an antiferromagnet with a Néel temperature $T_N = 2.5\,K$, which remains metallic below the antiferromagnetic (AFM) transition and even becomes superconducting (SC) at a critical temperature $T_c = 1.4\,K$ (see contribution on page 47). Here we report studies of Shubnikov-de Haas (SdH) oscillations in the normal metallic and AFM states for different field angles and of angular magnetoresistance oscillations (AMRO) in order to obtain information on the impact of the AFM ordering on the Fermi surface.

First, a series of measurements at ambient pressure was performed. Fig. 1 shows an example of a field sweep for B perpendicular to the conducting layers. The black and blue curves show the up- and down-sweeps, respectively. At $B \approx 5\,T$ a kink-like feature reflects the transition from the AFM to the paramagnetic state. Above the transition, for fields higher than 9 T SdH oscillations become visible. The top right inset shows the fast Fourier transform (FFT) spectrum for two measured samples. The observed frequencies $F_\alpha = 853\,T$ and $F_\beta = 4260\,T$ are in agreement with previous reports [1] and can be assigned to the classical α-orbit and the magnetic breakdown β-orbit on the Fermi surface. Additionally visible are frequencies $F_\beta - F_\alpha$ and $F_\beta - 2F_\alpha$, which are the result of a quantum interference effect, and the frequency $F_\gamma = 103\,T$ of still unknown origin.

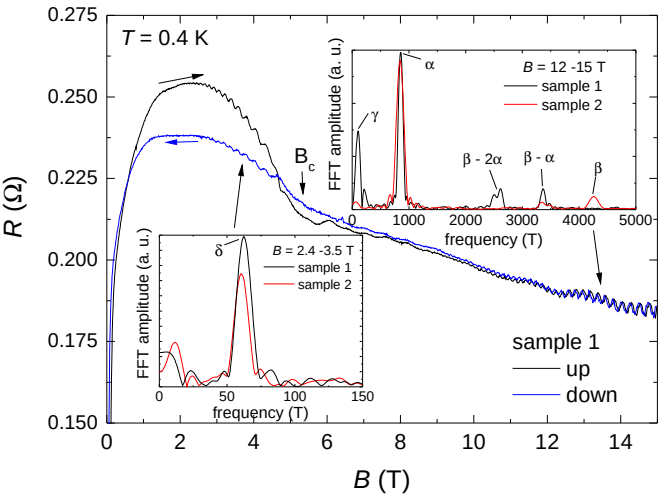

Figure 1: Field sweeps (up and down) at $T = 0.4\,K$ with the magnetic field perpendicular to the conducting planes. The insets show the FFT spectrum of the SdH oscillations visible below the AFM transition and in the high field region, respectively.

Below the AFM transition another set of SdH oscillations, denoted as δ oscillations, is visible, with $F_\delta \approx 62\,T$. The cyclotron mass of this orbit was determined as $1.08\,m_0$, where m_0 is the free electron mass. These values are again in excellent agreement with an earlier report [1]. The fact that these oscillations only appear in the AFM phase and completely vanish above the transition indicates a Fermi surface reconstruction in the AFM state. Also a clear hysteresis between the up- and down-sweeps is visible. It is also reflected in the oscillation amplitude. The origin of this hysteresis is not yet clear. It might be caused by some kind of domain structure in the AFM state that results in a change in the spin-dependent scattering rate. In order to acquire more information about the Fermi surface reconstruction in the AFM state, the angular dependence of the δ-oscillations was studied. Several field sweeps at different polar angles θ are shown in the inset of Fig. 2. In Fig. 2 the resulting FFT amplitude is plotted vs. angle. The coloured lines are simulations based on the Lifshitz-Kosevich theory. One of the main goals in this measurement was to check, if there are spin-zeros [2]. Our measurements didn't show any sign for a spin-zero for $\theta \leq 55°$, as as we would expect for $g = 2$ (blue simulation), where g is the Landé factor. However, as the oscillation amplitude was hardly

[1] This work was supported by the German Research Foundation by grant number KA 1652/4-1.
[2] Institute of Problems of Chemical Physics, 142432 Chernogolovka, Russia

resolvable for angles $\theta \geq 55°$ and the spin-zero would be expected at higher angles for smaller g (red simulation), no final conclusion can be drawn yet.

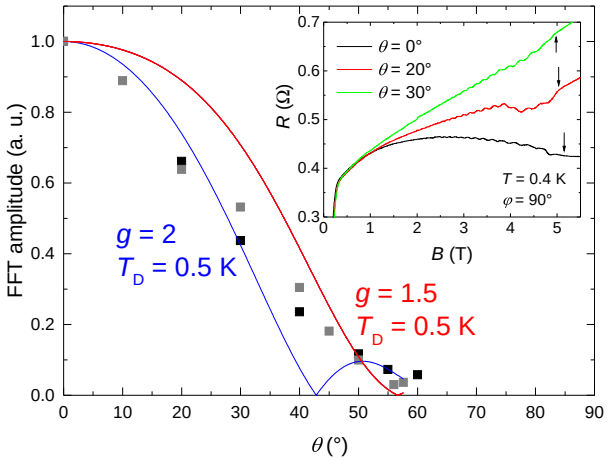

Figure 2: θ-dependence of the SdH oscillation amplitude in the bc-plane. The solid lines are simulated data for different values of g. Inset: Examples of $(R(B)$ curves.

The same studies of SdH oscillations were also done under hydrostatic pressure. At $p = 1.9\,\text{kbar}$ the α and δ oscillations were still visible, however, with decreased amplitudes, while the other frequencies were absent. The cyclotron masses were determined to be $m^*_\alpha = 3.3\,m_0$ (ambient pressure value $m^*_\alpha = 5.2\,m_0$ [1]) and $m^*_\delta = 0.83\,m_0$. The rather strong, $\sim 30\%$, decrease pressure is typical of organic charge transfer salts. At a pressure of 4.5 kbar no SdH oscillations were visible any more. In addition, a series of θ-sweeps at different azimuthal angles $70° \leq \varphi \leq 110°$ and $\varphi = 0°$ ($B \| a$-axis) were performed in order to study angle-dependent magnetoresistance oscillations (AMRO). Fig. 3 shows an example for $\varphi = 70°$. The irregular shape of the oscillations near parallel field orientations ($\theta = 90°$) suggests the existence of more than one set of oscillations.

A closer investigation using FFT analysis indeed revealed that three different sets of oscillatory effects could be resolved: The dominant frequency (which is the only one seen at low θ) was found to originate from the breakdown orbit β (responsible for F_β in the SdH spectrum). For high θ values another set of oscillations starts appearing depending on φ. For φ near 0° the AMRO could be identified as a contribution from the α orbit, while for φ near 90° the oscillations were found to be Lebed Magic Angle resonances [2] associated with the open sheets on the Fermi surface.

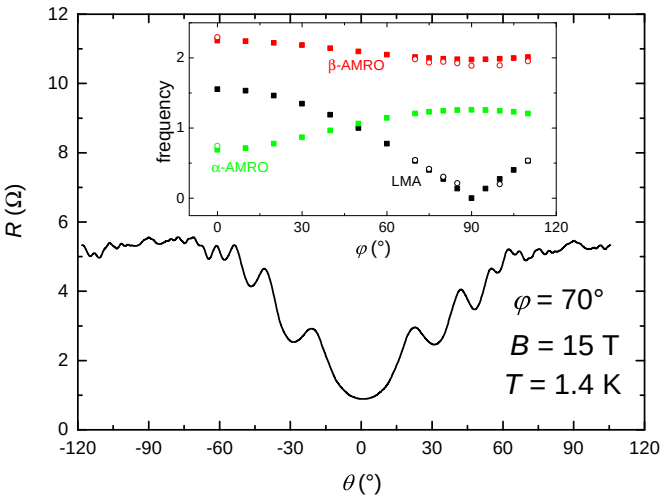

Figure 3: Example of an AMRO. Inset: φ-dependence of the frequencies of different sets of AMRO. The filled symbols show the calculated values; the empty symbols are the experimental data.

The inset in Fig. 3 shows frequencies that could be derived from the experimental data, as far as they could be resolved (empty symbols). The filled symbols show the calculated φ-dependence for each of the three AMRO sets, which are all in excellent agreement with the experimental data.

References

[1] T. Konoike, S. Uji, T. Terashima, M. Nishimura, S. Yasuzuka, K. Enomoto, H. Fujiwara, E. Fujiwara, B. Zhang, and H. Kobayashi, Phys. Rev. B **72**, 094517 (2005).
[2] M. V. Kartsovnik, Chem. Rev. **104**, 5737–5782 (2004).

Application–Oriented Research

Superconducting on-chip microwave interferometer

E. P. Menzel, M. Fischer, C. Schneider, F. Deppe, A. Marx, R. Gross [1]

In a new approach to quantum information processing, the so called all-microwave quantum computation, information is encoded in itinerant microwave photons. Similarly to all-optical quantum computing [1], the qubit states are superpositions of a microwave photon travelling in either one of two transmission lines. In such a system unitary operations are implemented by linear elements, for instance, beam splitters or interferometers. However, for two-qubit operations non-linear gates are required. In this work, we investigate superconducting interferometers as a basic building block for a two-qubit gate.

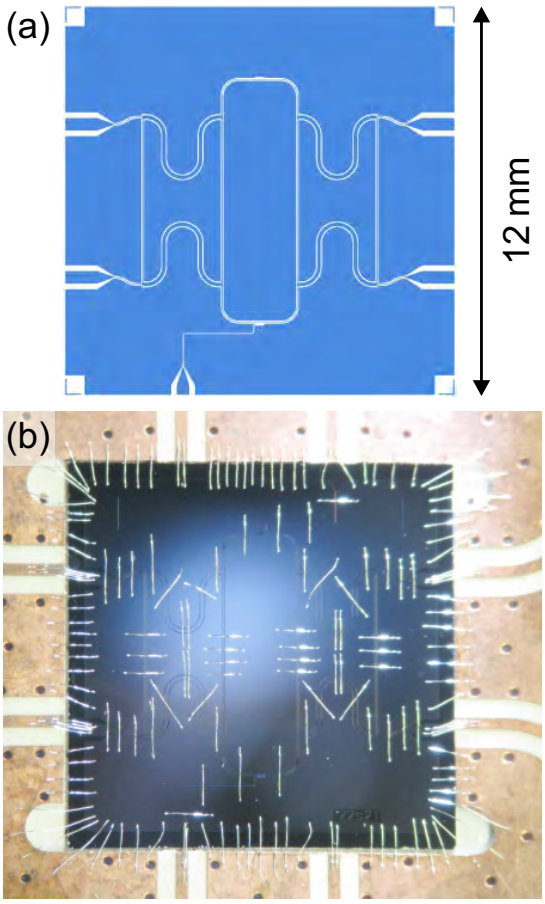

Figure 1: On-chip superconducting interferometer. (a) Sketch of the design of an interferometer with two transmon sites and one antenna. The blue areas denote niobium. (b) Photograph of an interferometer chip embedded in a printed circuit board.

For the implementation of a superconducting interferometer in a planar geometry on a chip, beam splitters with a scalable design and a suitable port configuration are required. The latter point is addressed by 90° hybrid beam splitters which can be easily cascaded to an interferometer without any crossing of transmission lines. In order to reduce the device footprint, we make use of 90° beam splitters with meandered branch lines in an optimized design [2]. The coplanar waveguide design is the natural choice for scalable microwave circuits with low crosstalk. Moreover, it is compatible to various superconducting qubit designs such as transmon or flux qubits. However, in coplanar structures parasitic modes can form at T-junctions or when the waveguides are bent. As a remedy, we connect the ground planes with bonds.

The design of an interferometer with gaps for two transmon qubits and one control antenna is sketched in Fig. 1(a). The device is patterned into a 100 nm thick niobium film via optical lithography and reactive ion etching. The Nb film is deposited on a silicon substrate by magnetron sputtering. In Fig. 1(b), a typical interferometer chip embedded in a printed circuit board is shown.

With various improvements of the measurement setup regarding impedance matching and electromagnetic environment [2, 3], we are able to characterize the fabricated on-chip interferometers. Figure 2 presents our results of the scattering properties of the interferometer measured at 4.2 K. For comparison, also the numerical simulation results of this system are shown [3]. For details on the theoretical model which describes all three measured transmission spectra quite well we refer the interested reader to Ref. [3]. The trend of the measured cross-transmission is similar to the theory

[1] We acknowledge financial support by the German Research Foundation through SFB 631, the German Excellence Initiative through the Nanosystems Initiative Munich (NIM), and the EU projects CCQED and PROMISCE.

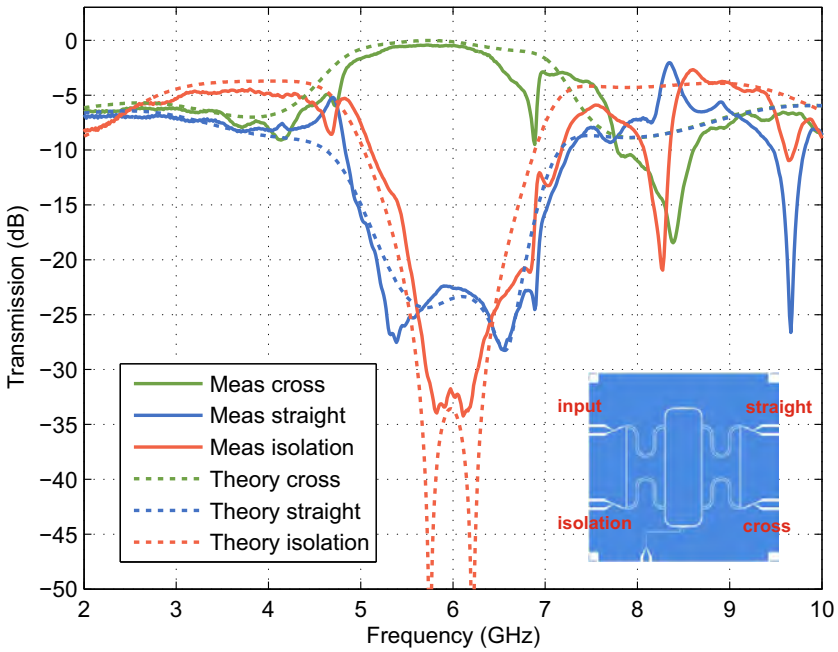

Figure 2: Measured transmission spectra of an interferometer with two transmon sites and one antenna. For comparison, also the numerical simulation results of this system are shown [3]. Inset: sketch of the interferometer design with the port names (red).

prediction, however with a slightly lower transmission of $-0.46\,\mathrm{dB}$ at the operation frequency of $5.75\,\mathrm{GHz}$. This might be due to the empty transmon sites, which change the impedance in the joints between the beam splitters. Around the working frequency the isolation between the two input ports shows two dips with a depth of approximately $-34\,\mathrm{dB}$, in good agreement with theory. Furthermore, the transmission to the straight port is suppressed by more than $22.4\,\mathrm{dB}$. These characteristics are very promising for future applications.

Recently, we have inserted a transmon qubit between the two beam splitters for first experiments towards a two-qubit gate in the spirit of all-microwave quantum computation.

References

[1] J. L. O'Brien, Science **318**, 1567–1570 (2007).
[2] C. M. F. Schneider. *On-chip Superconducting Beam Splitter*. Master's thesis, Technische Universität München (2014).
[3] M. Fischer. *On-chip Superconducting Microwave Interferometer*. Master's thesis, Technische Universität München (2014).

Coupling and decoupling of microwave resonators via an RF-SQUID

F. Wulschner, F. Kössel, E. P. Menzel, F. Deppe, A. Marx, R. Gross[1]

In circuit quantum electrodynamics (QED), Josephson-junction based quantum two level systems (qubits) and superconducting microwave resonators are the fundamental building blocks. In contrast to quantum-optical cavity QED, the large effective dipole moment of superconducting qubits allows for the coupling between qubit and resonator to reach the strong or even the ultra-strong regime [1]. In circuit QED architectures with multiple qubits and resonators, quantum logic gates have been successfully realized [2, 3]. However, while the requirements for such digital quantum computing are still enormous, analog quantum simulation with circuit QED systems appears to be a technologically less demanding and therefore attracts increasing interest. In analog quantum simulations, one mimics the Hamiltonian of a system of interest with a circuit offering a higher degree of controllability than the original system. In this context, one specific proposal is to strongly couple nonlinear resonators to explore Bose-Hubbard physics in the driven-dissipative regime [4, 5]. For such experiments, a scalable approach for the realization of tunable coupling between the resonators is strongly desirable. In this report, we present experimental data in this direction: two LC microwave resonators are coupled via an RF SQUID [6] as depicted in Fig. 1.

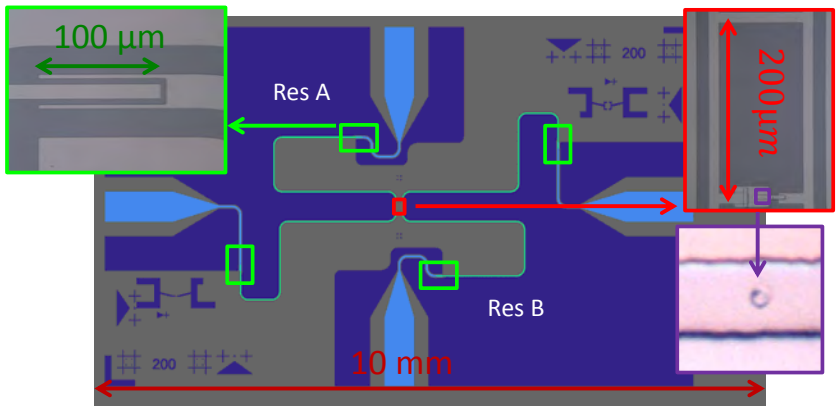

Figure 1: Layout of tunable coupler using a RF SQUID. Resonator groundplanes are depicted in dark blue, center lines of resonators A& B are painted in light green. Measurement signals are feed into the ports (light blue) which are coupled to the resonators via capacitors (micrograph in green inset). In the center both center lines are galvanically connected to an RF-SQUID (micrograph in red inset), which consists of a superconducting loop intersected by a Josephson junction (micrograph in purple inset)

The RF-SQUID can be treated as an effective mutual inductance which can be manipulated by an external magnetic field. The effective inductance of the RF-SQUID is determined by the change of the circulation currents upon changing the applied field ($1/L = dI/d\Phi$). Due to the sinusoidal dependence of the flux on the circulating currents in an RF-SQUID, one gets a flux depending coupling. In our experiment we also have to take into account that due to the immediate vicinity of the resonators on the chip one has to consider a second geometric coupling channel denoted with g_{geo}. The total coupling of the resonators is given by [6–8]:

$$g(\Phi) = g_{\mathrm{geo}} + g_{\mathrm{RF0}} \frac{\beta \cos(\frac{2\pi\Phi}{\Phi_0})}{1 + \beta \cos(\frac{2\pi\Phi}{\Phi_0})} \tag{1}$$

[1]We acknowledge financial support by the German Research Foundation through SFB 631, the German Excellence Initiative through the Nanosystems Initiative Munich (NIM), and the EU projects CCQED and PROMISCE.

Here $\beta = 2\pi L I_c/\Phi_0$ denotes the screening parameter of the the RF-SQUID, with the loop inductance L and the critical junction current I_c. The parameter β is a measure for the amount of flux which the RF-SQUID induces into itself due to circulating currents in the SQUID loop. The factor g_{RF0} only depends on geometrical properties of the resonator and the SQUID loop.

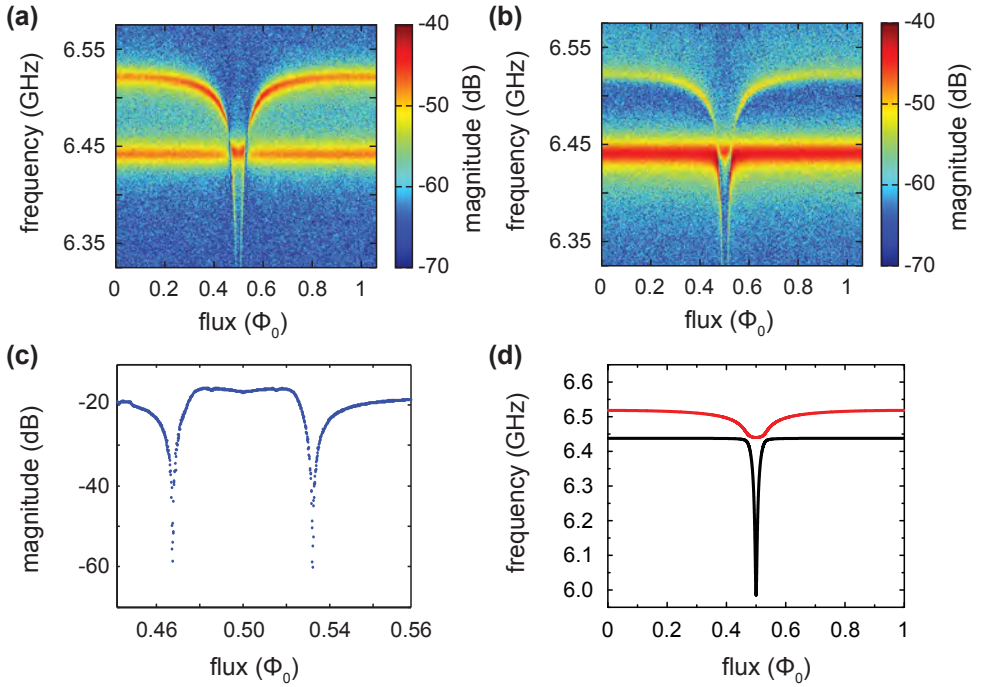

Figure 2: RF SQUID coupler between two superconducting transmission line resonators. (a) Cross transmission (color code) as a function of the external flux (Φ_x) and the probe frequency. (a) As (a), but through transmission through one of the resonators. (c) Cross section from (a) through the flux-independent mode in the "off" region showing deep dips. (d) Calculation of the normal mode energies of the system. Parameters close to those extracted from a fit to the data shown in (a) and (b).

In our experiment we measure the resonator transmission and sweep the magnetic field to change the coupling between the resonators. As expected we observe a flux dependent splitting of the resonator modes caused by the tunable coupling [Fig. 2(a) and Fig. 2(b)]. Furthermore we measure a significant suppression of signal transfer between the resonators in the regime where $g(\Phi) \to 0$ [Fig. 2(c)]. A closer look at the spectra in Fig. 2(a) reveals that both modes show unequal transmission amplitude over a broad range. This is caused by a detuning ($\Delta = \omega_A - \omega_B$) of the fundamental resonator frequencies. This leads to the fact that the collective modes of the system are not equal superpositions of the individual resonator modes. The mode spacing in this case is given by $\Delta\omega = \sqrt{4g(\Phi)^2 + \Delta^2}$. This is also visible in Fig. 2(d) where the eigenfrequencies of the system are plotted vs. the external flux. The minimum mode spacing at the point of decoupling, where the two modes are each localized in one resonator, is given by Δ. Fitting the data we obtain the resonator frequencies $\omega_A = 6.483\,\text{GHz}$ and $\omega_B = 6.459\,\text{GHz}$, the coupling rates $g_{geo} = 22.7\,\text{MHz}$ and $g_{RF} = 22.3\,\text{MHz}$, and a screening parameter $\beta = 0.9$. The total coupling $g(\Phi)$ varies from $< -250\,\text{MHz}$ to $37\,\text{MHz}$, but for large negative coupling values around $\Phi = 0.5$ the lower collective mode is significantly broadened and suppressed due to its steep flux dependence. Therefore, we compare the detuning $\Delta = 24\,\text{MHz}$ to the maximal positive coupling of $g(\Phi = 0) = 37\,\text{MHz}$. Here, the resonator modes mix with a ratio of 0.65:0.35.

In conclusion, despite a significant detuning between our resonators, we can still turn the coupling between them on and off by choosing suitable flux bias points and reach a signifi-

cant mixing of the resonator modes in the coupling case. In contrast to our previous work, where a superconducting flux qubit mediates tunable coupling between two resonators [9], the RF SQUID coupler is more suitable for scalable architectures because of simpler fabrication and higher coupling strength. In future we plan to implement a fast flux antenna for the RF SQUID and transmon qubits in the resonators. This should enable us to perform experiments on parametric amplification and squeezing similar to Ref. [7] or to go in the direction of quantum simulations of bosonic manybody Hamiltonians [10].

References

[1] T. Niemczyk, F. Deppe, H. Huebl, E. P. Menzel, F. Hocke, M. J. Schwarz, J. J. Garcia-Ripoll, D. Zueco, T. Huemmer, E. Solano, A. Marx, and R. Gross, Nature Phys. **6**, 772 (2010).

[2] E. Lucero, R. Barends, Y. Chen, J. Kelly, M. Mariantoni, A. Megrant, P. O. Malley, D. Sank, A. Vainsencher, J. Wenner, T. White, Y. Yin, A. N. Cleland, and J. M. Martinis, Nature **8**, 719 (2012).

[3] A. Fedorov, L. Steffen, M. Baur, M. P. da Silva, and A. Wallraff, Nature **481**, 170–172 (2011).

[4] M. Leib, and M. J. Hartmann, New J. Phys. **12**, 093031 (2010).

[5] M. Leib, F. Deppe, A. Marx, R. Gross, and M. J. Hartmann, New J. Phys. **14**, 075024 (2012).

[6] B. Peropadre, D. Zueco, F. Wulschner, F. Deppe, A. Marx, R. Gross, and J. Garcia-Ripoll, Phys. Rev. B **87** (2013).

[7] L. Tian, M. S. Allman, and R. W. Simmonds, New J. Phys. **10** (2008).

[8] M. S. Allman, F. Altomare, J. D. Whittaker, K. Cicak, D. Li, A. Sirois, J. Strong, J. D. Teufel, and R. W. Simmonds, Phys. Rev. Lett. **104** (2010).

[9] A. Baust, E. Hoffmann, M. Haeberlein, M. J. Schwarz, P. Eder, E. P. Menzel, K. Fedorov, J. Goetz, F. Wulschner, E. Xie, L. Zhong, F. Quijandria, B. Peropadre, D. Zueco, J.-J. Garcia Ripoll, E. Solano, F. Deppe, A. Marx, and R. Gross (2014). arXiv:1405.1969.

[10] J. Raftery, D. Sadri, S. Schmidt, H. E. Türeci, and A. A. Houck, Phys. Rev. X **4**, 031043 (2014).

Circuit quantum electrodynamics with three-dimensional cavities

E. Xie, G. Andersson, L. Wang, J. Müller, F. Deppe, A. Marx, R. Gross[1]

Superconducting quantum circuits have proven to be a promising platform for the implementation of quantum information systems. Typical arrangements are based on the so-called circuit quantum electrodynamics (circuit QED) approach employing on-chip superconducting quantum bits and integrated coplanar microwave resonators. In this configuration, strong and ultrastrong coupling has been demonstrated [1]. Therefore, in general such systems offer an excellent experimental setup to study light-matter interaction. However, there are also several drawbacks. First, due to the open planar geometry of the quasi 1D cavity the qubit remains very sensitive to its electromagnetic environment. Second, the desired high vacuum field amplitude allowing for ultrastrong coupling does not exclusively couple to the qubit, but also to other quantum systems such as two-level fluctuators (TLS) [2]. Therefore, in several experiments the integrated quasi 1D microwave resonators are the limiting factor regarding the total coherence of the system.

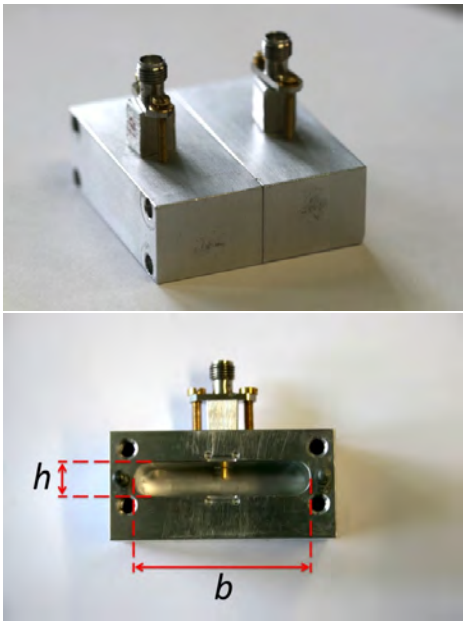

Figure 1: Box-type microwave cavity made of aluminum. Top: Closed cavity with two antennae, screws and spacers. Bottom: Open cavity with dimensions $a = 37.78\,\text{mm}$, $b = 38.46\,\text{mm}$, and $h = 7.4\,\text{mm}$. Each cavity half is $a/2$ deep.

Alternatively, an appropriate superconducting resonator/qubit hybrid system can also be realized by employing three-dimensional, box-type microwave cavities (cf. Fig. 1). The design of our box-type cavity is based on the result of a finite elements simulation (CST Microwave Studio) allowing to predict its transmission parameters. It turns out that both the coupling to the external feed lines and the cavity resonance frequency can be tuned by changing the penetration depth of the pins of the coaxial connectors used for coupling the microwave signal in and out. However, it would be preferable to independently tune the cavity resonance by, e.g., inserting a screw into the cavity. In this case, the coupling to the feed lines could be kept constant.

In Fig. 2, we present the transmission spectrum measured for a superconducting box cavity at millikelvin temperatures. This cavity is milled into a massive block of an aluminum alloy ($88\% - 93\%$ aluminum content). Fitting the measured transmission spectrum to a Lorentzian, a loaded quality factor of $Q \simeq 3.4 \times 10^5$) in the high power regime is determined. Furthermore, with a cavity made of high purity aluminum we find an internal quality factor of over 1.4×10^6 at low microwave power (single photon level) and a temperature of 60 mK. Our experiments also show that the quality factor is less dependent on the input power compared with planar resonator geometries. This confirms our expectation that TLS play a less pronounced role in a 3D microwave cavity. The reason is that the mode volume of the 3D cavity is much larger than for a quasi 1D coplanar waveguide cavity, resulting in a reduced electric field strength and, in turn, reduced coupling to the TLS.

[1]We acknowledge financial support by the German Research Foundation through SFB 631, the German Excellence Initiative through the Nanosystems Initiative Munich (NIM), and the EU projects CCQED and PROMISCE.

We choose the design of the qubit to be integrated into the 3D cavity according to Ref. [3]. Specifically, transmon type qubits are used for this task because they can be fabricated with high yield and good reproducibility. Moreover, they show low sensitivity to $1/f$ noise. To maintain high coupling strength between the cavity and the qubit, the transmon qubit is placed in the antinode of the first electrical field mode.

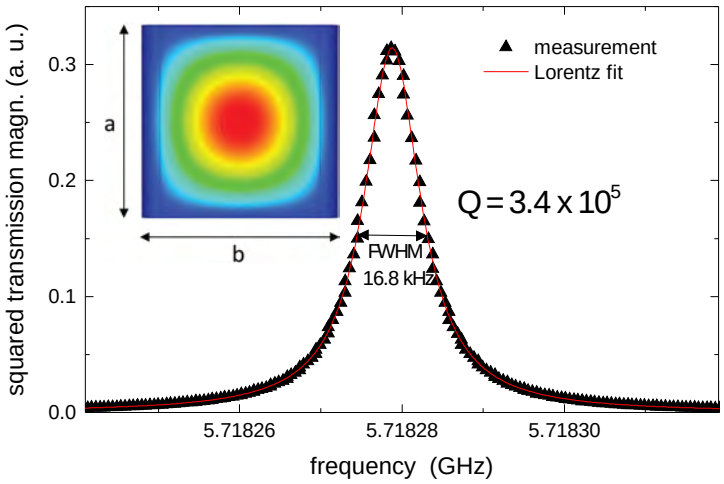

Figure 2: Fundamental mode of a superconducting aluminum cavity at 60 mK and −65 dBm input power. Loaded quality factor: $Q = 3.4 \times 10^5$. Inset: Simulated electric field distribution of the fundamental mode in arbitrary units.

As the next step, we plan to experimentally characterize a transmon qubit inside a fixed frequency cavity in both the time and frequency domain. Moreover, a setup with a tunable cavity and a tunable transmon qubit is planned. We also plan to extend the system to two cavities and multiple coupled transmon qubits.

References

[1] T. Niemczyk, F. Deppe, H. Huebl, E. P. Menzel, F. Hocke, M. J. Schwarz, J. J. Garcia-Ripoll, D. Zueco, T. Hümmer, E. Solano, A. Marx, and R. Gross, Nature Phys. **6**, 772–776 (2010).

[2] C. M. Quintana, A. Megrant, Z. Chen, A. Dunsworth, B. Chiaro, R. Barends, B. Campbell, Y. Chen, I.-C. Hoi, E. Jeffrey, J. Kelly, J. Y. Mutus, P. J. J. O'Malley, C. Neill, P. Roushan, D. Sank, A. Vainsencher, J. Wenner, T. C. White, A. N. Cleland, and J. M. Martinis, Appl. Phys. Lett. **105**, 062601 (2014).

[3] C. Rigetti, J. M. Gambetta, S. Poletto, B. L. T. Plourde, J. M. Chow, A. D. Córcoles, J. A. Smolin, S. T. Merkel, J. R. Rozen, G. A. Keefe, M. B. Rothwell, M. B. Ketchen, and M. Steffen, Phys. Rev. B **86**, 100506 (2012).

Characterization of Josephson parametric amplifiers

K. G. Fedorov, L. Zhong, M. Betzenbichler, S. Pogorzalek, A. Baust, P. Eder, J. Goetz, M. Haeberlein, F. Wulschner, E. Xie, E. P. Menzel, F. Deppe, A. Marx, R. Gross[1]

One of the cornerstones of quantum communication is the paradigm of quantum teleportation which allows one to safely transmit an unknown quantum state. Remote state preparation (RSP) has the same goal with the exception that a sender knows what state is to be remotely prepared. We plan to implement experiments with entangled quantum microwaves towards remote state preparation and teleportation. These states are typically generated by Josephson parametric amplifiers (JPAs) implemented by superconducting circuit technology [1–3]. Josephson parametric amplifiers (JPAs) [4] are nonlinear microwave devices capable of quantum-limited amplification in the microwave regime. They already have been successfully used for the realization of squeezed states [5, 6]. It is important to comprehensively characterize JPAs for the quantum communication protocols. Here, we report on recent measurements of a fresh batch of JPAs intended for future RSP experiments.

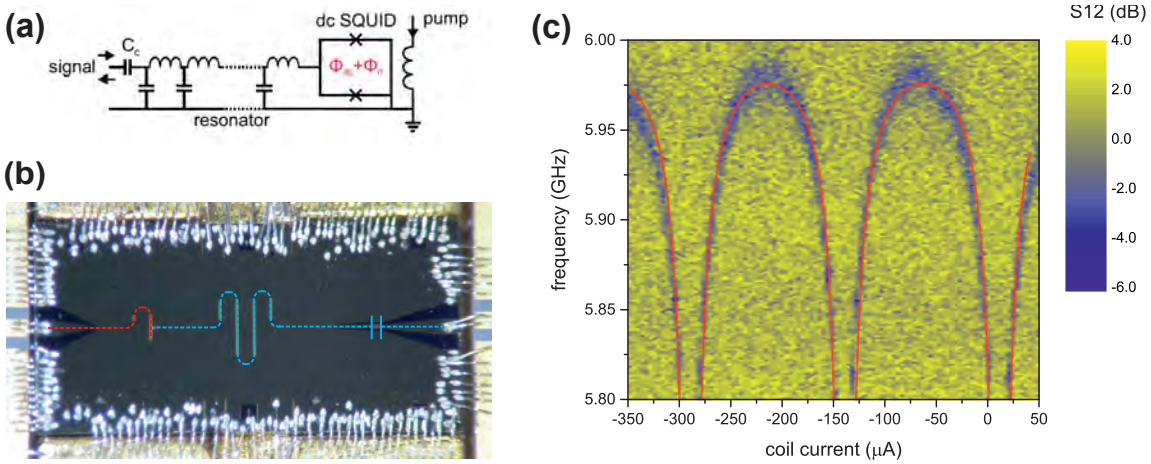

Figure 1: (a) Equivalent circuit of a JPA consisting of a quarter-wave length resonator shunted with a dc-SQUID to ground. An additional coplanar line is weakly coupled to the dc-SQUID in order to pump the JPA. (b) Photograph of the bonded JPA sample in a sample holder. Red and blue lines are guides for eye and highlight the pump line and the quarter-wavelength resonator, respectively. The 2.5 µm × 4 µm dc-SQUID (not visible) is located near the conjunction of the red and the blue lines. (c) Dependence of the JPA resonant frequency on the applied magnetic flux generated by an external coil. The red line depicts a fit to the experimental data.

In this report we show experimental results on one of the studied JPAs with a designed external quality factor $Q = 200$. A schematic and a photograph of the JPA chip are shown in Figs. 1(a) and (b). The dependence of the JPA resonant frequency on the magnetic flux through the dc-SQUID is shown in Fig. 1(c). This dependence can be described using a theory approach from Ref. [7]

$$\frac{2f}{\pi f_0}\tan\left(\frac{2f}{\pi f_0}\right) = \frac{L_{\text{cavity}}}{L_{\text{SQUID}}+L_{\text{loop}}}, \tag{1}$$

where L_{cavity} is the cavity inductance, L_{SQUID} is the SQUID inductance tunable by the magnetic flux, L_{loop} is the fixed inductance (geometrical and kinetic) of the SQUID loop, and f_0 is the cavity resonant frequency at zero magnetic field. The SQUID inductance can be defined as $L_{\text{SQUID}} = \Phi_0/4\pi I_c(\Phi)$, where $I_c(\Phi) = I_c|\cos(\Phi/\Phi_0)|$ is the flux dependent SQUID critical Josephson current, Φ is the magnetic flux bias, and Φ_0 the flux quantum. Using Eq. (1)

[1]We acknowledge financial support by the German Research Foundation through SFB 631, the German Excellence Initiative through the Nanosystems Initiative Munich (NIM), and the EU projects CCQED and PROMISCE.

and standard fitting routines one can fit the experimental dependence of the JPA resonant frequency on the magnetic flux bias $f(\Phi)$ (see Fig. 1(c)). The obtained fit parameters are: $L_{\text{cavity}} = 2.43\,\text{nH}$, $L_{\text{loop}} = 19.7\,\text{pH}$, $I_c = 7.65\,\mu\text{A}$. In addition, we have estimated experimental values for the external and internal losses of the JPA. Corresponding quality factors are $Q_{\text{ext}} = 280$ and $Q_{\text{int}} = 1500$. While the external quality factor is in a good agreement with the design value, the internal one deviates significantly from the design value of $Q_{\text{int}} \sim 10\,000$. This discrepancy may be due to problems in the fabrication process of the Josephson junctions of the dc-SQUID.

Next we characterize the non-degenerate gain of our JPA for a fixed input power which corresponds, on average, to 1 signal photon in the resonator. To this end we applied the pump microwave tone at a fixed frequency $f_{\text{pump}} = 2f_{\text{signal}} - 10\,\text{kHz}$, where f_{signal} is the signal frequency at the input of the JPA. Then, we swept the pump power in order to determine the condition for maximum non-degenerate gain. Experimental results are shown in Fig. 2. We observe a clear phase insensitive amplification of the input signal which reaches a maximum of 25 dB for pump powers $P_{\text{pump}} \sim 7.6\,\text{dBm}$.

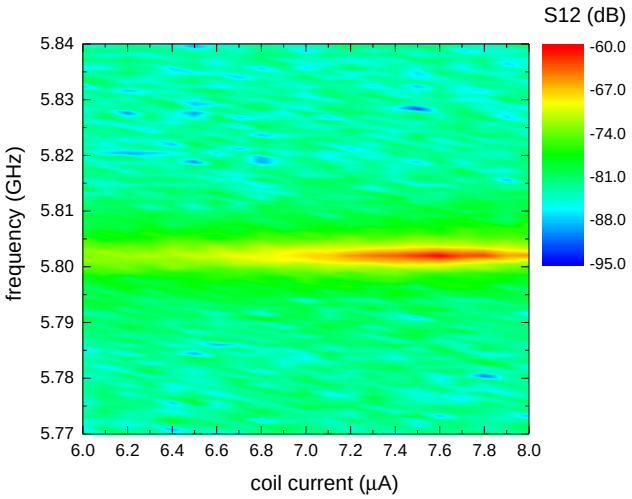

Figure 2: Non-degenerate gain of the JPA at a fixed flux-bias $I_{\text{coil current}} = -148\,\text{mA}$ versus pump power. Pump frequency is set to 11.604 GHz, the input signal power corresponds to around one photon in the resonator. The pump power level was measured at the output of the room temperature microwave source.

In conclusion, we have successfully tested new JPA samples. We have observed a regular dependence of the JPA resonant frequency on the applied magnetic field and extracted JPA parameters by fitting the experimental data with theory (1). The fit parameters were in a reasonable agreement with design values. We also measured the non-degenerate gain of the JPA and found its maximum value to be around 25 dB for a single photon input power. We intend to employ this JPA sample in more complex and novel experiments in quantum communication with continuous microwaves.

References

[1] B. Yurke, P. Kaminsky, R. Miller, E. Whittaker, A. Smith, A. Silver, and R. Simon, Phys. Rev. Lett. **60**, 764–767 (1988).

[2] S. Braunstein, and P. van Loock, Rev. Mod. Phys. **77**, 513–577 (2005).

[3] C. Eichler, D. Bozyigit, C. Lang, M. Baur, L. Steffen, J. Fink, S. Filipp, and A. Wallraff, Phys. Rev. Lett. **107**, 113601 (2011).

[4] T. Yamamoto, K. Inomata, M. Watanabe, K. Matsuba, T. Miyazaki, W. D. Oliver, Y. Nakamura, and J. S. Tsai, Appl. Phys. Lett. **93**, 042510 (2008).

[5] E. Menzel, R. Di Candia, F. Deppe, P. Eder, L. Zhong, M. Ihmig, M. Haeberlein, A. Baust, E. Hoffmann, D. Ballester, K. Inomata, T. Yamamoto, Y. Nakamura, E. Solano, A. Marx, and R. Gross, Phys. Rev. Lett. **109**, 250502 (2012).

[6] L. Zhong, E. P. Menzel, R. D. Candia, P. Eder, M. Ihmig, A. Baust, M. Haeberlein, E. Hoffmann, K. Inomata, T. Yamamoto, Y. Nakamura, E. Solano, F. Deppe, A. Marx, and R. Gross, New Journal of Physics **15**, 125013 (2013).

[7] M. Wallquist, V. Shumeiko, and G. Wendin, Phys. Rev. B **74**, 224506 (2006).

Characterization of superconducting transmission line resonators

J. Goetz, P. Summer, S. Meier, M. Krawczyk, M. Haeberlein, A. Baust, F. Wulschner, F. Deppe, A. Marx, R. Gross[1]

Superconducting transmission line resonators are widely used in circuit quantum electrodynamics experiments as quantum bus or storage devices. For these applications, long coherence times, which are related to the internal quality factor of the resonators, are essential [1]. Here, we show a systematic study of the internal quality factor of niobium thin film resonators at millikelvin temperatures.

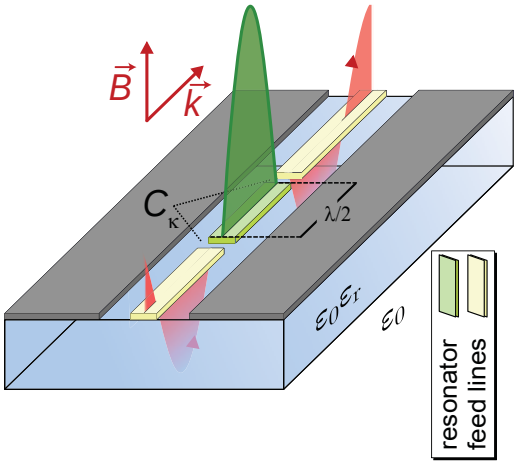

Figure 1: Sketch of a $\lambda/2$ resonator realized by inserting two coupling capacitors C_κ into a coplanar transmission line (yellow) on a dielectric substrate (blue) with permittivity ε_r. Red sinusoidal curve: Electromagnetic wave with wave vector **k** traveling along the transmission line. Due to the coupling capacitors a fundamental standing wave mode is excited (green curve).

All devices discussed here are fabricated from 100 nm thick niobium films sputter-deposited either onto silicon or sapphire substrates. Starting from our standard process of niobium on a 250 µm thick silicon substrate covered with 50 nm of SiO_2 on both sides, we investigate various materials and surface treatments to improve the quality factor of the resonators [2]. These treatments are crucial as the main loss channels in coplanar waveguide (CPW) resonators at low power are dielectric losses due to two level fluctuators at the metal-dielectric (Nb/SiO_2) and the dielectric-dielectric interfaces. All resonators discussed here are of the $\lambda/2$ type as sketched in Fig. 1 and have resonance frequencies between 4 GHz and 6 GHz. In order to be able to compare devices with different resonance frequencies ω_r, we calculate the internal quality factor $Q_i = (Q_l^{-1} - Q_x^{-1})^{-1}$. Here, Q_l and Q_x are the loaded and external quality factor, respectively. We obtain the loaded quality factor by performing spectroscopy measurements on each device and fitting the measured transmission curves to Lorentzian spectra. The external quality factor Q_x is determined from microwave simulations. We find that the internal quality factor itself is well described by the empirical relation $Q_i = (Q_{const}^{-1} + \widetilde{Q}_{TLS}^{-1}(P_{cir}, T))^{-1}$, where the power and temperature dependent contribution

$$\widetilde{Q}_{TLS}(P_{cir}, T) = Q_{TLS} \frac{\sqrt{1 + (P_{cir}/P_c)^\beta}}{\tanh(\hbar\omega_r / 2k_B T)} \quad (1)$$

is arising from an ensemble of microscopic two level systems (TLS) located inside the dielectric or just at the interface between the dielectric and the superconducting Nb thin film [3]. The constant term Q_{const} accounts for all other loss mechanisms. In Eq. (1), $P_{cir} = PQ^2/\pi Q_x$ is the power circulating inside the resonator when applying the power P to the resonator input, P_c is a critical power and the exponent β is expected to be about unity.

In Figs. 2(a) and 2(b) we show the two contributions Q_{TLS} and Q_{const} for different samples measured at millikelvin temperatures. Samples 1, 2, 3, and 6 are CPW structures fabricated

[1]We acknowledge financial support by the German Research Foundation through SFB 631, the German Excellence Initiative through the Nanosystems Initiative Munich (NIM), and the EU projects CCQED and PROMISCE.

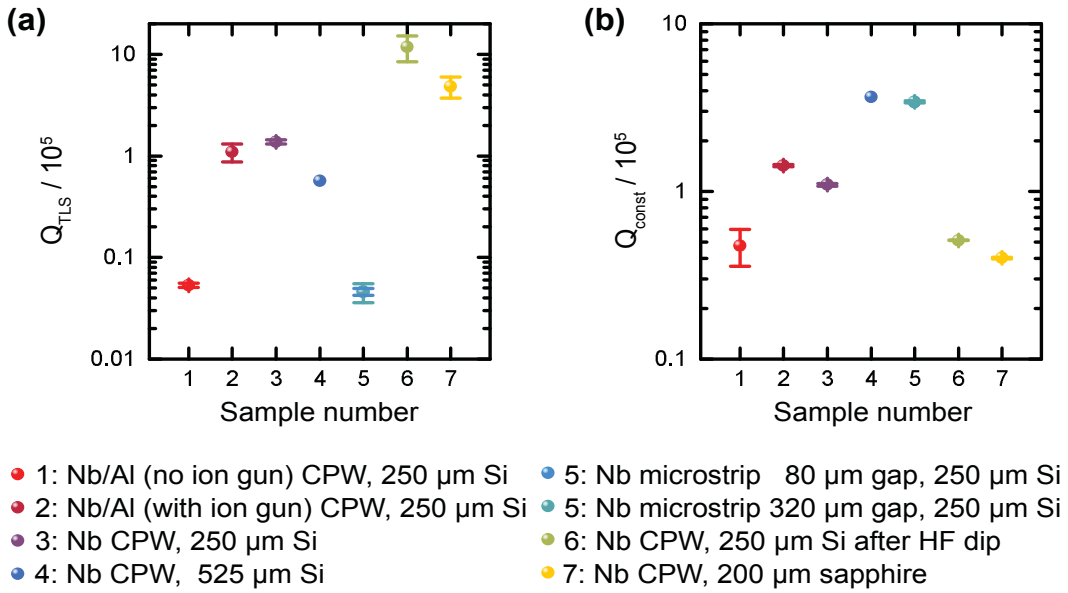

Figure 2: (a) Two-level system (TLS) contribution to the internal quality factor for various materials, treatments, and geometries. The data is taken at around 25 mK and low microwave power corresponding to about a single photon on average in the resonator. (b) Remaining constant contribution to the internal quality factor for various materials, treatments, and geometries.

on a 250 µm thick silicon substrate covered with 50 nm of SiO_2 on both sides which is removed for sample 6 using an HF dip. Samples 1 and 2 include a niobium-aluminum interface which is required for galvanically coupled flux qubits made from aluminum. For sample 2, the niobium surface is cleaned using an Ar ion beam cleaning process before evaporating aluminum in-situ onto the niobium film. Samples 4 and 7 are identical to sample 3 but fabricated on a 525 µm thick silicon substrate and a 200 µm thick sapphire substrate [4], respectively. We also show results for two samples fabricated in a microstrip design (5) which are discussed in detail in Ref. [5].

As shown in Fig. 2(a), we can achieve quality factors Q_{TLS} limited only by TLS as high as 10^6 by applying a proper surface treatment of the substrates. Unfortunately, then the remaining constant term Q_{const} limits the total internal quality factors to values below 10^5. Nevertheless, these quality factors are already suitable for most circuit QED experiments. It is interesting to emphasize a few more details on the investigated material systems. We first note that Nb resonators containing a short Al segment at a current node require a careful removal of the Nb oxide, for example by an Ar ion gun cleaning step, before evaporating in-situ the aluminum. This result is important for the implementation of galvanically coupled flux qubits into Nb transmission line resonators as discussed in the contribution on page 21. Second, removing the SiO_2 coating from the Si substrates immediately reduces the TLS losses significantly. The same effect is observed when we replace the silicon substrate with sapphire, which has an intrinsically "cleaner" surface with a smaller density of TLS. And finally, we note that for coplanar waveguide resonators thin substrates limit Q_i via the Q_{const}-contribution regardless of the chosen substrate or surface treatment. We attribute this behavior to possible ohmic losses, either in the silver glue used to fix the chip to the gold-plated copper sample holder or in the sample holder itself. A notable exception is the microstrip geometry, which has a superconducting ground plane at the back side of the substrate chip.

In conclusion, we improved the quality factors of the planar microwave resonators fabricated at WMI to an extent, where we are limited by the coherence of other quantum circuits, in particular, the flux qubit, even at millikelvin temperatures, and ultra low powers.

References

[1] M. Mariantoni, H. Wang, R. C. Bialczak, M. Lenander, E. Lucero, M. Neeley, A. D. O'Connell, D. Sank, M. Weides, J. Wenner, T. Yamamoto, Y. Yin, J. Zhao, J. M. Martinis, and A. N. Cleland, Nature Phys. **7**, 287–293 (2011).
[2] P. Summer. *Characterization of superconducting coplanar waveguide resonators at millikelvin temperatures*. Diploma thesis, Technische Universität München (2014).
[3] J. M. Sage, V. Bolkhovsky, W. D. Oliver, B. Turek, and P. B. Welander, J. Appl. Phys. **109**, 063915 (2011).
[4] S. Meier. *Loss reduction of superconducting coplanar microwave resonators on sapphire substrates*. Bachelor's thesis, Technische Universität München (2014).
[5] A. Baust, M. Krawczyk, M. Haeberlein, E. Hoffmann, U. Ehmann, N. Kalb, F. Deppe, A. Marx, and R. Gross, WMI Ann. Rep. **2011**, 59–61 (2011).

Materials, Thin Film and Nanotechnology, Experimental Techniques

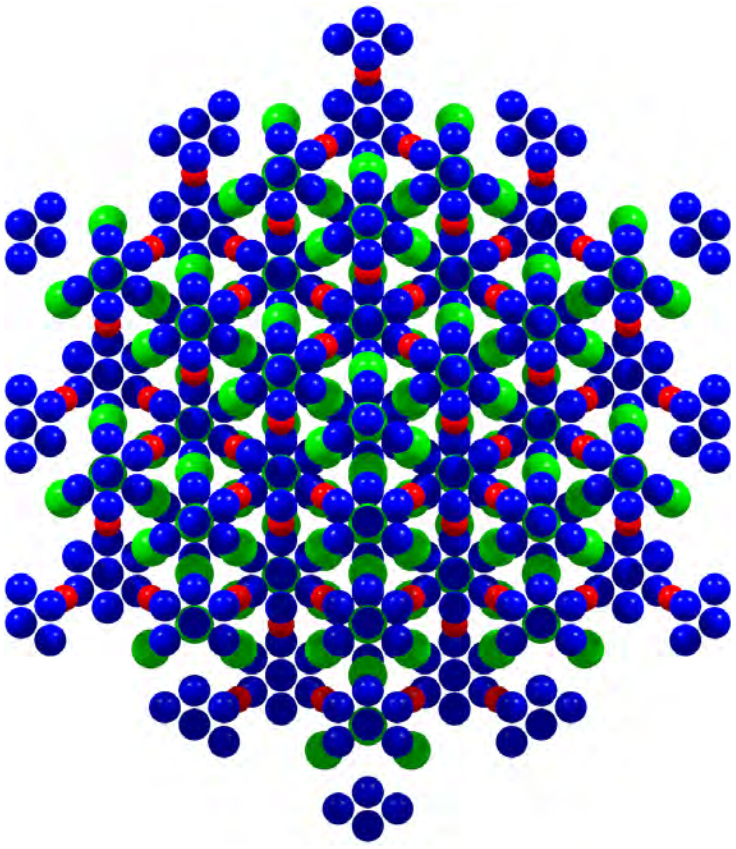

The *A*-227 pyrochlore structure of $Nd_2Ir_2O_7$. View along the (111) direction (red: Nd^{3+}, green: Ir^{4+}, blue: O^{2-}).

Magnetic properties of the electron doped cuprate superconductor $Nd_{2-x}Ce_xCuO_4$

A. Dorantes, Q. Cai, M. V. Kartsovnik, A. Erb[1]

The 214 superconducting (SC) cuprate compounds contain CuO_2 layers within their structure and have the general formula $Ln_{2-x}A_xCuO_4$ where Ln is a rare earth metal and A = Ca, Sr, Ba, Ce etc. Depending on their chemical composition they are divided into hole and electron-doped cuprates. They are derived from a parent compound which is an antiferromagnetic (AF) Mott insulator. Upon doping, charge carriers are inserted and the AF state disappears when the carrier concentration n is large enough to produce a SC transition. The transition temperature T_c reaches a maximum value at the optimal dopant concentration x_{opt}. After this, the T_c decreases again until the SC state disappears [1].

Most of the current information about the properties of these materials is focused on the hole-doped cuprates while the electron-doped cuprates have not been studied as intensively, mainly due to difficulties in their preparation. In the electron-doped cuprates the AF and SC states are not separated by a well defined boundary and it is not fully understood whether superconductivity and antiferromagnetism coexist or a structural or electronic phase separation occurs. In addition, samples of the electron-doped cuprates do not show a SC transition in their as grown state and have to be subjected to an annealing process which eliminates the oxygen surplus in the chemical formula $Ln_{2-x}A_xCuO_{4+\delta}$ where δ is the apical oxygen in the crystal structure T' [2].

In the electron-doped cuprate $Nd_{2-x}Ce_xCuO_4$ (NCCO), a SC transition has been reported between $x = 0.13$ and $x = 0.18$ with a critical temperature $T_{c,opt} = 25\,K$ at $x_{opt} = 14.5$ [1]. In previous research at the Walther-Meißner Institute [3] NCCO showed quantum oscillations of magnetoresistance (Shubnikov-de Haas, SdH effect) where the SdH effect was observed on the optimally doped and a range of overdoped compositions of NCCO, but no oscillations were found in underdoped samples. The SdH oscillations vanished within a very small doping interval in x which suggested a sharp change in the electronic structure when the charge carrier concentration deviates from x_{opt}. This observation and the uncertainty of the separation of the AF and SC states motivated further studies on the NCCO superconductor with particular focus on the underdoped regime of the phase diagram.

Underdoped single crystals with 10, 11, 12, 12.5, and 13 % Ce concentration were grown with the Traveling Solvent Floating Zone Technique [2]. Optimally doped samples $x = 14.5$ and $x = 15$ % were grown for comparison. The samples with 10, 11, 12, and 12.5 % were repeatedly annealed at 910 °C for 20 h for each repetition and the samples with 13, 14.5, and 15 % were annealed at 935 °C. The magnetization χ was measured in AC and DC fields in zero field cooling (ZFC) and (FC) with a $B_{\parallel} = 100\ Oe$. The SC volume fraction was estimated by comparing to a type-I superconducting sample with same size and shape as the NCCO crystals, in this case Pb. An overview of the corresponding results can be seen in Fig. 1.

As expected, NCCO-14.5 and NCCO-15 showed a sharp SC transition at $T_{c,opt} = 23\,K$ in AC and $T_{c,opt} = 20\,K$ in DC. Both crystals showed a SC volume fraction of 100%. The NCCO-13 samples showed a maximum $T_c = 16.5\,K$ in AC and $T_c = 10\,K$ in DC with a SC volume fraction close to 100 %. The transition width was up to $\Delta T_c = 10\,K$. An interesting observation was that after 20 h of annealing the DC measurement showed no transition, even though a transition in AC was observed. Similarly, the NCCO-12 crystals showed maximum $T_c = 17\,K$ in AC and $T_c = 12\,K$ in DC and a SC volume fraction close to 100 %. To the best of our knowledge,

[1]This work is supported by the German Research Foundation (Grant-No. GR 1132/15-1). QC acknowledges support via the State Scholarship Fund by China Scholarship Council, 201306250060.

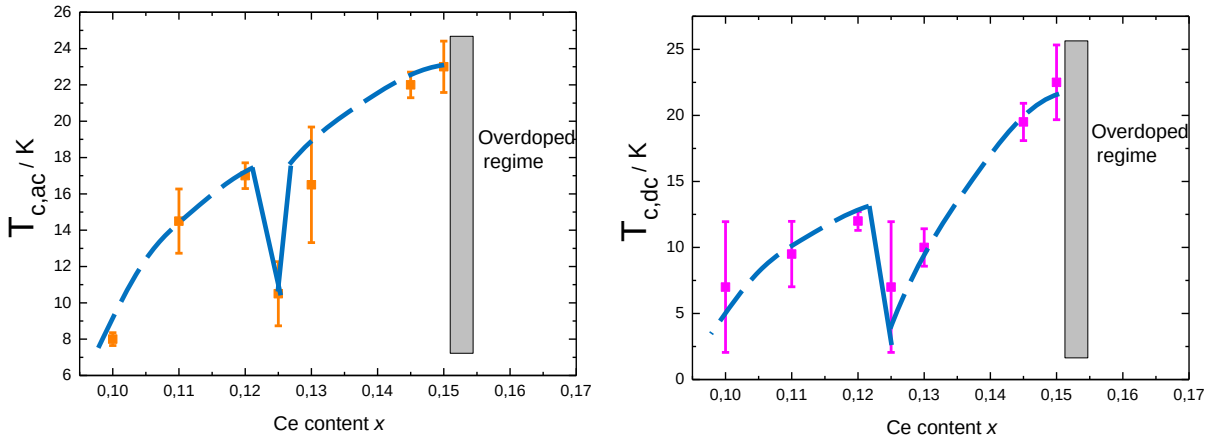

Figure 1: Superconducting half dome of the NCCO samples in AC (left) and DC (right). The dotted lines are guided to the eye. The vertical bars show the deviation in the values to the minimum T_c observed for each sample. The T_c should decrease with lower Ce concentration x, but the T_c seems to drop at $x = 12.5$ and it reappears again at $x = 12$.

a SC transition in a 12 % Ce doped crystal has not been reported before. Additionally and, very unexpectedly, the T_c was higher than T_c of NCCO-13. The T_c should decrease with lower x until the AF order becomes dominant and suppresses superconductivity. To clarify this issue, crystals of the NCCO-12.5 were also prepared and measured. The NCCO-12.5 samples showed a broad SC transition in AC. In contrast, the DC transition for ZFC was almost negligible or not even present at all. In the FC measurements only a paramagnetic contribution was observed. NCCO-10 and NCCO-11 showed a transition in AC measurements but only traces of superconductivity in DC, with $T_c = 5\,\mathrm{K}$ and $T_c = 7\,\mathrm{K}$ respectively. Furthermore, the SC volume fraction was very small with 1.3 % for ZFC experiments and a completely absent SC signal in FC curves. These results lead to the conclusion that for most of the tested samples we could achieve a SC transition after an appropriate annealing treatment, but the SC volume fraction drops when x is lower than 12 %. We note that the AC magnetization curves can be very misleading and they should not be considered as a measure of bulk superconductivity. Special attention should be paid to the results of the 12, 12.5, and 13 % samples. Our results showed bulk superconductivity at 13 % but no SC transition and SC volume fraction at $x = 12.5$ %, which reappeared at $x = 12$ %. In fact, our findings could be a first clue of the existence of the 1/8 anomaly in the electron-doped cuprates, analogous to that observed in the hole-doped cuprates. The latter has been explained with the formation of spin-charge stripes [4].

In order to confirm the presence of such properties in the electron-doped system, further site sensitive tests such as NMR, spin correlation studies, magnetization experiments and neutron scattering should be performed on carefully and well characterized high-quality crystals. For the susceptibility studies, more concentrations of Ce doping should be equally tested to complete the data in the underdoped region of NCCO.

References

[1] N. P. Armitage, P. Fournier, and R. L. Greene, Rev. Mod. Phys. **82**, 2421–2487 (2010).
[2] M. Lambacher, T. Helm, M. Kartsovnik, and A. Erb, Eur. Phys. J. Special Topics **18**, 61–72 (2010).
[3] M. V. Kartsovnik, T. Helm, C. Putzke, F. Wolff-Fabris, I. Sheikin, S. Lepault, C. Proust, D. Vignolles, N. Bittner, W. Biberacher, A. Erb, J. Wosnitza, and R. Gross, New J. Phys. **13**, 015001 (2011).
[4] J. M. Tranquada, B. J. Sternlieb, J. D. Axe, Y. Nakamura, and S. Uchida, Nature **375**, 561–563 (1995).

News from our methuselah cryogen-free fridge

K. Uhlig

Improved 1K-stage

In 2014, after 13 years of reliable operation, the cold head of our pulse tube cryocooler (PTC) had developed a cold leak and had to be replaced by a new one (courtesy of Cryomech, Inc. [1]). We decided to stick with a small (0.5 W @ 4 K) cold head because of its low vibration level and low power consumption.

The present version of our cryogen-free dilution refrigerator (DR) is equipped with a ^{4}He-1K cooling loop whose cooling power at $T \sim 1$ K exceeds that of the still of the DR by approximately a factor of 10 (Fig. 1) [2, 3]. High refrigeration powers at $T \sim 1$ K are needed in experiments where cold amplifiers have to be cooled. The construction of the 1K-stage is identical to the one of a JT-cooler. It consists of a counterflow heat exchanger (cf-hx), a flow restriction and a vessel, where the liquid ^{4}He can accumulate after expansion. The gas fraction of the flow is pumped by a standard rotary pump. In the vessel there is a heat exchanger which is part of the DR loop so that the ^{3,4}He mash of the DR is liquefied there. This leads to a much improved condensation rate at the beginning of an experiment. The 1K-loop can be shut down with the DR still in operation by pumping the ^{4}He into a storage tank. Then the temperature of the 1K-vessel quickly approaches the temperature of the 2nd stage of the PTC and the DR is run like a standard dry DR.

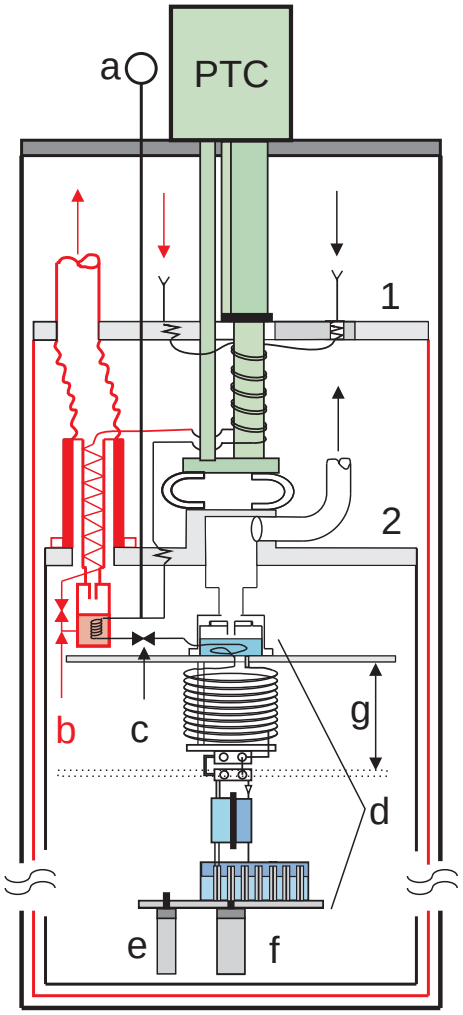

Figure 1: Sketch of our dilution refrigerator (DR). It consists of three components, the PTC, a dilution unit and a ^{4}He-1K-loop. The 1K-loop is drawn in red. 1, 2: 1st and 2nd stage of PTC; a: pressure gauge and line; b, c: flow restrictions; d: dilution unit; e: CMN thermometer; f: superconducting fixed point device; g: still flange before and after installation of the new 1K-stage.

Whereas in the former setup the long cf-hx took up quite a bit of the length of the experimental space, in the modified version the cf-hx is placed in an extension of the mounting plate of the 2nd stage of the PTC. This way the otherwise empty space between the two stages of the PTC is used and valuable experimental space in the inner vacuum can is saved ("g" in Fig. 1).

In Fig. 2 the refrigeration power of the 1K-loop is depicted. The cooling power is proportional to the ^{4}He flow rate and therefore primarily given by the pumping speed of the rotary pump (66 m^3/h in our present setup). We reached a lowest temperature of 1.0 K and a maximum cooling power of 65 mW at a vessel temperature of 1.4 K. The base temperature of the DR was 4.5 mK.

Flow restriction of the DR

The ^{3}He flow of our DR is liquefied in the 1K-pot and then expanded in a flow restriction ("c" in Fig. 1). It is made from a piece of capillary where a wire is inserted to give just the right flow impedance needed. The dimensions of capillary and wire are most critical to give precisely the right value of the flow impedance. Of course, the pressure at the inlet of the flow restriction depends on the ^{3}He throughput. The pressure at the outlet is small, but high enough to keep the ^{3}He in the liquid phase. In Fig. 3 the ^{3}He inlet pressure p_{in} of the impedance is given as a function of the flow rate. To measure p_{in} precisely, a separate pressure line has been installed in the DR with a pressure gauge at the top of the cryostat (marked "a" in Fig. 1). For comparison, calculated pressure curves are included in the graph, one for turbulent flow and one for laminar flow.

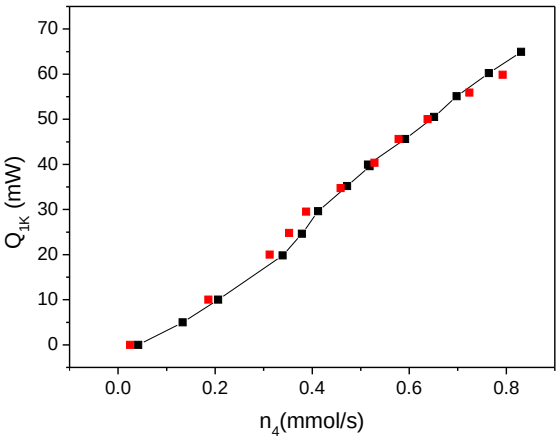

Figure 2: Cooling power of the 1K loop of Fig. 1 as a function of the ^{4}He throughput. Data of two different experiments are plotted. The maximum refrigeration power was 65 mW.

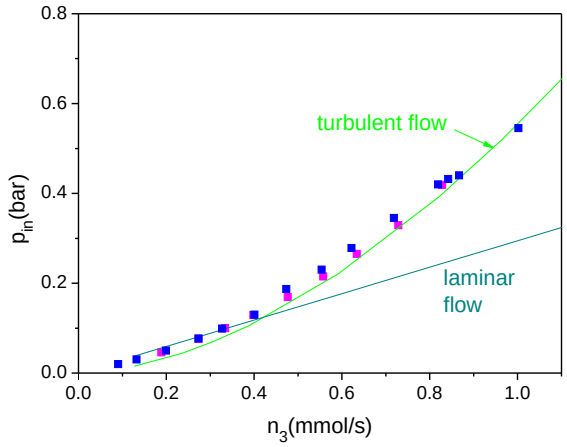

Figure 3: ^{3}He inlet pressure measured at the inlet of the flow restriction. Experimental data of two experiments are given. For comparison, calculated curves are shown for laminar and turbulent ^{3}He flow.

The expression for calculating the pressure drop ΔP is given by [4]

$$p_{\mathrm{in}} \approx \Delta P = 0.5 \cdot \Psi \cdot L \cdot G^2 / D_h \cdot \rho \qquad (1)$$

where $\Psi = 64/Re$ and $Re = GD_h/\eta$ for Poiseuille (laminar) flow or $\Psi = 0.316(Re)^{-0.25}$ for turbulent flow (Re = Reynolds number). L is the length of the tube, G the mass flow rate, D_h the hydrodynamic diameter, η the viscosity and ρ the density. To calculate p_{in}, it has to be kept in mind that the temperature of the liquid ^{3}He flow changes in the capillary while the pressure drops, and ρ and η also change (only the enthalpy remains constant). Fortunately, as the ^{3}He stream is in an all-liquid state, these changes are small ($\delta\eta/\eta \approx 10\%$ and $\delta\rho/\rho \approx 5\%$). We used constant values for η and ρ in the calculus. From Fig. 3 it is obvious that the ^{3}He flow in the restriction of a dry DR is turbulent, and finally we understand the disproportionately high increase of the ^{3}He inlet pressure with increasing flow rate which is usually encountered on operation of a dry fridge.

In future, we would like to take similar data from the impedance of the 1K-circuit ("b" in Fig. 1) to get a comparison between the ^{3}He flow in the dilution loop and the ^{4}He flow in the 1K-stage.

References

[1] Cryomech Inc., Syracuse, NY .
[2] K. Uhlig, Cryogenics [in press] (2014).
[3] K. Uhlig, AIP Conf. Proc. **1573**, 1393–1398 (2014).
[4] G. White. *Experimental Techniques in Low-temperature Physics, 3rd edition* (Clarendon Press, Oxford, 1979).

Electron beam lithography system nB5

J. Goetz, M. Haeberlein, M. Pernpeintner, L. Wang, F. Wulschner, E. Xie, T. Brenninger, E. P. Menzel, F. Deppe, A. Marx, R. Gross[1]

Supported by substantial funding of the Excellence Cluster Nanosystems Initiative Munich (NIM) the Walther-Meißner-Institute could replace its electron beam writer. The new 100 kV nB5 Electron Beam Lithography System of NanoBeam Ltd., UK, has been delivered in October 2014. With this new powerful instrument the WMI has strengthened its technological infrastructure for nanofabrication.

Solid state nanostructures are at the core of numerous research projects at WMI including superconducting quantum circuits, nano-electromechanical devices and ferromagnetic nanostructures. Our previous electron beam lithography system based on a FEI electron beam microscope XL30 SFEG and a Raith elphy plus lithography unit served as central facility to define lateral nanostructures at the WMI for almost 15 years (actually the system had been in use at the University of Cologne for 3 years before moving the machine to WMI). However, in the last years both the demand for writing time and the technological requirements (structure size, write field size, write field alignment, writing speed, throughput, reliability) have strongly increased because of the growing number of research projects based on the availability of respective nanostructures. Therefore, the replacement of the old electron beam writer by a state-of-the-art electron beam lithography systems was overdue.

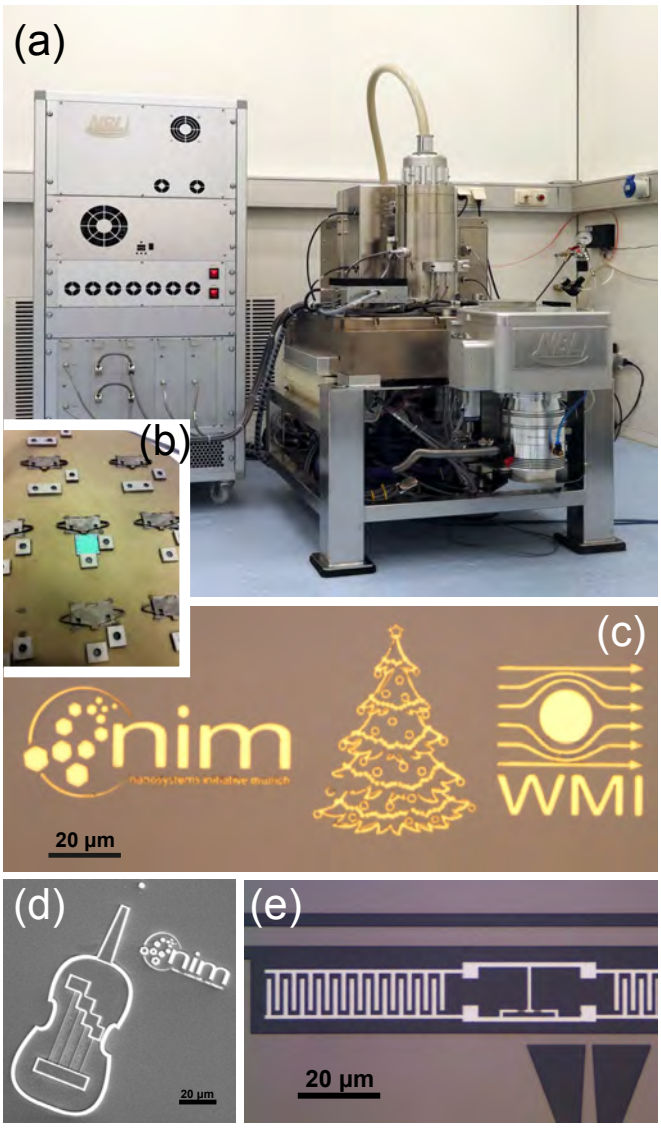

Figure 1: Photograph of the nB5 electron beam lithography system and micrographs of some test structures.

The nB5 system has been installed in the place of the old lithography system inside the WMI clean room facility in October 2014. On the occasion of this replacement, all final air filters in the clean room ceiling have been renewed. The nB5 main characteristics are an innovative design of the electron optics and a high degree of automation providing high throughput and reliability. The nB5 is equipped with a thermal field emitter, fast deflection speed (55 MHz deflection rate), fast beam blanking unit (rise time < 5 ns, 55 MHz blanking rate), main field

[1]We acknowledge financial support by the German Excellence Initiative through the Nanosystems Initiative Munich (NIM).

and subfield writing, and advanced vibration tracking design. The electron optics provides beam voltages up to 100 kV, beam currents up to 100 nA (presently $\sim$ 10 nA), and a theoretical beam size of 2.3 nm. After 3 days of installation and adjustments there was an initial user training for several days.

Figure 1(a) shows a photograph of the nB5 system in the WMI clean room. The device is equipped with a load-lock chamber with automatic loading robotics. The loading cassette can house up to 6 chucks with a diameter of 8 inch. Figure 1(b) shows a part of a chuck with a mounted 12 mm $\times$ 12 mm silicon wafer. The nB5 system operation is highly automated. The sample geometry is converted from the GDSII format into the required data format by the pattern generation software. After defining the job in a dedicated scripting language, the sample alignment, beam focusing/adjustment, mark recognition, write field alignment/stitching, and electron beam exposure can be run in a fully automated fashion.

Figure 1(c) shows a micrograph of a thin film gold test structure fabricated in a lift-off process using a PMMA resist on a silicon wafer. Figure 1(d) depicts a micrograph of a nano-electromechanical device consisting of four doubly clamped, tensile-stressed Si_3N_4 nanobeams. The sample is fabricated on a single-crystalline silicon wafer coated with a thin layer of tensile-stressed low pressure chemical vapor deposited silicon nitride (Si_3N_4). First, a nanobeam as well as supporting clamping rectangles are defined using electron beam lithography. Subsequently, the unprotected Si_3N_4 is removed by reactive ion etching (RIE) step. Finally, the nanobeam is released in an additional isotropic RIE step. The micrograph in Fig. 1(e) shows a zoom into the center of a superconducting microwave coplanar transmission line. Implementing this structure, in a first step, the geometry of the thin film niobium resonator is defined by electron beam lithography and reactive ion etching. In a second step a superconducting transmon qubit (bright structure between the center conductor and the resonator groundplane) is fabricated by shadow evaporation. Here, the transmon geometry is defined in a second electron beam lithography step in a two-layer PMMA/MAA resist system followed by the deposition of thin aluminum layers and a lift-off process.

The initial experience with the new electron beam lithography system nB5 is very positive. The system is extremely versatile and fast. It can be operated remotely (except for sample mounting). The machine can be operated after very short training period and therefore is well suited for research groups with master and Ph.D. students. There are still some minor bugs in the pattern generating software but, nevertheless, the first samples look very promising.

Experimental Facilities

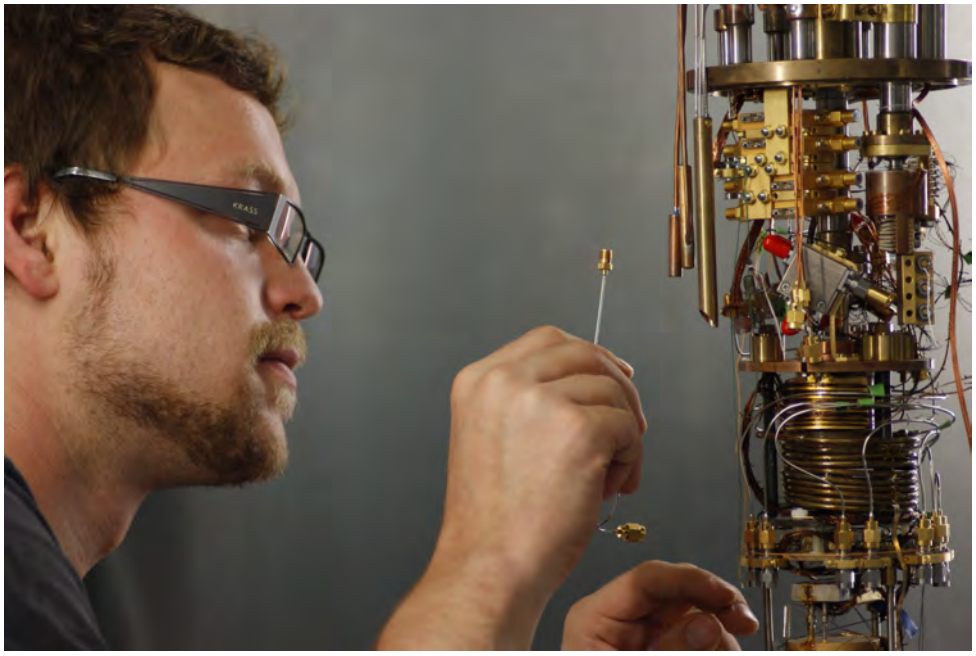

Overview of Key Experimental Facilities and Infrastructure

In the following basic information on the key experimental facilities and components of the technical infrastructure installed at the Walther-Meißner-Institute (WMI) is given.

UHV Laser-MBE

The WMI operates an UHV Laser-Molecular Beam Epitaxy (L-MBE) system for the growth of complex oxide heterostructures. The system has been designed to meet the special requirements of oxide epitaxy. The UHV cluster tool consists of the following main components:

- central transfer chamber;
- load-lock chamber with a heater system for substrate annealing;
- laser deposition chamber with a KrF excimer laser, *in-situ* reflection high energy electron diffraction (RHEED) system, laser substrate heating system, and atomic oxygen/nitrogen source; the RHEED system has been modified to allow for the operation at high oxygen partial pressure up to 0.5 mbar;
- surface characterization chamber with UHV scanning atomic force microscope (Omicron);
- metallization chamber with a four heart electron gun system and a liquid nitrogen cooled sample stage. The sample holder can be tilted for shadow evaporation.

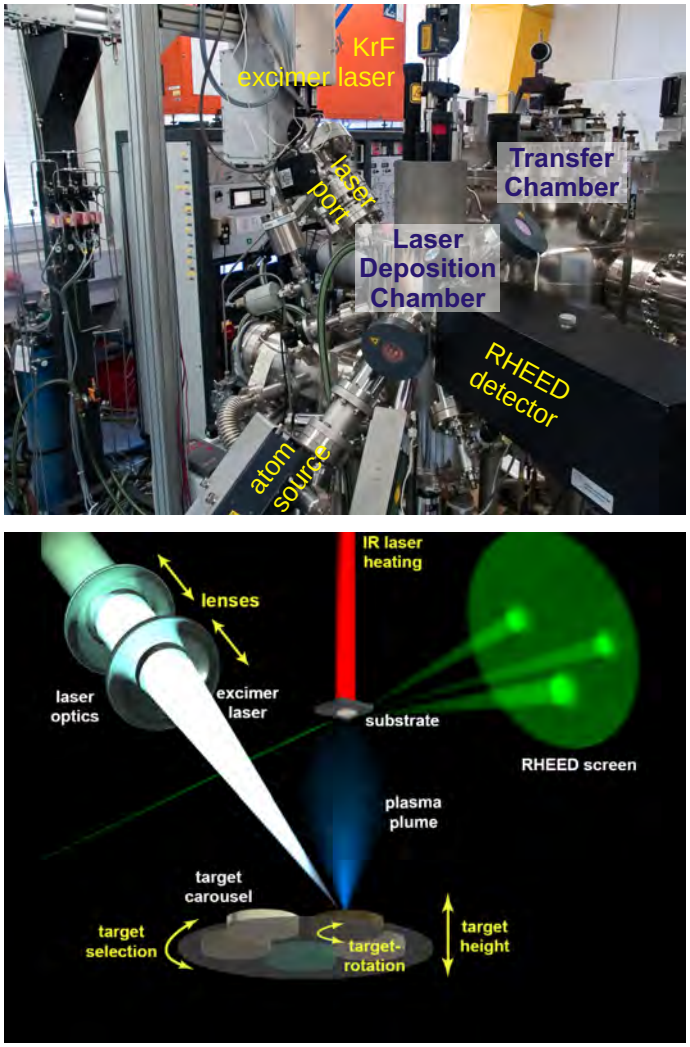

Figure 1: Top: UHV laser-molecular beam epitaxy system. Bottom: principle of the deposition process.

The system is used for the growth of complex oxide heterostructures consisting of superconducting, ferromagnetic, ferroelectric, and semiconducting materials such as high-temperature superconductors, doped manganites, (double) perovskites, magnetite, zinc oxide, rare earth iron garnets, pyrochlore iridates, etc.

The original laser molecular beam epitaxy system (laser-MBE) designed already in 1995/96 has been continuously upgraded and modified until now. In particular, the substrate heating system and the temperature control unit were changed from a resistive radiation heater to an infrared laser heating system (see Fig. 3, left) including a pyrometer for determining the sample temperature. In addition, a source for atomic oxygen and nitrogen has been installed. The main advantage of the new heating system is that only the substrate is heated while the surrounding parts are hardly affected (Fig. 3, right). In this way one can achieve a substantially better vacuum at temperatures well above 1000 °C. The achievable substrate temperature is limited by the melting point and the size of the substrate material (approx. 1410 °C for a 5 mm × 5 mm silicon substrate). The laser heating system has already been successfully used for removing the amorphous silicon oxide layer from the surface of silicon substrates at 1150 °C.

Figure 2: Pulsed Laser Deposition (PLD): When the pulse of the UV laser (KrF excimer laser, 248 nm) hits the target, the target material is ablated and the so-called laser "plume" containing highly excited atoms and molecules is formed.

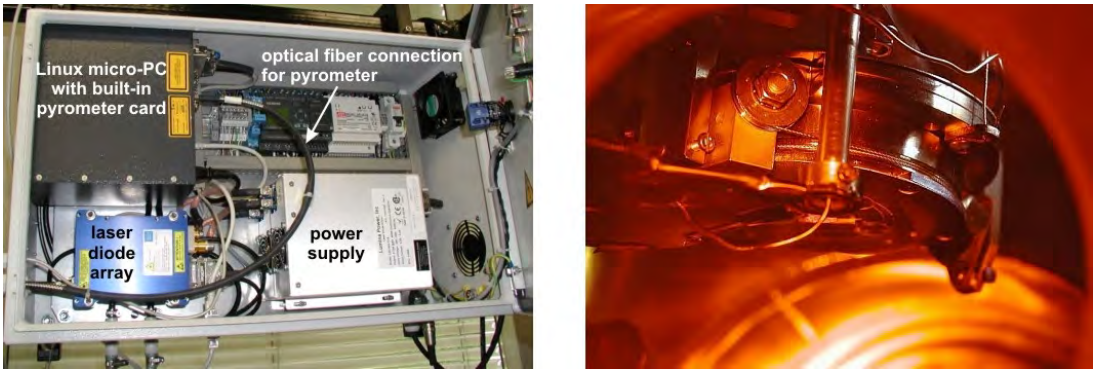

Figure 3: Components of the laser heating system: The substrate is heated using an IR diode laser head that is located in a separate box far away from the deposition chamber (left). The laser light is brought to the substrate (right) via an optical fiber.

We have further developed and installed a home-made telescope zoom optics for the pulsed UV laser light, consisting of in total five lenses on sliding lens holders allowing for a movement over a total distance of 1200 mm. The lens holders are attached to independent stepper motors, each connected to a controller providing an accurate positioning precision. The controllers are driven via a PC, thus allowing for a full automation of the lens system itself. With this telescope zoom optics we are able to change the area of the UV laser spot on the target, resulting in an accessible range of laser fluences from $\rho_L = 0.5\,J/cm^2$ to $5\,J/cm^2$. To maintain a stable laser fluence at the target, we have installed a so-called *intelligent* window (PVD Products) at the laser entrance port combining two unique features. First, it keeps the inner side of the entrance window free of coatings by blocking the ablated plasma plume via a rotatable disc consisting of UV grade fused silica. Second, an insertable mirror positioned in the light path after the disc allows to guide the incoming UV laser pulse through a side window, where its energy is determined by a pyroelectric detector. These measures help to improve the deposition processes by accurately monitoring ρ_L as one of the most critical process parameters.

UHV Electron Beam Evaporation System

The UHV metal MBE system allows for the growth of high quality metallic thin films by electron beam evaporation and molecular beam epitaxy. The system is optimized for the fabrication of superconducting persistent current qubits by aluminum shadow evaporation. It is equipped with an improved substrate holder allowing for multi-angle shadow evaporation. The main components of the system are:

- UHV system with a process chamber with a base pressure of $\sim 1 \times 10^{-8}$ mbar pumped by a 1000 l/s turbo molecular pump with magnetic suspension of the rotor adequate for corrosive gases.
- Load-lock chamber equipped with a magnetic transfer system (push-pull positioner) for sample transfer without breaking the vacuum in the process chamber.
- Downstream pressure control by an adaptive pressure controlled gate valve.
- Electron beam evaporator with six 8 cm^3 crucibles embedded in a linearly movable water cooled rail providing six different materials.
- Film thickness measurement and closed loop evaporation rate control by a quartz crystal microbalance in combination with the evaporation controller.
- Effusion cell for molecular beam epitaxy processes.
- Ion sputtering gun for in-situ sample cleaning
- Manipulator with UHV stepping motors for automated and precise sample tilt and options for rotating and cooling the sample.

A precise and reproducible tilt of the sample is realized by a sample manipulator with process specific degrees of freedom. The downstream pressure control allows for a fast adjustment and precise control of the oxygen partial pressure. This is crucial for a well-defined oxidation process of the Josephson junctions barriers. The entire process can be performed fully automated via a touch screen and is controlled by a LabView program. Up to six effusion cells can be optionally added to the system allowing for further materials. The manipulator allows for further degrees of freedom that can be used to align the sample to the effusion cells, the ion sputtering gun and to measuring equipment such as ellipsometry or RHEED.

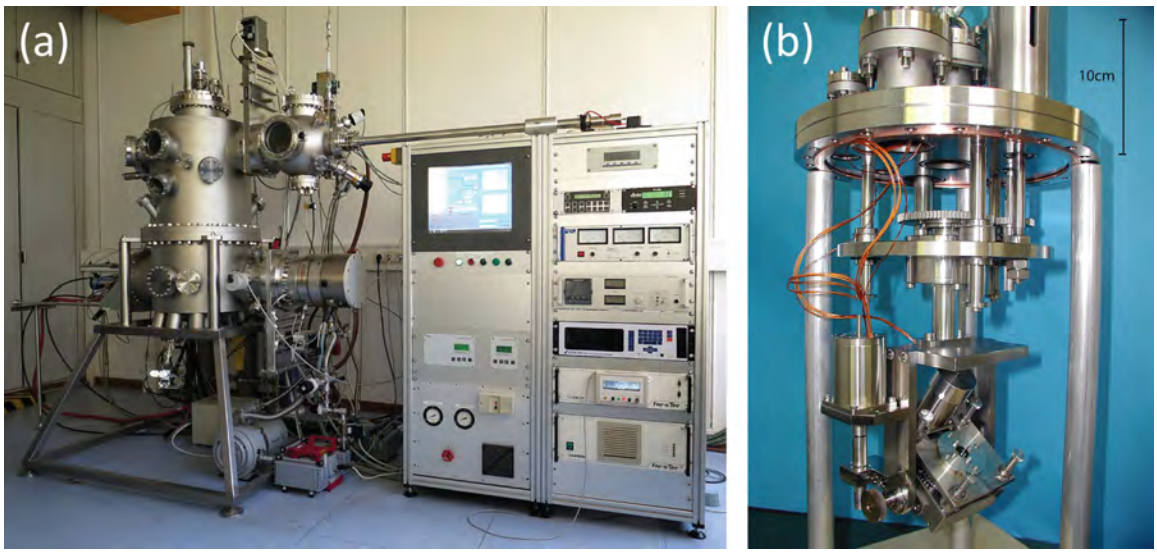

Figure 4: (a) Photograph of the UHV electron beam evaporation system. (b) Manipulator with UHV stepping motors for automated and precise sample tilt and options for rotation.

Single Crystal Growth and Synthesis of Bulk Materials

Transition metal oxides are of great interest due to their various interesting physical properties (e.g. high temperature superconductivity, colossal magnetoresistance, ferroelectricity, nonlinear optical properties etc.) and their high potential for applications. Therefore, the WMI operates a laboratory for the synthesis of bulk materials and single crystals of transition metal oxides. Besides various chamber- and tube furnaces a four-mirror image furnace is used for the crystal growth of various oxide systems. With this furnace crystals of many different compounds of the high temperature superconductors and various other transition metal oxides have been grown as single crystals using the traveling solvent floating zone technique. The furnace consists basically of 4 elliptical mirrors with a common focus on the sample rod and with halogen lamps in their other focus. By irradiation of the focused light the sample rod is locally heated and eventually molten. The molten zone can be moved up and down along the entire sample rod under simultaneous rotation. Due to the anisotropic growth velocity a preferential growth of those grains with the fastest growth velocity along the pulling direction is obtained and the formerly polycrystalline rod is transformed into a single crystal. Single crystal growth can be performed with this furnace at maximum temperatures up to 2200 °C in the pressure range from 10^{-5} mbar up to 10 bar and in oxidizing, reducing as well as inert atmosphere.

Figure 5: The four-mirror image furnace installed at the crystal laboratory of the WMI. Crystals can be grown by the floating zone and traveling solvent floating zone techniques at temperatures up to 2200 °C and pressures up to 10 bar.

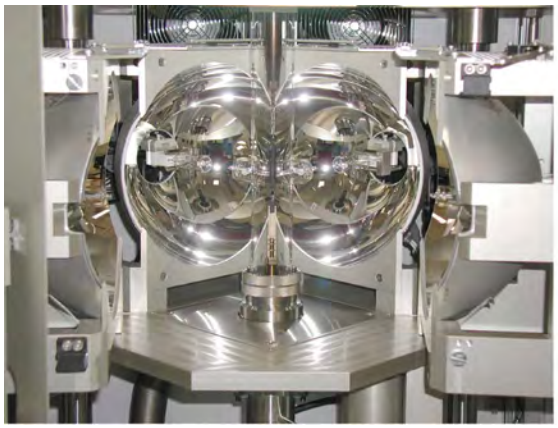

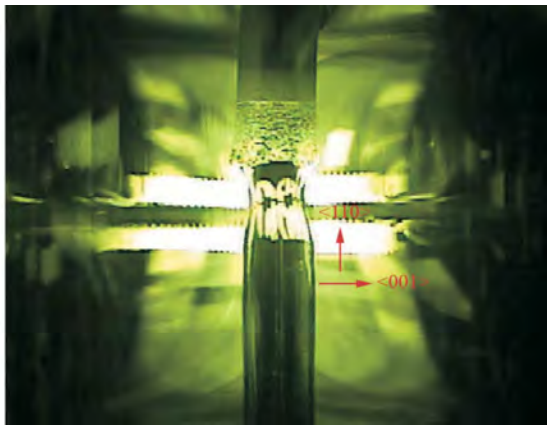

Figure 6: Left: Central part of the image furnace with four elliptical mirrors. In the center one can see the quartz tube with a polycrystalline rod. Right: View on the molten zone of $Pr_{2-x}Ce_xCuO_4$ (melting point: 1280 °C) obtained by a CCD camera.

The X-ray diffraction systems

For X-ray analysis the Walther-Meissner-Institute operates two X-ray diffractometers (Bruker D8 Advance and D8 Discover). The two-circle system is used for powder diffraction. In this system the samples can be heated in oxygen atmosphere up to 1600 °C. It is equipped with a Göbel mirror and an area detector to save measuring time. The second system is a high resolution four-circle diffractometer that can be used for reciprocal space mappings. It is equipped with a Göbel mirror and an asymmetric two-fold Ge monochromator and allows for the texture analysis of thin film superlattices and single crystalline materials. In both systems measurements can be carried out fully computer controlled.

Beside these two Bruker X-ray systems a Laue camera for single crystal analysis and a Debye-Scherrer camera are available.

Figure 7: The two-circle X-ray diffractometer Bruker D8 Advance.

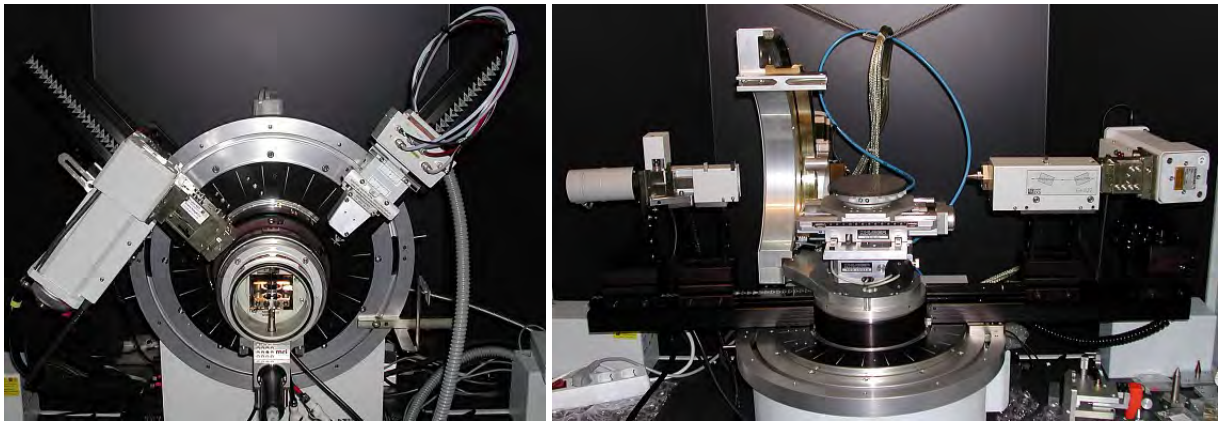

Figure 8: Left: High temperature sample holder of the D8 Advance system. Right: Four-circle high resolution X-ray diffractometer Bruker D8 Discover.

Figure 9: Quantum Design SQUID magnetometer.

The SQUID magnetometer

For the analysis of the magnetic properties of materials, a Quantum Design SQUID magnetometer system (Fig. 9) is operated at the WMI. The SQUID magnetometer allows for measurements in the temperature regime from 1.8 to 400 K and provides excellent sensitivity particularly in the low field regime. Due to the excellent sensitivity of the system, thin film samples with a very small sample volume can be analyzed. The SQUID magnetometer is equipped with a superconducting solenoid allowing for a maximum field of 7 T. At present, the magnetometer is used for the characterization of magnetic and superconducting materials (both in bulk and thin film form). Examples are the cuprate high temperature superconductors, the doped manganites, magnetite, the double perovskites, magnetic semiconductors, or multiferroics.

The High Field Laboratory

Transport and thermodynamic properties of samples are often studied as a function of the applied magnetic field. For such measurements several superconducting magnets are available at the WMI. Two of them (8/10 and 15/17 Tesla magnet system) are located in the high magnetic field laboratory in the basement of the WMI. The magnet systems are installed below the floor level to facilitate the access to the top flange and the change of the sample sticks. The magnet systems are decoupled from the building to avoid noise due to mechanical vibrations. A variety of sample holders can be mounted allowing for e.g. sample rotation during the measurement. For standard sample holders the accessible temperature regime is 1.5 K $< T <$ 300 K. However, also ^{3}He/^{4}He dilution refrigerator inserts ($T >$ 20 mK) or high temperature units ($T <$ 700 K) can be mounted. All measurements are fully computer controlled (by the use of the LabView software tool) allowing for remote control and almost continuous measurements.

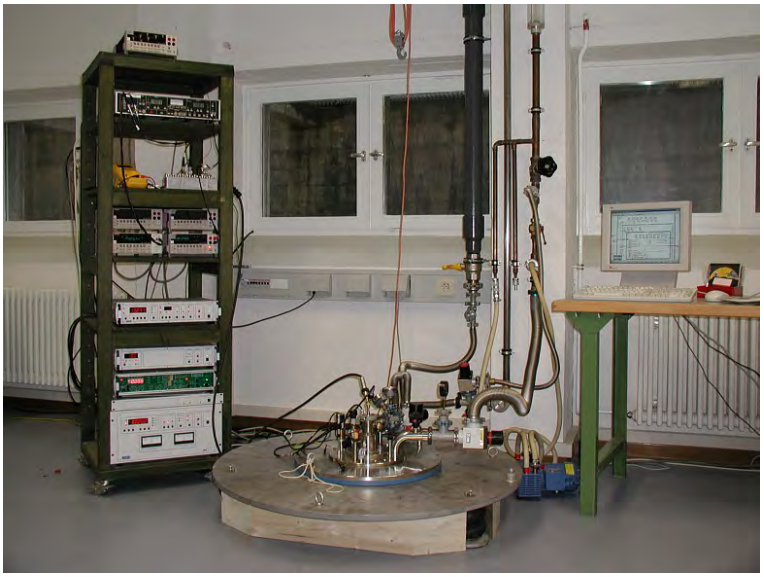

Figure 10: High field laboratory with Oxford 17 T magnet system.

Since 2012, a 3D vector magnet with variable temperature insert, allowing for 2 T in-plane and 6 T out-of-plane magnetic fields is available for thermal and electrical transport experiments.

A further 3D vector magnet allowing for 1 T in-plane and 6 T out-of-plane magnetic fields is installed in the WMI Quantum Laboratories as part of a cryogen-free dilution system.

The Clean Room Facility

For the fabrication of solid state nanostructures and quantum circuits including superconducting, spintronic and nanomechanical devices the WMI operates a class 1000 clean room facility with an area of about 50 m^2. This clean room facility has been put into operation at the WMI within the year 2001. The clean room is subdivided into two parts for photolithography and electron beam lithography, respectively. The clean room facility is equipped with the standard tools for photolithography such as resist coaters, hot plates, wet benches, a Karl Süss MJB3 mask aligner and an optical projection lithography system. The technical infrastructure for the clean room is located in the basement of the WMI directly below the clean room area.

Since 2005 the clean room also is equipped with a reactive ion etching system, Plasmalab 80 Plus with ICP plasma source (Oxford Instruments Plasma Technology).

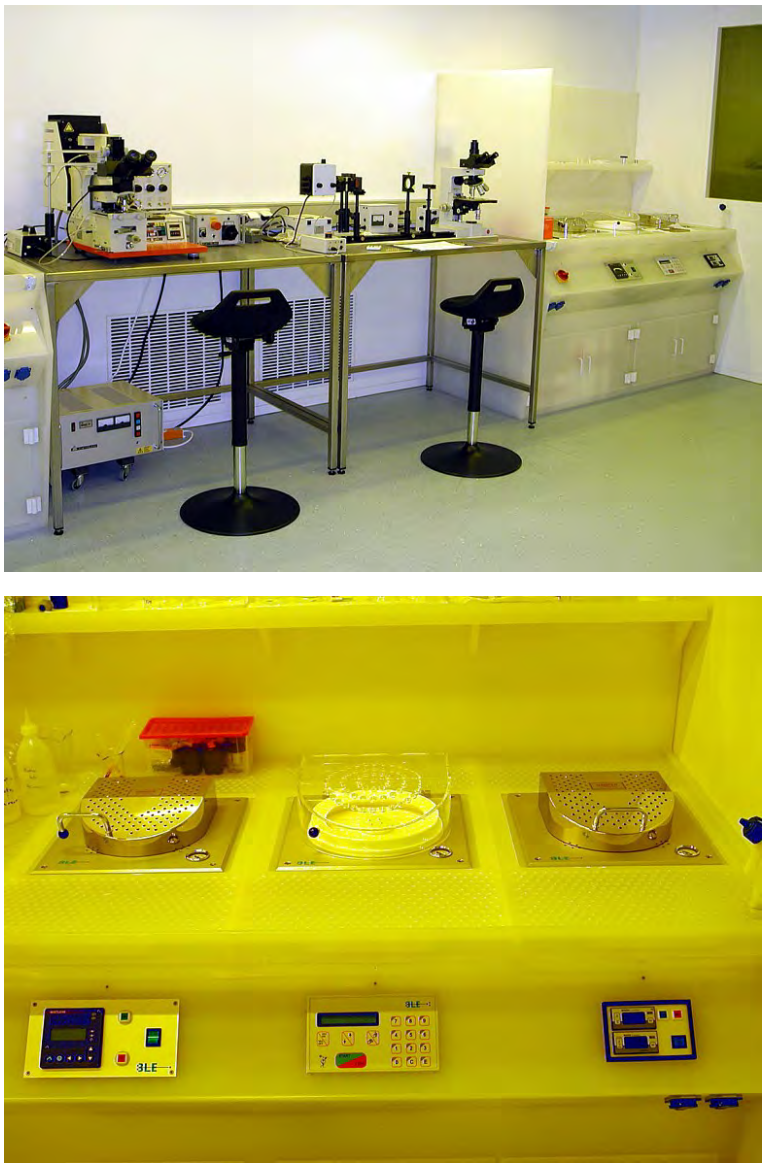

Figure 11: Top: Part of the clean room facility with optical lithography equipment and clean room benches. Bottom: Resist coater and hot plates.

Electron Beam Lithography

Figure 12: 100 kV Electron Beam Lithography System nB5 of NanoBeam Ltd., UK, inside the WMI cleanroom facility.

The 100 kV Electron Beam Lithography System nB5 fabricated by NanoBeam Ltd., UK, is installed in the second part of the clean room facility. The nB5 is a round-beam step-and-repeat system oriented towards high-end R&D applications at universities and research institutes. It is designed for nanopatterning and mix-and-match lithography. The innovative design of the electron optics and automation system enhances its throughput and reliability. It is an ideal tool for nano-device research and production. The electron beam lithography is used for the fabrication of nanostructures in metallic and oxide systems required for the study of quantum effects in mesoscopic samples.

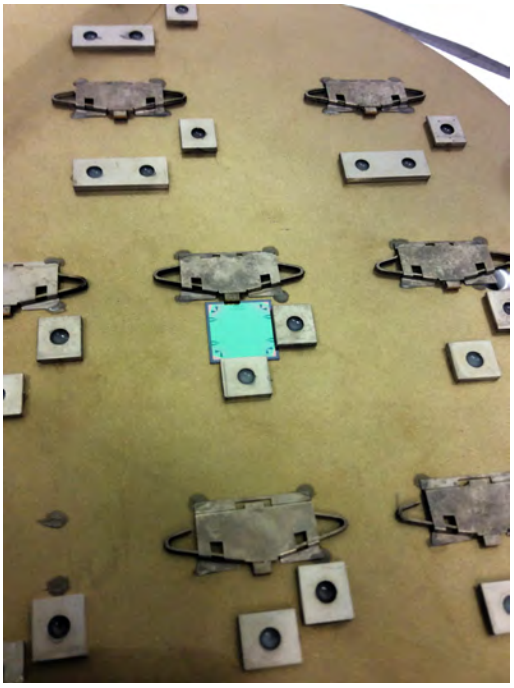

Figure 13: Chuck of the nB5 e-beam lithography system with a mounted $12 \times 12\,\mathrm{mm}^2$ silicon wafer.

The nB5 Electron Beam Lithography System employs low Coulomb-effect electron optics and sophisticated column designs to reduce beam size. The shorter optical column eliminates column bending and reduces system vibration. The modern electronics has low noise and low thermal effects. The perfectly integrated machine structure greatly improves system settling time and total stage move time. The advanced vibration tracking design enables the nB5 system to write on the fly. All these features combined with the fast deflection speed and high data processing rate make the nB5 the highest throughput system available today. Moreover, the nB5 requires undemanding cleanroom conditions, in particular regarding temperature stability, stray field magnitude, and floor vibration level.

The nB5 system is equipped with a thermal field emitter (TFE), an electrostatic lens and magnetic condenser lens, a conjugate beam blanking at $< 5\,\mathrm{ns}$ slew rate and a dual beam deflection. The latter is used to achieve ultra-high deflec-

tion speed for beam writing (clock rate: 55 MHz). The total deflection coverage is combined with the mainfield and the subfield and controlled by two independent deflection sub-systems (field size: 1000 μm, address resolution: 1 nm). The characteristic performance parameters of the electron optics of the nB5 system are: (i) beam voltage range: 20 kV to 100 kV, (ii) minimum beam current: 0.1 nA, (iii) maximum beam current: 100 nA, (iv) theoretical beam size: 2.3 nm at 100 kV, (v) guaranteed writing beam size: < 5 nm at 2 nA, (vi) beam current drift: $< 0.5\%$/hour at 5 nA, (vii) beam position drift: < 50 nm/hour for 3 nA beam current, including blanking, deflection and stage move.

The XY-stage allows for a traversal distance of 200 mm with a total stage move time of only 150 ms for 1 mm stage movement and a position measurement resolution of 0.3 nm using laser interferometry. The maximum substrate sizes are $2-8$ in for round substrates, $2-5$ for square glass masks up to 3 mm thickness. Finally, the nB5 system has airlock operation with automatic loading robotics with a loading cassette for 6 chucks with a maximum diameter of 8 inch.

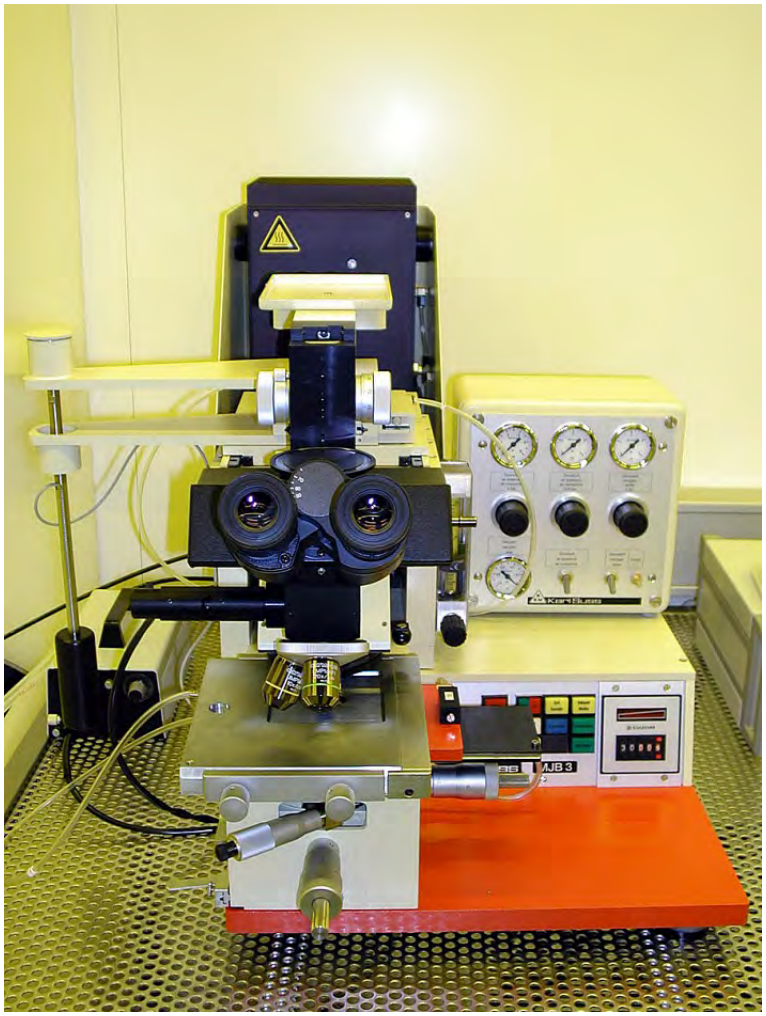

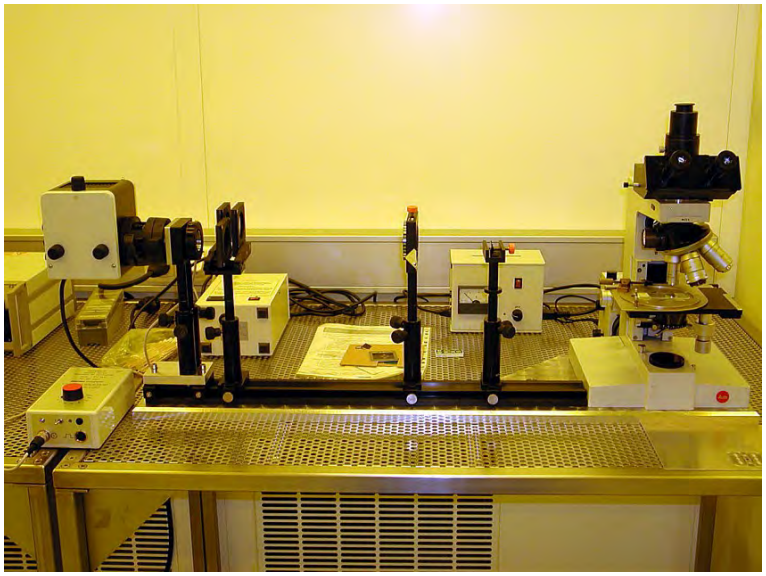

Figure 14: Top: Süss MJB 3 maskaligner for optical lithography. Bottom: Optical projection lithography based on an optical microscope.

Optical Lithography

For photolithography, a Karl Süss MJB 3 maskaligner or an optical microscope based projection system are used. The maskaligner operates in the 1 : 1 soft or hard contact mode and uses chromium metal masks. In the projection system the mask pattern is demagnified by a factor of 5 to 100. Therefore, cheap foil masks can be used. With both systems microstructures with a lateral dimension down to 1 µm can be fabricated.

Low and Ultra-Low Temperature Facilities

At the WMI, we have constructed the first dilution refrigerator with pulse tube pre-cooling for ultra-low temperature experiments. This type of refrigerator works without cryo-liquids, and thus is a lot more practical, more economical and more reliable than cryostats with liquid helium pre-cooling. These days, all major cryo-engineering companies are offering commercial versions of this Millikelvin cooler, and these so-called "dry" refrigerators outsell conventional refrigerators by a wide margin. The general construction concept of most manufacturers is unchanged from our original prototype, where the refrigerator consists of three basic components. The first cooling stage is a commercial pulse tube cryocooler which reaches a base temperature of 2.5 K. The second stage is a Joule-Thomson stage, and the last stage is a dilution refrigeration stage, where the lowest temperature of the cryostat is about 0.01 K (Fig. 15).

Figure 15: The "dry" dilution refrigerator of the WMI.

Figure 16: Low-temperature unit of a WMI dilution refrigerator ready to go into a cryostat.

Figure 17: Two mixing chamber mounting plates with silver sponges. Those are needed to overcome the thermal resistance (Kapitza resistance) between the liquid ^{3,4}He and the mounting plate of the mixing chamber. To fabricate the mounting of the sponge (square pins embedded in the sponge) a spark erosion technique has been employed.

In many low temperature applications high refrigeration capacities are required. Our design allows for a high circulation rate of ^{3}He which in the end determines the cooling power of a dilution refrigerator. Presently our "dry" fridge reaches a refrigeration capacity of 700 µW at a temperature of the mixing chamber of 0.1 K, seven times the cooling power of the WMI nuclear demagnetization cryostat. Goals of our present work are a further increase of cooling power and a lower base temperature of the dry dilution refrigerator.

A smaller version of our cryogen-free fridge has become commercially available by *Oxford Instruments* (formerly *VeriCold Technologies, Ismaning*). It has a refrigeration capacity of 250 µW

at a mixing chamber temperature of 0.1 K (Fig. 16).

The WMI also develops and fabricates dilution refrigerator inserts for temperatures down to about 20 mK. The inserts fit into all cryogenic systems (e.g. superconducting magnets) having a two inch bore. They allow fast sample change and rapid cool down cycles of less than five hours. The dilution refrigerator inserts are engineered and fabricated in-house and are also provided to other low temperature laboratories for ultra-low temperature experiments.

Millikelvin Temperatures in Combination with 3D Vector Magnetic-Fields

Figure 18: The dilution refrigerator with the 3D vector magnet located in the Quantum Laboratories.

In one room of the WMI Quantum Laboratories a cryogen-free dilution refrigerator is installed. This system is equipped with a 3D vector magnet allowing for 1 T in-plane and 6 T out-of-plane magnetic fields. Additional microwave coaxial lines allow for the microwave spectroscopy up to 18 GHz under these experimental conditions.

Scientifically, several directions in the field of fundamental light-matter interaction are envisaged:

(i) Circuit quantum electrodynamics (circuit QED), where superconducting qubits form hybrids with microwave resonators. These experiments are time consuming, because quantum effects arise in the limit of low excitation numbers. Hereby, challenging requirements are imposed on the detection systems allowing to detect microwave signals in the attowatt regime.

(ii) Storage of quantum states. One possibility is the transfer of the quantum information contained in photons to long-lived spin states. Additionally, exchange coupled systems or ferromagetic systems come into focus, because the effective coupling strength scales with the square-root of the number of spins contributing. In general, we study the light-matter interaction with long-lived spin systems and integrate superconducting quantum circuits.

(iii) Spin systems. Here, the investigations are not limited to paramagnetic spin systems, but will be extended to exchange coupled (ferro-) magnetic systems. Hereby, magnetization damping can be investigated as a function of temperature, frequency and magnetic field direction.

(iv) Circuit electro-mechanical hybrid systems consisting of a nano-mechanical element coupled to a superconducting microwave resonator. In this context, sideband cooling of the mechanical system into its ground state and pulsed spectroscopy of hybrid system are performed and will be extended.

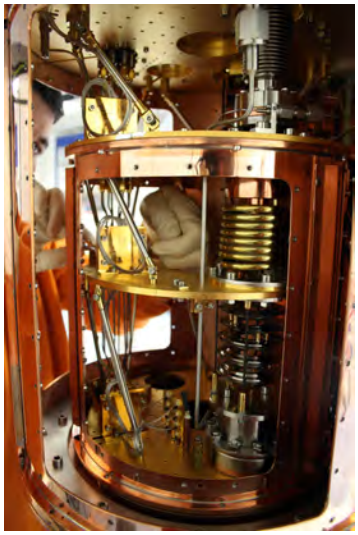

Figure 19: Inside of the dilution system. The windows of the 4 K and the still shield are removed providing access to the low temperature stages.

WMI Millikelvin Facilities for Experiments with Superconducting Quantum Circuits

The research on superconducting quantum circuits at WMI focuses mainly on systems sensitive to externally applied flux (flux qubits), circuit QED systems where flux qubits are coupled to transmission line resonators, squeezing physics in flux driven Josephson parametric amplifiers, and propagating quantum microwaves (e.g., quantum state reconstruction methods). In order to further develop our activities on quantum effects in the microwave regime, additional cryogenic capacities at millikelvin temperatures have been established. In addition to sufficient cooling power, the specifications for these cryostats are mainly dictated by the dimensions (typically a few centimeters in each direction) of bulky microwave components such as circulators or microwave switches.

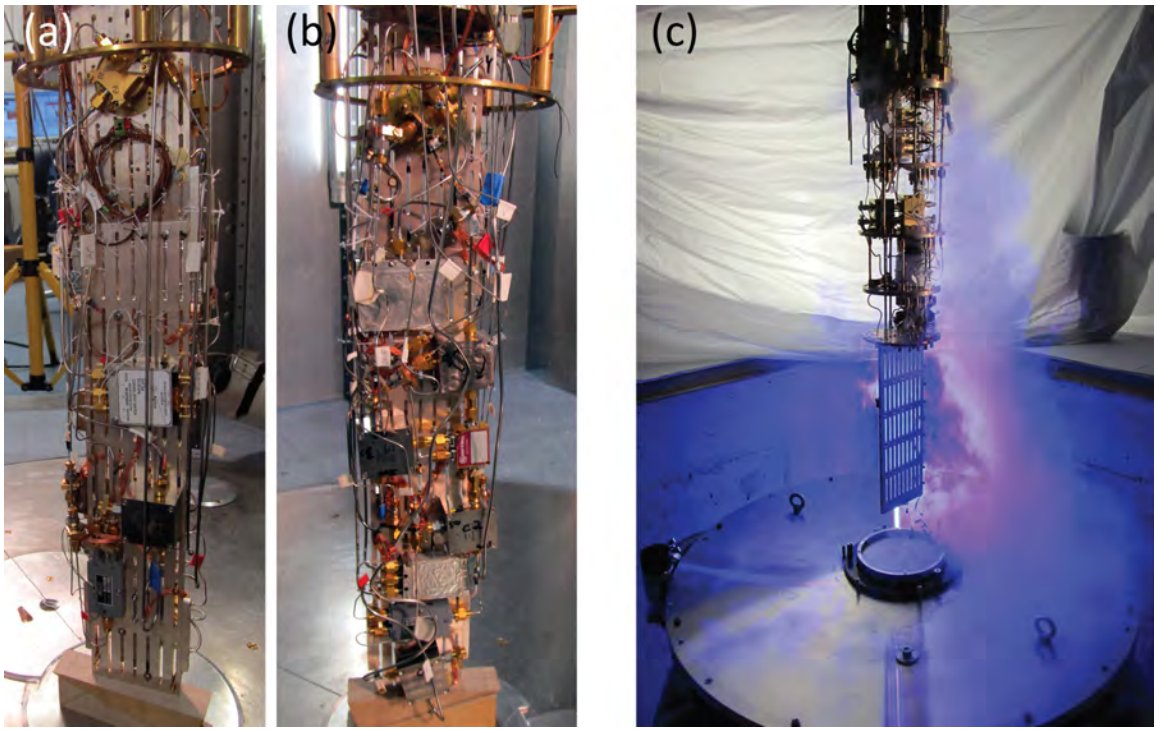

Figure 20: Liquid-helium precooled dilution refrigerators for experiments with superconducting quantum circuits. (a), (b) Back and front sides of the sample stage of the K12-refrigerator equipped with four circuit QED experiments. The height of the silver rod is 50 cm. (c) Sample stage and dewar of the dilution refrigerator in the quantum laboratory K04.

Two liquid-helium precooled dilution refrigerators are available for experiments with superconducting quantum circuits. The dilution refrigerator in laboratory K12 provides a sample space with a cylindrical volume with 11 cm diameter 55 cm height. The refrigerator is equipped with four microwave amplifiers at the 4 K-stage, seven broadband input lines and 80 twisted pair DC lines. This allows for mounting four experiments simultaneously to avoid idle times by interleaved measurements (see Fig. 20(a) and (b)). The base temperature of this refrigerator is 20 mK.

A new liquid-helium precooled dilution refrigerator for experiments with superconducting quantum circuits has been set up in the quantum laboratory K04. To provide enough space at the sample stage we have installed a Cryogenic Ltd. stainless steel dewar with a ^{4}He volume of 89 l. The time between two refills exceeds nine days. The cryostat is equipped with 16 coaxial measurement lines suitable for microwave frequencies down to the mixing chamber stage and low-noise cryogenic high electron mobility transistor (HEMT) amplifiers. Presently up to four samples can be mounted simultaneously to the sample stage. By expanding the number of input lines in the near future a more complex experiment can be set up. The cooling power of

the mixing chamber at 100 mK was determined to about 140 µW.

A new cryogen-free dilution refrigerator with a pulse tube refrigerator (PTR) for precooling and with a large sample stage has been set up in room K21 of the WMI Quantum Laboratories using the longstanding experience in dry dilution refrigerators at WMI. This refrigerator features large diameters (tens of centimeters) of all temperature stages providing sufficient space for advanced quantum experiments. The main components of the refrigerator are the PTR, a 1 K-stage and a dilution unit. The two stages of the PTR cool the incoming ^{4}He and the ^{3}He/^{4}He mixture as well as one radiation shield at each stage. To provide sufficiently high cooling power near 1 K to cool microwave components and cables, this refrigerator has been equipped with a 1 K-stage operating in a closed cycle. A refrigeration capacity of the 1 K-stage of up to 100 mW could be reached. The dilution refrigerator is precooled by a dedicated ^{4}He circuit. The minimum base temperature of the refrigerator is below 11 mK. The cooling power at 100 mK was determined to about 300 µW at the maximum ^{3}He flow rate.

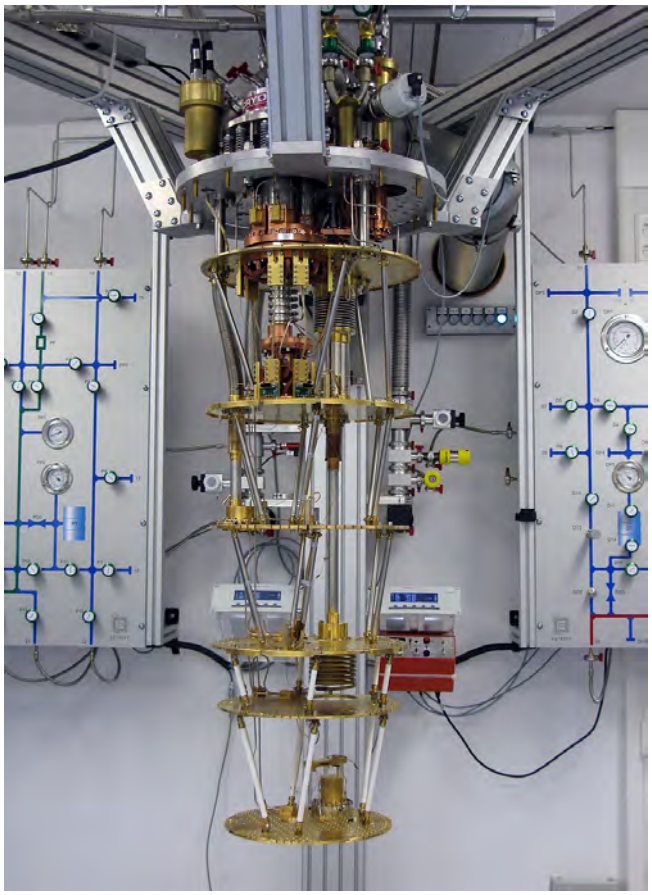

Figure 21: Dry dilution refrigerator with a large sample space.

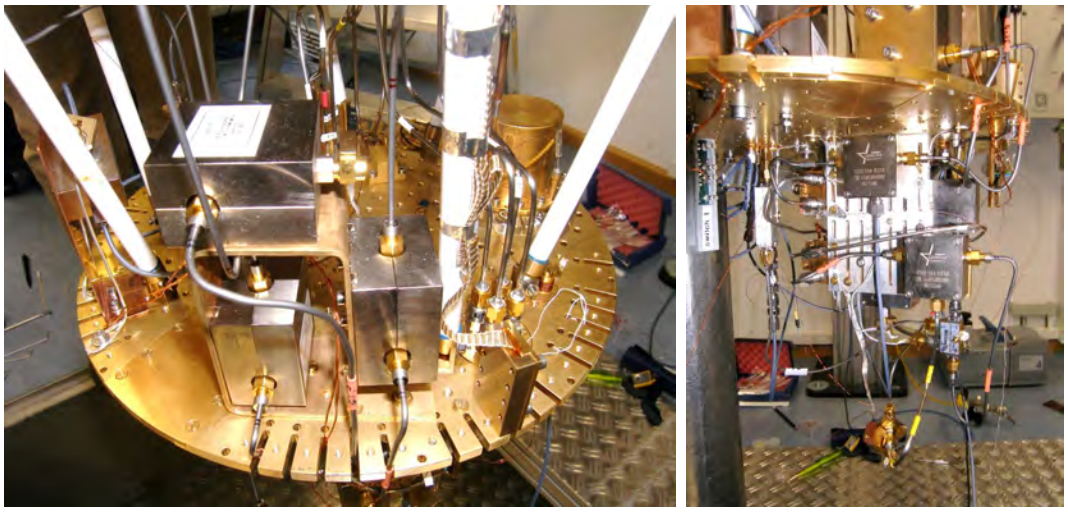

Figure 22: Low temperature platform of K21 dilution refrigerator with experimental setup for circuit QED experiments.

Publications

1. **Laser Molecular Beam Epitaxy of ZnO Thin Films and Heterostructures**
Matthias Opel, Stephan Geprägs, Matthias Althammer, Thomas Brenninger, Rudolf Gross
J. Phys. D: Appl. Phys. **47**, 034002 (2014).

2. **Dual-Path Methods for Propagating Quantum Microwaves**
R. Di Candia, E. P. Menzel, L. Zhong, F. Deppe, A. Marx, R. Gross, E. Solano
New. J. Phys. **16**, 015001 (2014).

3. **Interactions and Chemical Transformations of Coronene Inside and Outside Carbon Nanotubes**
Bea Botka , Melinda E. Füstös , Hajnalka M. Tóháti , Katalin Németh , Gyöngyi Klupp , Zsolt Szekrényes , Dorina Kocsis , Margita Utczás , Edit Székely , Tamás Váczi , György Tarczay , Rudi Hackl , Thomas W. Chamberlain , Andrei N. Khlobystov, and Katalin Kamarás
Small **10**, 1369-1378 (2014).

4. **Zinc Oxide - From Dilute Magnetic Doping to Spin Transport**
Matthias Opel, Sebastian T.B. Goennenwein, Matthias Althammer, Karl-Wilhelm Nielsen, Eva-Maria Karrer-Müller, Sebastian Bauer, Konrad Senn, Christoph Schwark, Christian Weier, Gernot Güntherodt, Bernd Beschoten, Rudolf Gross
Phys. Status Solidi B **251**, No. 9, 1700-1709 (2014) .

5. **Dry Dilution Refrigerator With ^{4}He Precool Loop**
K. Uhlig
AIP Conference Proceedings Vol. **1573**, 1393-1398 (2014).

6. **Strain-controlled Nonvolatile Magnetization Switching**
Stephan Geprägs, Andreas Brandlmaier, Martin S. Brandt, Rudolf Gross, Sebastian T.B. Goennenwein
Solid State Communications **198**, 7-12 (2014).

7. **Unambiguous Determination of Spin Dephasing Times in ZnO by Time-resolved Magneto-optical Pump-probe Experiments**
Sebastian Kuhlen, Ralph Ledesch, Robin de Winter, Matthias Althammer, Sebastian T.B. Goennenwein, Matthias Opel, Rudolf Gross, Thomas A. Wassner, Martin S. Brandt, Bernd Beschoten
Phys. Status Solidi B **251**, No. 9, 1861-1871 (2014).

8. **Investigation of Induced Pt Magnetic Polarisation in Pt/$Y_3Fe_5O_{12}$ Bilayers**
Stephan Geprägs, Sibylle Meyer, Stephan Altmannshofer, Matthias Opel, Fabrice Wilhelm, Andrei Rogalev, Rudolf Gross, Sebastian T.B. Goennenwein
ESRF Highlights 2013, pp. 88–89 (2014).

9. **A Raman study of the temperature and magnetic field dependence of electronic and lattice properties in MnSi**
H.-M. Eiter, P. Jaschke, R. Hackl, A. Bauer, M. Gangl, C. Pfleiderer
Phys. Rev. B **90**, 024411 (2014).

10. **The EURECA Collaboration**
G. Angloher, E. Armengaud, C. Augier, A. Benoit, T. Bergmann, J. Blümer, A. Broniatowski, V. Brudanin, P. Camus, A. Cazes, M. Chapellier, N. Coron, G.A. Cox, C. Cuesta, F. A. Danevich, M. De Jésus, L. Dumoulin, K. Eitel, A. Erb, A. Ertl, F. von Feilitzsch, D. Filosofov, N. Fourches, E. García, J. Gascon, G. Gerbier, C. Ginestra, J. Gironnet, A. Giuliani, M. Gros, A. Gütlein, D. Hauff, S. Henry, G. Heuermann, J. Jochum, S. Jokisch, A. Juillard, C. Kister, M. Kleifges, H. Kluck, E. V. Korolkova, V. Y. Kozlov, H. Kraus, V. A. Kudryavtsev, J.-C. Lanfranchi, P. Loaiza, J. Loebell, I. Machulin, S. Marnieros, M. Martínez, A. Menshikov, A. Münster, X.-F. Navick, C. Nones, Y. Ortigoza, P. Pari, F. Petricca, W. Potzel, P. P. Povinec, F. Pröbst, J. Puimedón, F. Reindl, M. Robinson, T. Rolón, S. Roth, K. Rottler, S. Rozov, C. Sailer, A. Salinas, V. Sanglard, M. L. Sarsa, K. Schäffner, B. Schmidt, S. Scholl, S. Schönert, W. Seidel, B. Siebenborn, M. v. Sivers, C. Strandhagen, R. Strauß, A. Tanzke, V. I. Tretyak, M. Turad, A. Ulrich, I. Usherov, P. Veber, M. Velazquez, J. A. Villar, O. Viraphong, R. J. Walker, S. Wawoczny, M. Weber, M. Willers, M. Wüstrich, E. Yakushev, X. Zhang, A. Zöller

Physics of the Dark Universe **3**, 41-74 (2014).

11. **Nano- and Microstructures of Magnetic Field-Guided Maghemite Nanoparticles in Diblock Copolymer Films**
Yuan Yao, Ezzeldin Metwalli, Martin A. Niedermeier, Matthias Opel, Chen Lin, Jing Ning, Jan Perlich, Stephan V. Roth, Peter Müller-Buschbaum
ACS Appl. Mater. Interfaces **6**, 5244-5254 (2014).

12. **Temperature dependent spin transport properties of Platinum inferred from spin Hall magnetoresistance measurements**
Sibylle Meyer, Matthias Althammer, Stephan Geprägs, Matthias Opel, Rudolf Gross, Sebastian T. B. Goennenwein
Appl. Phys. Lett. **104**, 242411 (2014).

13. **Energy-dependent light quenching in $CaWO_4$ crystals at mK temperatures**
R. Strauss, G. Angloher, A. Bento, C. Bucci, L. Canonica, W. Carli, A. Erb, F. von Feilitzsch, P. Gorla, A. Gütlein, D. Hauff, D. Hellgartner, J. Jochum, H. Kraus, J.-C. Lanfranchi, J. Loebell, A. Münster, F. Petricca, W. Potzel, F. Pröbst, F. Reindl, S. Roth, K. Rottler, C. Sailer, K. Schäffner, J. Schieck, S. Scholl, S. Schönert, W. Seidel, M. von Sivers, L. Stodolsky, C. Strandhagen, A. Tanzke, M. Uffinger, A. Ulrich, I. Usherov, S. Wawoczny, M. Willers, M. Wüstrich and A. Zöller
Eur. Phys. J. C **74**, 2957 (2014).

14. **A carrier relaxation bottleneck probed in single InGaAs quantum dots using integrated superconducting single photon detectors**
G. Reithmaier, F. Flassig, P. Hasch, S. Lichtmannecker, K. Müller, J. Vuckovic, R. Gross, M. Kaniber, J. J. Finley
Appl. Phys. Lett. **105**, 081107 (2014).

15. **Real Time Electrical Detection of Coherent Spin Oscillations**
F. Hoehne, C. Huck, M. S. Brandt, H. Huebl
Phys. Rev. B **89**, 161305(R) (2014).

16. **Festkörperphysik**, 2. aktualisierte Auflage
R. Gross, A. Marx
Walther de Gruyter GmbH, Berlin/Boston (2014), ISBN 978-3-11-035870-4.

17. **Circuit-quantum electrodynamics with direct magnetic coupling to single-atom spin qubits in isotopically enriched ^{28}Si**
Guilherme Tosi, Fahd A. Mohiyaddin, Hans Huebl, and Andrea Morello
AIP Advances **4**, 087122 (2014).

18. **Theoretical model for torque differential magnetometry of single-domain magnets**
Akashdeep Kamra, Michael Schreier, Hans Huebl, and Sebastian T. B. Goennenwein
Phys. Rev. B **89**, 184406 (2014).

19. **Time resolved spin Seebeck effect experiments**
Niklas Roschewsky, Michael Schreier, Akashdeep Kamra, Felix Schade, Kathrin Ganzhorn, Sibylle Meyer, Hans Huebl, Stephan Geprägs, Rudolf Gross, Sebastian T. B. Goennenwein
Appl. Phys. Lett. **104**, 202410 (2014).

20. **Magnetic quantum oscillations in the charge-density-wave state of the organic metals α-(BEDT-TTF)$_2$MHg(SCN)$_4$ with M = K and Tl**
M. V. Kartsovnik, V. N. Zverev, D. Andres, W. Biberacher, T. Helm, P. D. Grigoriev, R. Ramazashvili, N. D. Kushch, H. Müller
Low Temperature Physics **40**, 377-383 (2014).

21. **Determination of effective mechanical properties of a double-layer beam by means of a nano-electromechanical transducer**
Fredrik Hocke, Matthias Pernpeintner, Xiaoqing Zhou, Albert Schliesser, Tobias J. Kippenberg, Hans Huebl, Rudolf Gross
Appl. Phys. Lett. **105**, 133102 (2014).

22. **Circuit Electromechanics with a Non-Metallized Nanobeam**
Matthias Pernpeintner, Thomas Faust, Fredrik Hocke, Jörg P. Kotthaus, Eva M. Weig, Hans

Huebl, Rudolf Gross
Appl. Phys. Lett. 105, 123106 (2014).

23. **Self-Assembly of Diblock Copolymer-Maghemite Nanoparticle Hybrid Thin Films**
Yuan Yao, Ezzeldin Metwalli, Jean-FrancÂÿois Moulin, Bo Su, Matthias Opel, Peter Müller-Buschbaum
ACS Appl. Mater. Interfaces **6**, 18152-18162 (2014).

24. **Spin Hall noise**
Akashdeep Kamra, Friedrich P. Witek, Sibylle Meyer, Hans Huebl, Stephan Geprägs, Rudolf Gross, Gerrit E. W. Bauer, Sebastian T. B. Goennenwein
Phys. Rev. B **90**, 214419 (2014).

25. **Spin Hall Magnetoimpedance**
Johannes Lotze, Hans Huebl, Rudolf Gross, Sebastian T. B. Goennenwein
Phys. Rev. B **90**, 174419 (2014).

26. **A balancing act: Evidence for a strong subdominant d-wave pairing channel in $Ba_{0.6}K_{0.4}Fe_2As_2$**
T. Böhm, A. F. Kemper, B. Moritz, F. Kretzschmar, B. Muschler, H.-M. Eiter, R. Hackl, T. P. Devereaux, D. J. Scalapino, Hai-Hu Wen
Phys. Rev. X **4**, 041046 (2014).

27. **High magnetic field studies of the vortex lattice structure in $YBa_2Cu_3O_7$**
A.S. Cameron, J.S. White, A.T. Holmes, E. Blackburn, E.M. Forgan, R. Riyat, T. Loew, C.D. Dewhurst, A. Erb
Phys. Rev. B **90**, 054502 (2014).

28. **Distribution of electrons and holes in cuprate superconductors as determined from ^{17}O and ^{63}Cu nuclear magnetic resonance**
Michael Jurkutat, Damian Rybicki, Oleg P. Sushkov, Grant V. M. Williams, Andreas Erb, Jürgen Haase
Phys. Rev. B **90**, 140504(R) (2014).

29. **Results on low mass WIMPs using an upgraded CRESST-II detector**
CRESST collaboration: G. Angloher, A. Bento, C. Bucci, L. Canonica, A. Erb, F. v. Feilitzsch, N. Ferreiro Iachellini, P. Gorla, A. Gütlein, D. Hauff, P. Huff, J. Jochum, M. Kiefer, C. Kister, H. Kluck, H. Kraus, J.-C. Lanfranchi, J. Loebell, A. Münster, F. Petricca, W. Potzel, F. Pröbst, F. Reindl, S. Roth, K. Rottler, C. Sailer, K. Schäffner, J. Schieck, J. Schmaler, S. Scholl, S. Schönert, W. Seidel, M. v. Sivers, L. Stodolsky, C. Strandhagen, R. Strauss, A. Tanzke, M. Uffinger, A. Ulrich, I. Usherov, M. Wüstrich, S. Wawoczny, M. Willers, A. Zöller
Eur. Phys. J. C **74**, 3184 (2014).

30. **Radiopurity of $CaWO_4$ Crystals for Direct Dark Matter Search with CRESST and EURECA**
A. Münster, M. v. Sivers, G. Angloher, A. Bento, C. Bucci, L. Canonica, A. Erb, F. v. Feilitzsch, P. Gorla, A. Gütlein, D. Hauff, J. Jochum, H. Kraus, J.-C. Lanfranchi, M. Laubenstein, J. Loebell, Y. Ortigoza, F. Petricca, W. Potzel, F. Pröbst, J. Puimedon, F. Reindl, S. Roth, K. Rottler, C. Sailer, K. Schäffner, J. Schieck, S. Scholl, S. Schönert, W. Seidel, L. Stodolsky, C. Strandhagen, R. Strauss, A. Tanzke, M. Uffinger, A. Ulrich, I. Usherov, S. Wawoczny, M. Willers, M. Wüstrich, A. Zöller
JCAP **05**, 018 (2014).

31. **Precision Measurements of Light Quenching in $CaWO_4$ Crystals at mK Temperatures**
R. Strauss, G. Angloher, A. Bento, C. Bucci, L. Canonica, A. Erb, F. v. Feilitzsch, P. Gorla, A. Gütlein, D. Hauff, J. Jochum, H. Kraus, J.-C. Lanfranchi, J. Loebell, A. Münster, F. Petricca, W. Potzel, F. Pröbst, F. Reindl, S. Roth, K. Rottler, C. Sailer, K. Schäffner4 J. Schieck, S. Scholl, S. Schönert, W. Seidel, M. v. Sivers, L. Stodolsky, C. Strandhagen, A. Tanzke, M. Uffinger, A. Ulrich, I. Usherov, S. Wawoczny, M. Willers, M. Wüstrich, A. Zöller, W. Carli, C. Ciemniak, H. Hagn, D. Hellgartner
arXiv:1401.3332, submitted for publication (2014).

32. **Glassiness induced by charge stripe order in 1/8-doped lanthanum cuprates**
S.-H. Baek, M. Hücker, A. Erb, G. D. Gu, B. Büchner, H.-J. Grafe
arXiv:1402.3077, submitted for publication (2014).

33. **Correlation between Fermi surface transformations and superconductivity in the electron-doped high-T_c superconductor $Nd_{2-x}Ce_xCuO_4$**
T. Helm, M. V. Kartsovnik, C. Proust, B. Vignolle, C. Putzke, E. Kampert, I. Sheikin, E.-S. Choi, J. S. Brooks, N. Bittner, W. Biberacher, A. Erb, J. Wosnitza, R. Gross
arXiv:1403.7398, submitted for publication (2014).

34. **Sign of inverse spin Hall voltages generated by ferromagnetic resonance and temperature gradients in yttrium iron garnet | platinum bilayers**
Michael Schreier, Gerrit E. W. Bauer, Vitaliy Vasyuchka, Joost Flipse, Ken-ichi Uchida, Johannes Lotze, Viktor Lauer, Andrii Chumak, Alexander Serga, Shunsuke Daimon, Takashi Kikkawa, Eiji Saitoh, Bart J. van Wees, Burkard Hillebrands, Rudolf Gross, Sebastian T. B. Goennenwein
arXiv:1404.3490, submitted for publication (2014).

35. **Scanning probe microscopy in an ultra-low vibration closed-cycle cryostat**
Francesca Paola Quacquarelli, Jorge Puebla, Thomas Scheler, Dieter Andres, Christoph Bödefeld, Balazs Sipos, Claudio Dal Savio, Andreas Bauer, Christian Pfleiderer, Andreas Erb, Khaled Karrai
arXiv:1404.2046, submitted for publication (2014).

36. **Torque differential magnetometry using quartz tuning forks**
Akashdeep Kamra, Stefan von Hoesslin, Niklas Roschewsky, Johannes Lotze, Michael Schreier, Rudolf Gross, Sebastian T. B. Goennenwein, Hans Huebl
arXiv:1404.6341, submitted for publication (2014).

37. **Tunable and Switchable Coupling Between Two Superconducting Resonators**
A. Baust, E. Hoffmann, M. Haeberlein, M. J. Schwarz, P. Eder, E. P. Menzel, K. Fedorov, J. Goetz, F. Wulschner, E. Xie, L. Zhong, F. Quijandria, B. Peropadre, D. Zueco, J.-J. Garcia Ripoll, E. Solano, F. Deppe, A. Marx, R. Gross
arXiv:1405.1969, submitted for publication (2014).

38. **Origin of the spin Seebeck effect probed by temperature dependent measurements in $Gd_3Fe_5O_{12}$**
Stephan Geprägs, Andreas Kehlberger, Tomek Schulz, Christian Mix, Francesco Della Coletta, Sibylle Meyer, Akashdeep Kamra, Matthias Althammer, Gerhard Jakob, Hans Huebl, Rudolf Gross, Sebastian T.B. Goennenwein, Mathias Kläui
arXiv:1405.4971, submitted for publication (2014).

39. **Ultrafast electronic read-out of diamond NV centers coupled to graphene**
Andreas Brenneis, Louis Gaudreau, Max Seifert, Helmut Karl, Martin S. Brandt, Hans Huebl, Jose A. Garrido, Frank H.L. Koppens, Alexander W. Holleitner
arXiv:1408.1864, submitted for publication (2014).

40. **Impact of Coherent Neutrino Nucleus Scattering on Direct Dark Matter Searches based on $CaWO_4$ Crystals**
A. Gütlein, G. Angloher, A. Bento, C. Bucci, L. Canonica, A. Erb, F. v. Feilitzsch, N. Ferreiro Iachellini, P. Gorla, D. Hauff, J. Jochum, M. Kiefer, H. Kluck, H. Kraus, J.-C. Lanfranchi, J. Loebell, A. Münster, F. Petricca, W. Potzel, F. Pröbst, F. Reindl, S. Roth, K. Rottler, C. Sailer, K. Schäffner, J. Schieck, S. Schönert, W. Seidel, M. v. Sivers, L. Stodolsky, C. Strandhagen, R. Strauss, A. Tanzke, M. Uffinger, A. Ulrich, I. Usherov, S. Wawoczny, M. Willers, M. Wüstrich, A. Zöller
arXiv:1408.2357, submitted for publication (2014).

41. **On-chip generation, routing and detection of quantum light**
Günther Reithmaier, Michael Kaniber, Fabian Flassig, Stefan Lichtmannecker, Kai Müller, Alexander Andrejew, Jelena Vuckovic, Rudolf Gross, Jonathan Finley
arXiv:1408.2275, submitted for publication (2014).

42. **Electron/gamma and alpha backgrounds in CRESST-II Phase 2**
R. Strauss, G. Angloher, A. Bento, C. Bucci, L. Canonica, A. Erb, F. v. Feilitzsch, N. Ferreiro Iachellini, P. Gorla, A. Gütlein, D. Hauff, J. Jochum, M. Kiefer, H. Kluck, H. Kraus, J.-C. Lanfranchi, J. Loebell, A. Münster, F. Petricca, W. Potzel, F. Pröbst, F. Reindl, S. Roth, K. Rottler, C. Sailer, K. Schäffner, J. Schieck, S. Scholl, S. Schönert, W. Seidel, M. v. Sivers, L. Stodolsky, C. Strandhagen, A. Tanzke, M. Uffinger, A. Ulrich, I. Usherov, S. Wawoczny, M. Willers, M. Wüstrich, A. Zöller
arXiv:1410.4188, submitted for publication (2014).

43. **A detector module with highly efficient surface-alpha event rejection operated in CRESST-II Phase 2**
R. Strauss, G. Angloher, A. Bento, C. Bucci, L. Canonica, A. Erb, F. v. Feilitzsch, N. Ferreiro, P. Gorla, A. Gütlein, D. Hauff, J. Jochum, M. Kiefer, H. Kluck, H. Kraus, J.-C. Lanfranchi, J. Loebell, A. Münster, F. Petricca, W. Potzel, F. Pröbst, F. Reindl, S. Roth, K. Rottler, C. Sailer, K. Schäffner, J. Schieck, S. Scholl, S. Schönert, W. Seidel, M. v. Sivers, M. Stanger, L. Stodolsky, C. Strandhagen, A. Tanzke, M. Uffinger, A. Ulrich, I. Usherov, S. Wawoczny, M. Willers, M Wüstrich, A. Zöller
arXiv:1410.1753, submitted for publication (2014).

44. **Pulsed Low-Field Electrically Detected Magnetic Resonance**
L. Dreher, F. Hoehne, H. Morishita, H. Huebl, M. Stutzmann, K. M. Itoh, M. S. Brandt
arXiv:1410.6464, submitted for publication (2014).

45. **Longitudinal spin Seebeck effect contribution in transverse spin Seebeck effect experiments in Pt/YIG and Pt/NFO**
Daniel Meier, Daniel Reinhardt, Michael van Straaten, Christoph Klewe, Matthias Althammer, Michael Schreier, Sebastian T. B. Goennenwein, Arunava Gupta, Maximilian Schmid, Christian H. Back, Jan-Michael Schmalhorst, Timo Kuschel, Günter Reiss
arXiv:1411.6790, submitted for publication (2014).

46. **Dry dilution refrigerator with ^{4}He-1 K-loop**
Kurt Uhlig
arXiv:1412.3597, submitted for publication (2014).

47. **Dry Dilution Refrigerator for Experiments on Quantum Effects in the Microwave Regime**
A. Marx, J. Hoess, and K. Uhlig
arXiv:1412.3619, submitted for publication (2014).

48. **Dry Dilution Refrigerator with He-4 Precool Loop**
Kurt Uhlig
arXiv:1412.3665, submitted for publication (2014).

49. **Current-induced spin torque resonance of a magnetic insulator**
Michael Schreier, Takahiro Chiba, Arthur Niedermayr, Johannes Lotze, Hans Huebl, Stephan Geprägs, Saburo Takahashi, Gerrit E. W. Bauer, Rudolf Gross, Sebastian T. B. Goennenwein
arXiv:1412.7460, submitted for publication (2014).

50. **Magnon-polaritons in Microwave Cavities**
Yunshan Cao, Peng Yan, Hans Huebl, Sebastian T.B. Goennenwein, Gerrit E.W. Bauer
arXiv:1412.5809, submitted for publication (2014).

The accompanying diagram shows the development of the total number of citations per year of papers published by members of WMI since 1996. This number has more than doubled within the last ten years and is exceeding 1500 in 2014.

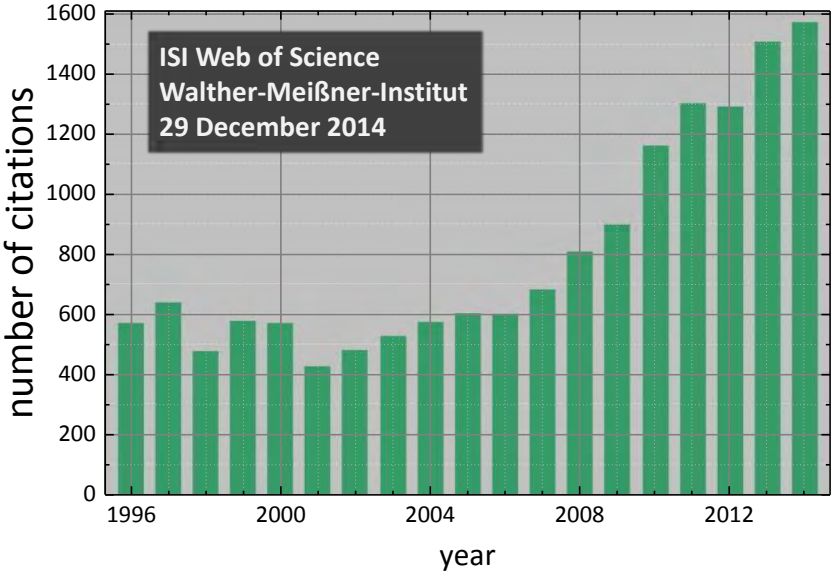

Books

Festkörperphysik (2. überarbeitete und erweiterte Auflage)

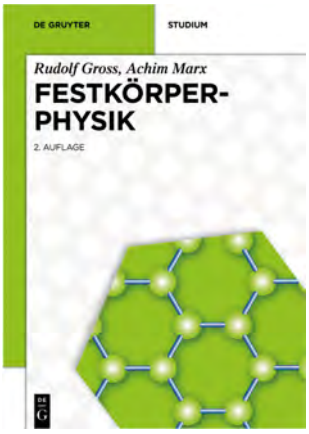

The first edition (2000 copies) of the solid state physics textbook ***Festkörperphysik*** by Rudolf Gross and Achim Marx appeared in 2012. It was receiving very positive reviews (see e.g. review by Prof. Daniel Hägele in Physik Journal **12** (2013) Nr. 10, p. 60). The textbook as well as the related book with exercises and solutions are well received by teachers and highly esteemed by the students. The first edition has been out of print already mid of 2014. The second revised and expanded edition has been published by De Gruyter Oldenbourg in October 2014. It is also available as ebook.

Basic information on the book:

- Title: Festkörperphysik
- Publisher: de Gruyter Oldenbourg, Munich
- Published: October 2014
- Presentation: hardcover, XVIII, 1007 pages, with more than 800 colored illustrations and 50 colored tables
- Language: German
- Size: 240 mm x 170 mm x 63 mm
- Weight: 2026 g
- ISBN-13: 978-3-486-71294-0
- ISBN-10: 3-486-71294-2
- Price: EUR 54,95

Festkörperphysik. Aufgaben und Lösungen

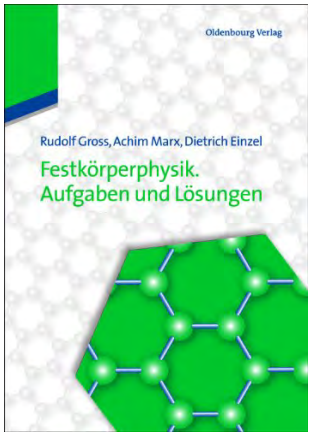

In December 2013, the supplementary book entitled ***Festkörperphysik. Aufgaben und Lösungen*** by Rudolf Gross, Achim Marx and Dietrich Einzel has been published by the Oldenbourg Wissenschaftsverlag München. The book contains model solutions to all exercises listed at the end of the chapters of the related solid state physics textbook ***Festköperphysik***. The book is ideal for preparing for examinations and for learning on one's own.

Basic information on the book:

- Title: Festkörperphysik. Aufgaben und Lösungen
- Publisher: Oldenbourg Wissenschaftsverlag München
- Published: December 18, 2013
- Presentation: paperback, XI, 309 pages, 83 black and white illustrations, 3 tables
- Language: German
- Size: 242 mm x 170 mm x 20 mm
- Weight: 1915 g
- ISBN-13: 9783486712940
- ISBN-10: 3486712942
- eISBN: 978-3-486-85896-9
- Price: EUR 25,70

Bachelor, Master, Doctoral, and Habilitation Theses

Completed and Ongoing Habilitation Theses

Dr. Hans Hübl of WMI was submitting his habilitation thesis entitled ***Quantum Hybrid Systems*** in 2014. It was evaluated positively by the "Habilitationsmentorat" and the international reviewers and finally accepted by the Faculty of Physics of TU Munich in November 2014.

Hans Hübl started the habilitation process in February 2010 with R. Gross (TUM), J.P. Kotthaus (LMU) and P. Vogl (TUM) acting as his mentoring team. Following an intermediate evaluation on 19 July 2012, the mentoring team recommended him to complete the habilitation process at his earliest convenience since most of the objectives in teaching and research agreed on with the mentoring team had already been reached. Hans Hübl then submitted his cumulative habilitation thesis, summarizing his broad research activities, in April 2014.

In the past few years, Hans Hübl developed into an internationally renowned junior scientist. His scientific work impresses not only by the large number but even more by the originality, novelty and relevance of his results. Meanwhile, his publication list contains more than 50 articles in reviewed journals (including 6 in Nature Journals, 12 in Physical Review Letters, 6 in Applied Physics Letters). The total number of citations of his articles is exceeding 1400, with the number of citations quadrupling within the last four years. In 2012, Hans Hübl received the Prize of the Karl Thiemig-Stiftung of the Bavarian Academy of Sciences and Humanities in recognition of his pioneering research on solid state quantum systems as the basis for future quantum information systems.

In November 2014, also Dr. Frank Deppe of WMI submitted his habilitation thesis entitled ***Microwave Quantum Science with Superconducting Circuits***. He started the habilitation process in October 2010 with R. Gross (TUM), E. Solano (Universidad del País Vasco, Bilbao) and J. Finley (TUM) acting as his mentoring team. The habilitation thesis presently is reviewed by the mentoring team and international experts. We are looking forward to a successful completion of the habilitation procedure early in 2015.

Completed and Ongoing Ph.D. Theses

Completed Ph.D. Theses:

1. **Carrier and Lattice Dynamics in Systems with Charge and Spin Order**
   Hans-Martin Eiter, TU München, Juli 2014.

Hans-Martin Eiter is receiving his "Doktorhut" after his Ph.D. defense on 27 August 2014.

Ongoing Ph.D. Theses:

2. **Superconducting Flux Qubits with Tunable Gap**
   Manuel Schwarz, TU München, seit Juni 2009.
3. **All Optical Quantum Computing**
   Max Häberlein, TU München, seit Dezember 2009.
4. **Raman-Untersuchungen an stark korrelierten Systemen mit hoher Ortsauflösung**
   Florian Kretschmar, TU München, seit Januar 2010.
5. **Vibrational Investigations of Luminescence Molecules**
   Nitin Chelwani, TU München, seit September 2010.
6. **Time-Domain Measurements on Ultra-strong-coupled Qubit-Resonator Systems**
   Alexander Baust, TU München, seit Oktober 2010.
7. **Spinabhängige thermogalvanische Effekte in ferromagnetischen Dünnschichten**
   Johannes Lotze, TU München, seit April 2011.
8. **Generation and Detection of Quantum Correlations in Circuit QED Systems**
   Ling Zhong, TU München, seit November 2011.
9. **Superconducting Quantum Circuits for Qunatum Electrodynamics Experiments**
   Karl Friedrich Wulschner, TU München, seit Januar 2012.
10. **Circuit Quantum Electrodynamics Experiments with Tunable Flux Qubits**
    Jan Goetz, TU München, seit Januar 2012.
11. **Single Excitation Transfer in the Quantum Regime: A Spin-Based Solid State Approach**
    Christoph Zollitsch, TU München, seit Januar 2012.

12. **Untersuchung der verschiedenen Phasen eisenbasierter Supraleiter mittels Raman-Streuung**
    Andreas Baum, TU München, seit April 2012.
13. **Superconducting Properties of Organic Metals in the Vicinity of Ordering Instabilities**
    Michael Kunz, TU München, seit August 2012.
14. **Quantum Information Processing with Propagating Quantum Microwaves**
    Peter Eder, TU München, seit November 2012.
15. **Coupled Electro-Nanomechanical Systems**
    Matthias Pernpeintner, TU München, seit November 2012.
16. **Spin Transport in Ferrromagnetic Microsturctures**
    Michael Schreier, TU München, seit Dezember 2012.
17. **Spin Caloritronics in Ferromagnet/Normal Metal Hybrid Structures**
    Sybille Meyer, TU München, seit Dezember 2012.
18. **Spin dynamics and spin transport in solid state systems**
    Hannes Maier-Flaig, TU München, seit November 2013.
19. **A Comparative Study of the Phase Diagrams of CuO_2 and Fe-based Compounds**
    Thomas Böhm, TU München, seit Dezember 2013.
20. **Circuit Quantum Electrodynamics with Three-dimensional Cavities**
    Edwar Xie, TU München, seit Dezember 2013.

Completed and Ongoing Diploma, Bachelor, Master Theses

Completed Master and Diploma Theses:

1. **Magnetostriction in Nanomechanical Systems**
   Rasmus Holländer, TU München, März 2014.
2. **Spin Seebeck Effect Experiments**
   Niklas Roschewsky, Masterarbeit, TU München, März 2014
3. **High-field Normal State Magnetotransport Properties of Electron-doped Cuprate Superconductors**
   Vassilios Tzanos, Masterarbeit, TU München, Mai 2014.
4. **Magnetoelektrische Effekte in multifunktionalen Schichtstrukturen**
   Bastian Stibbe, Diplomarbeit, TU München, Mai 2014.
5. **Bestimmung thermischer Materialparameter von Dünnschichtsolarzellen**
   Valentin Kunkel, Masterarbeit, TU München, Juli 2014.
6. **Charakterisierung der modalen Eigenschaften einer Niederdruckturbinenbeschaufelung**
   Lukas Traußnig, Diplomarbeit, TU München, September 2014.
7. **Topologische Phasen in Iridaten mit Pyrochlorstruktur / Topological Phases in Pyrochlore Iridates**
   Andreas Wörfel, Masterarbeit, TU München, Oktober 2014.
8. **Experimental Study of Spin Currents in Compensated Rare Earth Garnets**
   Katrin Ganzhorn, Masterarbeit, TU München, Oktober 2014.
9. **Magnetotransportuntersuchung des antiferromagnetischen organischen Supraleiters κ-(BETS)$_2$FeBr$_4$ / Magnetotransport studies of the organic superconductor and antiferromagnet κ-(BETS)$_2$FeBr$_4$**
   Ludwig Schaidhammer, Masterarbeit, TU München, November 2014.
10. **Charakterisierung und Analyse von RF-SQUID-vermittelter, einstellbarer Resonatorkopplung / Characterisation and analysis of RF-SQUID mediated tunable resonator coupling**
    Fabian Kössel, Masterarbeit, TU München, November 2014.
11. **Charakterisierung von supraleitenden koplanaren Wellenleiter-Resonatoren bei Millikelvin-Temperaturen / Characterization of superconducting coplanar waveguide resonators at millikelvin temperatures**
    Philipp Summer, Masterarbeit, TU München, November 2014.
12. **Fabrikation und Charakterisierung eines elektro-nanomechanischen Hybrid-System / Fabrication and characterization of an electro-nanomechanical hybrid system**
    Anh Tu Bohn, Masterarbeit, TU München, November 2014:
13. **Kohärente Manipulation von Phospor-Donatorspins in Silizium bei tiefen Temperaturen / Coherent Manipulation of Phosphorus Donor Spins in Silicon at Low Temperatures**
    Kai Müller, Masterarbeit, TU München, November 2014.
14. **Photoleitfähigkeitsmessungen in Yttrium-Eisen-Granat-Dünnfilmen / Photoconductivity Measurements in Yttrium Iron Garnet Thin Films**
    Roland Rösslhuber, Masterarbeit, TU München, November 2014.
15. **Supraleitendes On-chip-Mikrowellen-Interferometer / On-chip Superconducting Microwave Interferometer**
    Michael Fischer, Masterarbeit, TU München, Dezember 2014.

16. **Supraleitender On-chip-Mikrowellen-Strahlteiler / On-chip Superconducting Microwave Beam Splitter**
Christian Schneider, Masterarbeit, TU München, Dezember 2014.
17. **Ketten von Resonatoren mit einstellbarer Nichtlinearität**
Udo Schaumburger, Diplomarbeit, TU München, Dezember 2014.

Completed Bachelor Theses:

18. **Abhängigkeit des Spin-Hall-Magnetwiderstandes von der magnetischen Grenzflächen-Momentdichte in Pt | $Y_3Fe_5O_{12}$-Bilagen / Dependence of the Spin Hall Magnetoresistance on the Interface Magnetic Moment Density in Pt | $Y_3Fe_5O_{12}$ Bilayers**
Tamara Aderneuer, Bachelorarbeit, TU München (2014).
19. **Die Bedeutung der Yosida-Funktion für die Zweiflüssigkeits-Beschreibung der Supraleitung**
Matthias Englbrecht, Bachelorarbeit, TU München (2014).
20. **Hochpräzise Phasenstabilisierung zwischen Mikrowellengeneratoren / High-precision phase stabilization between microwave generators**
Johanna Fischer, Bachelorarbeit, TU München (2014).
21. **Dünne Schichten für Spinstrom- und spinkalorische Experimente / Thin Film Fabrication for Spin Current and Spin Caloric Experiments**
Sascha Frölich, Bachelorarbeit, TU München (2014).
22. **Untersuchung von $CeTe_3$ mit Raman-Spektroskopie / Study of $CeTe_3$ using Raman spectroscopy**
Henrik Gabold, Bachelorarbeit, TU München (2014).
23. **Herstellung eines Breitband-Messstabs zur Untersuchung ferromagnetischer Resonanz / A Magnet Cryostat Dip Stick for Broadband Ferromagnetic Resonance Experiments**
Felix Hartz, Bachelorarbeit, TU München (2014).
24. **Herstellung dünner $Pr_2Ir_2O_7$-Schichten und ihre elektrischen Eigenschaften / Fabrication of $Pr_2Ir_2O_7$ thin films and their electrical properties**
Adrian Haussmann, Bachelorarbeit, TU München (2014).
25. **Hochauflösende Widerstandsmessungen / High Resolution Resistance Measurements**
Tobias Meier, Bachelorarbeit, TU München (2014).
26. **Verlustreduzierung von supraleitenden koplanaren Mikrowellenresonatoren auf Saphir-Substraten / Loss reduction of superconducting coplanar microwave resonators on sapphire substrates**
Sebastian Meier, Bachelorarbeit, TU München (2014).
27. **Dreidimensionale Hohlraumresonatoren für die Schaltkreis-Quantenelektrodynamik / 3D Cavities for Circuit Quantum Electrodynamics**
Jonathan Müller, Bachelorarbeit, TU München (2014).
28. **Spin-Pumpen und SMR-Rektifikation in Pt/YIG-Doppelschichten / Spin Pumping and SMR-Rectification in Pt/YIG-Bilayers**
Arthur Niedermayr, Bachelorarbeit, TU München (2014).
29. **Herstellung von Yttrium-Eisengranat-Dünnschichten via Sol-Gel-Prozess / Yttrium iron garnet (YIG) thin films via metal-organic deposition**
Magdalena Pühl, Bachelorarbeit, TU München (2014).
30. **Supraleitende Quantenschaltkreise: Mikrowellenresonatoren mit Antenne / Super-**

conducting quantum circuits: Microwave resonators with antenna
Korbinian Reiser, Bachelorarbeit, TU München (2014).

31. **Optische Interferometrie spinmechanischer Nanostrukturen**
Lisa Rosenzweig, Bachelorarbeit, TU München (2014).
32. **Untersuchungen zu magnetischen Winkelsensoren mit Hilfe von COMSOL Multiphysics / Analysis of Magnetic Angle Sensors using COMSOL Multiphysics**
Jonas Schenk, Bachelorarbeit, TU München (2014).
33. **Erweiterung einer Rundenzeitsimulationssoftware um ein Modul zur Kühlungssimulation / Extension of a lap time simulation software with a module to malinger cooling systems**
Bernhard Springer, Bachelorarbeit, TU München (2014).
34. **Spitzenverstärkte Raman-Streuung (TERS) / Tip-Enhanced Raman-Scattering (TERS)**
Maria Theodoridou, Bachelorarbeit, TU München (2014).

Ongoing Master and Diploma Theses:

35. **Coupling of Transmon Qubits and CPW Resonators for Circuit-QED Experiments**
Javier Puertas Martinez, Masterarbeit, TU München, seit Februar 2014.
36. **Three-dimensional Cavities for Circuit Quantum Electrodynamics**
Gustav Andersson, Masterarbeit, TU München, seit März 2014.
37. **Charakterisierung von Hochleistungspermanentmagneten für elektrische Antriebe**
Michael Tillinger, Diplomarbeit, TU München, seit März 2014.
38. **Spitzenverstärkte Raman-Spektroskopie / Tip-Enhanced Raman Spectroscopy**
David Hoch, Masterarbeit, TU München, seit April 2014.
39. **Untersuchung des magneto-strukturellen Phasenübergangs in FeAs-Verbindungen / Study of the Magneto-structural Phase Transition in FeAs Compounds**
Michael Rehm, Masterarbeit, TU München, seit April 2014.
40. **Elektromechanik in variierbaren Mikrowellenresonatoren / Electromechanics with tunable microwave resonators**
Philipp Schmidt, Masterarbeit, TU München, seit April 2014.
41. **Eight-Channel Microwave Receiver for Quantum Experiments**
Martin Betzenbichler, Masterarbeit, TU München, seit April 2014.
42. **Fabrication stability of Josephson junctions and superconducting flux qubits**
Lujun Wang, Masterarbeit, TU München, seit Mai 2014.
43. **Thin Film Fabrication for Spin Current and Spin Caloritronic Experiments**
Francesco Della Coletta, Masterarbeit, TU München, seit Mai 2014.
44. **Schaltkreis-Quantenelektrodynamik mit Gap-Tunable Qubits / Circuit-QED using gap-tunable qubits**
Miriam Müting, Masterarbeit, TU München, seit August 2014.
45. **Magneto-galvanische Messungen in magnetischen Hybridstrukturen / Magneto-galvanic measurements in magnetic hybrid structures**
Franz-Georg Kramer, Masterarbeit, TU München, seit August 2014.
46. **Charakterisierung eines JPA für Experimente mit propagierenden Quantemikrowellen / JPA Characterization for experiments with propagating quantum microwaves**
Stefan Pogorzalek, Masterarbeit, TU München, seit August 2014.
47. **Weiterentwicklung eines Schärfe-Messverfahrens für Kameras mit Fisheye-Objektiven**

Marc Schneider, TU München, seit Oktober 2014.

48. **Magnetic insulators for spin current and spin caloritronic experiments**
Michaela Lammel, Masterarbeit, TU München, seit Oktober 2014.

49. **Superconductivity versus Charge Density Wave in the Organic Metal α-(BEDT-TTF)$_2$TlHg(SCN)$_4$**
Luzia Höhlein, Masterarbeit, seit November 2014.

50. **Spin current transport in magnetic hybrids**
Richard Schlitz, Masterarbeit, TU München, seit Oktober 2014.

51. **Zirkularpolarisierte Mikrowellenkavitäten**
Sho Watanabe, Masterarbeit, TU München, seit Oktober 2014.

52. **Untersuchung von $BaFe_2As_2$ unter hydrostatischem Druck / Study of $BaFe_2As_2$ under hydrostatic pressure**
Andreas Walter, Masterarbeit, TU München, seit Oktober 2014.

Research Projects and Cooperations

A large number of our research projects are benefiting from the collaboration with external groups in joint research projects, as well as from individual collaborations, exchange programs and visitors. Most collaborations are based on joint projects, which are funded by different research organizations (see list below). A considerable number of collaborations also exists with universities, other research institutions and industry without direct financial support.

Funded Projects

A. German Research Foundation: Excellence Initiative

Cluster of Excellence "Nanosystems Initiative Munich"

1. Research Area I: *Quantum Nanophysics*
   F. Deppe, S.T.B. Gönnenwein, R. Gross, H. Huebl, A. Marx
2. Research Area II: *Hybrid Nanosystems*
   S.T.B. Gönnenwein, R. Gross, H. Huebl

B. German Research Foundation: Collaborative Research Centers

Collaborative Research Center 631: "Solid-State Quantum Information Processing: Physical Concepts and Materials Aspects"

1. Project A3: *Superconducting Quantum Circuits as Basic Elements for Quantum Information Processing*
   R. Gross, A. Marx
2. Project A8: *Cavity Quantum Electrodynamics with Superconducting Devices*
   A. Marx, R. Gross
3. Project C3: *Fundamentals of Quantum Logic Gates in Silicon*
   M. Brandt, H. Huebl, M. Stutzmann
4. Project S: *Coordination of the Collaborative Research Center*
   R. Gross

Transregional Collaborative Research Center TRR 80: "From Electronic Correlations to Functionality"

1. Project A2: *Spatially and Momentum Resolved Raman Studies of Correlated Systems*
   R. Hackl

C. German Research Foundation: Priority Programs

1. Spin-dependent thermo-galvanic effects: experiment
   within the DFG Priority Program 1538 *Spin-Caloric Transport – SpinCAT*
   S.T.B. Gönnenwein, R. Gross (Az. GO 944/4-1, GO 944/4-2)
2. Project: *Raman study of electron dynamics and phase transitions in iron-pnictide compounds*
   within the DFG Priority Program 1458 *"High-Temperature Superconductivity in Iron-Pnictides"*
   R. Hackl, R. Gross, B. Büchner, D. Johrendt, C. Honerkamp (Az. HA 2071/7-1, HA 2071/7-2)

3. Project: *Spin injection, spin transport and controllable ferromagnetism in transition metal doped ZnO*
   within the DFG Priority Program 1285 *"Halbleiter-Spinelektronik"*
   R. Gross, S.T.B. Gönnenwein, M. Opel (Az. GR 1132/14-1, GR 1132/14-2, GR 1132/14-3)

D. German Research Foundation: Research Projects

1. Project: *Exotic Superconductivity in Strongly Anisotropic Correlated Organic Metals in the Vicinity of Insulating Phases*
   M. Kartsovnik, W. Biberacher, R. Gross (Az. KA 1652/4-1)
2. Project: *Doping Dependent Evolution of the Fermi Surface and Competing Ordering Phenomena in Superconducting Cuprates*
   R. Gross, M. Kartsovnik, A. Erb (Az. GR 1132/15-1)
3. Project: *Interaction Between Spin, Lattice, and Charge in Non-Centrosymmetric Correlated Metals*
   R. Hackl, R. Gross (Az. HA 2071/5-1)

E. European Union

1. EU Collaborative Project (call identifier FP7-ICT-2011-C), project title *Quantum Propagating Microwaves in Strongly Coupled Environments – PROMISCE*
   F. Deppe, A. Marx, R. Gross, Grant Agreement no. 284566
   partners: several European Universities and research facilities.
2. Marie Curie Network for Initial Training (call identifier FP7-PEOPLE-2010-ITN), project title *Circuit and Cavity Quantum Electrodynamics (CCQED)*
   R. Gross, A. Marx, F. Deppe, Grant Agreement No. PITN-GA-2010-264666
   partners: several European Universities and research facilities.

F. Bavaria California Technology Center (BaCaTeC)

1. Project: *Nematic Order and New Phases in Quantum Materials*
   R. Hackl,
   partners: Profs. Thomas Devereaux, Steve Kivelson, and Sri Raghu (Stanford University)

G. German Academic Exchange Service

1. Project-based Personnel Exchange Programme (PPP) with Serbia (project 56267076: Fe-based superconductors), collaboration with the Institute of Physics, University of Belgrade (Dr. Z.V. Popovic).
   R. Hackl
2. Project-based Personnel Exchange Programme (PPP) with India (project 57085749: Spin Current Generation and Detection Using FMI/NM Hybrids), collaboration with the IIT Madras, Chennai (Prof. Dr. M. S. Ramachandra Rao).
   R. Gross

Conferences, Workshops, Public Outreach

The Walther-Meißner-Institute has organized/co-organized conferences, workshops and symposia in 2014. It also was participating in several public outreach events aiming at making science accessible to the public.

Highlights of Physics 2014 (27 September – 02 October 2014, Saarbrücken, Germany)

Walther-Meißner-Institute was participating in the annual festival "Highlights of Physics" at Saarbrücken, Germany. The this year's motto of the highlights was "Quantenwelten", bringing the topics quantum physics and quantum information technology into the focus of the public.

Several scientists of WMI (S. Geprägs, S.T.B. Gönnenwein, H. Hübl, J. Götz, M. Pernpeintner) were explaining phenomena related to macroscopic quantum effects such as superconductivity and suprafluidity over a whole week. In particular, they were demonstrating experiments on the Meißner effect as well as the fountain effect to the public.

6^{th} Ph.D. Student Workshop on Solid State Quantum Information Processing (06 – 10 October 2014, Glocknerhaus, Austria)

Due to the interdisciplinary character of the research field and the involvement of four universities, the stimulation of the direct exchange and interaction between the the Ph.D. students working in the different research projects of the Collaborative Research Center 631 (CRC 631) has been recognized as an important task from the beginning. Therefore, CRC 631 regularly organizes two- to three-day workshops for the Ph.D. students without their supervisors. The 6^{th} Ph.D. Student Workshop on Solid State Quantum Information Processing was organized by Hans Hübl of WMI, supported by the Ph.D. students Alexander Baust (WMI) and Stefan Lichtmannsecker (WSI). It was taking place at the Glocknerhaus located in the stunning scenery of the Hohe Tauern national park in Austria. This workshop particularly aimed at deepening cooperation amongst all Ph.D. students investigating quantum systems in the greater Munich area. Therefore, it was jointly organized

with the Research Area 1 on Quantum Nanophysics of the Excellence Cluster Nanosystems Initiative Munich (NIM).

The workshop topics ranged from quantum optics, circuit quantum electrodynamics with artificial atoms, semiconductor quantum systems, opto- and electromechanics to theoretical aspects of quantum information processing. It also was including tutorial talks providing a fundamental introduction into the topics of the main research directions of CRC 631 and NIM. In addition, the Ph.D. and master students from six universities and research institutions reported on the progress of the research work to their fellow students and discussed future directions of their work. The workshop turned out to be very fruitful for the interaction among the Ph.D. students and the mutual information both on their research work and practical problems. Moreover, due to the tutorial style of the presentations during the workshops, those Ph.D. students that had joined CRC 631 or NIM only recently were able to get a broad overview on the research activities going on within this coordinated research projects.

Course 3 on "Physics and Electronics in Everyday Life" of the Ferienakademie 2014 (September 21 – October 03, 2014, Sarntal, Italy)

The course was hold by Rudolf Gross of WMI together with Prof. Dr. Gert Denninger, University of Stuttgart, and Prof. Dr. Klaus Mecke, University of Erlangen-Nuremberg, within the *Ferienakademie*. The Ferienakademie is jointly organized by the Technical University of Munich, the University of Erlangen/Nuremberg, and the University of Stuttgart to motivate and foster highly talented students. It took place at Sarntal in the Italian Alps.

Workshop of the work unit "Intermetallic and Oxide Systems with Spin and Charge Interactions" within the German Association for Crystal Growth (23 – 24 October 2014, Research Campus Garching, Germany)

The 16^{th} meeting of the work unit *Intermetallic and Oxide Systems with Spin and Charge Interactions* of the Deutsche Gesellschaft für Kristallwachstum und Kristallzüchtung e.V. (DGKK) was jointly organized by C. Pfleiderer (Faculty of Physics, TUM) and A. Erb (WMI, BAdW), who presently also is spokesman of this work unit. With 16 scientific talks on various problems of crystal growth and characterization and with more than 40 participants from Germany and Austria, the workshop found an extraordinary resonance.

The workshop program was covering a wide variety of materials systems, which are subjects of current research programs mainly in university research. Particular subsessions were dedicated to oxide materials with $LaRuO_5$ showing spin-dimer transitions, flux growth of $BaCuSi_2O_6$, $PdCrO_2$ and $PdCoO_2$ delafossites, electron doped superconductors, detector crystals for dark matter research, and the use of Lithium containing solvents in flux growth for the crystallization of light and volatile compounds. The workshop program was also covering intermetallics such as silicates and Heusler compounds as well as diborates. A relatively new topic in the community were the iridates with their special problem related to the highly volatile Iridium oxide. The meeting offered a great opportunity to exchange knowledge and experience in various fields and techniques of crystal growth and to convey the experience of older colleagues especially to the younger researchers in the field.

Final Meeting of the EU Initial Training Network CCQED (29 – 31 October 2014, Aarhus University, Denmark)

In 2011, the european network ***Circuit and Cavity Quantum Electro-Dynamics (CCQED)*** has been granted 3.5 Million Euros by the European Union through a Marie Curie Action within the Seventh Framework Program Initial Training Network ITN-People-2010. The aim of CCQED was to bridge two communities in physics, in the academic and private sectors, to share, pursue and diffuse within Europe the benefits of collaborations in the science of elementary quanta. CCQED involves 10 research centres and 3 companies, representing the cutting edge of research in the quantum electrodynamics of fundamental systems in Europe. The network trains 12 early stage researchers (Ph.D. students) and 2 experienced researchers (postdocs).

CCQED had its final meeting organized in the form of a conference from 29–31 October 2014 at Aarhus University in Denmark. In addition to the CCQED speakers reviewing the scientific progress within the network, prominent external speakers were invited. They gave insight into spin ensembles in cavity fields (A. Briggs, Oxford University, UK), quantum dots in photonic crystals (P. Lodahl, University of Copenhagen, Denmark), Rydberg atoms in optical cavities (P. Grangier, Institute d'Optique, France), circuit QED systems (B. Huard, École Normale Supérieure, France), and ensembles of cold atoms in cavities (D. Stamper-Kurn, Berkeley University, USA). Further details can be found under www.ccqed.eu/conferences/final-meeting-in-aarhus/.

NanoDay 2014
(22 November 2014, German Science Museum, Munich, Germany)

The NanoDay was organized by the Excellence Cluster Nanosystems Initiative Munich (NIM) to inform the public on nanoscience in general and the research activities of NIM in particular. At the information booths the visitors were able to do a lot of nano-experiments by themselves and in the stage program professors were explaining their cutting edge research projects. The program was completed by the comedian Georg Eggers who presented science with a twinkle in his eye.

The NanoDay was a great success with an unexpectedly large number of visitors. Rudolf Gross of WMI was contributing to the lecture program with a talk on "Die verrückte Welt der Quantenphysik" and Hans Hübl and his team of Ph.D. and master students were presenting a life experiment, were visitors could play and watch the motion of a nano-guitar (see picture) by a laser interferometer.

Public outreach events such as the NanoDay or the annual "Tag der Offenen Tür" (not mentioned in our report) are causing a considerable extra-workload to the involved scientists. However, they considered important and necessary to communicate the scientific work of the Bavarian Academy of Sciences and Humanities to the general public.

Cooperations

Other collaborations without direct project funding involve:

- Stanford University, Stanford, USA (T.P. Devereaux, M. Greven, Z.-X. Shen, I. Fisher, B. Moritz)
- Universidad del País Vasco and Ikerbasque Foundation, Bilbao, Spain (E. Solano)
- Instituto de Física Fundamental, CSIC, Madrid, Spain (J.J. Garcia-Ripoll)
- Central Research Institute of the Electric Power Industry, Tokyo, Japan (Dr. S. Ono, Dr. Y. Ando)
- Green Innovation Research Laboratories, NEC Corporation, Japan (Y. Nakamura, J.S. Tsai, K. Inomata, T. Yamamoto)
- University of Tohoku, Sendai, Japan (Gerrit E.W. Bauer, Eiji Saitoh)
- European Synchrotron Radiation Facility (ESRF), Grenoble (H. Müller, F. Wilhelm, K. Ollefs)
- Lund University, Lund, Sweden (D. Mannix)
- Materials Science Research Centre, IIT Madras, India (M.S. Ramachandra Rao)
- Raja Ramanna Centre for Advanced Technology, Indore, India (Lalit M. Kukreja)
- ETH-Zurich, Switzerland (A. Wallraff, L. Degiorgi, R. Monnier, Dr. M. Lavagnini)
- Chalmers University of Technology Gothenburg, Sweden (P. Delsing, G. Wendin)
- University of Alabama, MINT Center, Tuscaloosa, USA (A. Gupta)
- Helsinki University of Technology, Materials Physics Laboratory, Finland (T. Heikkilä)
- Delft University of Technology, Kavli Institute of NanoScience, Delft, The Netherlands (T.M. Klapwijk, G.E.W. Bauer)
- B. Verkin Institute for Low Temperature Research and Engineering, Kharkov, Ukraine (V.G. Peschansky)
- Landau Institute for Theoretical Physics, Chernogolovka, Russia (P. Grigoriev)
- University of Oxford, Clarendon Laboratory, England (A. Karenowska)
- Russian Academy of Sciences, Chernogolovka, Russia (N. Kushch, A. Palnichenko)
- High Magnetic Field Laboratory, Dresden (E. Kampert, J. Wosnitza)
- High-Magnetic-Field Laboratory, Grenoble, France (I. Sheikin)
- High Magnetic Field Laboratory, Toulouse (C. Proust, D. Vignolles)
- National High Magnetic Field Laboratory, Tallahassee, USA (J. Brooks)
- IFW Dresden, Germany (B. Büchner, J. Fink, S.V. Borisenko, M. Knupfer)
- Max-Planck-Institut für Festkörperforschung, Stuttgart (B. Keimer, L. Boeri)
- University of Tübingen, Germany (R. Kleiner, D. Kölle)
- University of Würzburg, Germany (W. Hanke, F. Assaad, C. Honerkamp, M. Potthoff)
- University of Augsburg, Germany (P. Hänggi, A. Wixforth, A. Kampf, A. Loidl, J. Deisenhofer, V. Tsurkan)
- University of Hamburg, Germany (G. Meier, W. Wurth)
- University of Leipzig, Germany (J. Haase)
- University of Ulm, Abt. Halbleiterphysik, Germany (W. Limmer)
- RWTH Aachen, Germany (G. Güntherodt, B. Beschoten)
- Ernst-Moritz-Arndt Universität Greifswald, Germany (Markus Münzenberg)
- Martin-Luther-Universität Halle, Germany (Georg Woltersdorf)

- Universität Regensburg, Institut für Experimentelle und Angewandte Physik, Germany (Christian Back)
- Universität Bielefeld, Germany (G. Reiss, A. Thomas, T. Kuschel)
- University of British Columbia, Vancouver, Canada (D. Bonn, A. Damascelli)
- TU München, Physics Department, Germany (D. Grundler, Ch. Pfleiderer, F.C. Simmel, Jean Come Lanfranchi, P. Müller-Buschbaum)
- TU München, Walter Schottky Institut, Germany (G. Abstreiter, M. Stutzmann, J. Finley, M. Brandt, A. Holleitner)
- TU München, Lehrstuhl für Technische Elektronik (M. Becherer)
- LMU München, Physics Department, Germany (J.P. Kotthaus, J. von Delft, E. Frey, J. Rädler, S. Ludwig)
- LMU München, Chemistry Department, Germany (Hubert Ebert, Diemo Ködderitzsch)
- Universidad de Zaragoza, Departamento de Fisica de la Materia Condensada, Spain (L. Morellon, J.M. de Teresa, D. Zueco)
- EPFL Lausanne, Switzerland (T. Kippenberg, H. Ronnov)
- University of New South Wales, Sydney, Australia (M. Simmons, A. Morello)
- McMaster University, Hamilton, Canada (J.P. Carbotte)
- Technische Universität Graz, Austria (E. Schachinger)
- Universität Konstanz (A. Leitenstorfer, E. Weig, J. Demsar, A. Pashkin)
- BMW Group, Munich, Germany (J. Schnagl, W. Stadlbauer, G. Steinhoff)
- Siemens AG, CT MM 2, Munich, Germany (R. Matz, W. Metzger)
- Attocube, Munich, Germany (K. Karrai, D. Andres, E. Hoffmann)
- THEVA Dünnschichttechnik, Ismaning, Germany (W. Prusseit)
- Johannes-Kepler-Universität Linz, Institut für Halbleiter- und Festkörperphysik, Austria (A. Ney)
- Jülich Centre for Neutron Science JCNS, Garching, Germany (S. Pütter)
- Université de Toulouse, Laboratoire de Physique Théorique, Toulouse, France (R. Ramazashvili)
- Lawrence Berkeley National Laboratory, Berkeley, USA (A. F. Kemper)
- University of Belgrade, Belgrade, Serbia (Z. Popovic, N. Lazarevic, D. Tanaskovic)
- University of Aveiro, Portugal (N. A. Sobolev)
- Macquarie University, MQ Research Centre for Quantum Science and Technology, Australia (J. Twamley)
- Instituto de Ciencia de Materiales de Sevilla, Spain (J. Poyato, J.L. Perez-Rodriguez)
- Hungarian Academy of Sciences, Research Institute for Solid State Physics and Optics, Budapest, Hungary (K. Kamaras, I. Tüttö, J. Balogh)
- University of Rome "La Sapienza", Rome, Italy (S. Caprara, C. Di Castro, M. Grilli)
- Hungarian Academy of Sciences, Budapest University of Technology and Economics, Budapest, Hungary (A. Virosztek, A. Zawadowski, G. Mihály)

Stays abroad

Extended visits of members of the Walther-Meißner-Institute at foreign research laboratories:

1. **Rudi Hackl**
   Stanford University and Stanford Institute for Materials and Energy Science, Stanford, USA
   29. 04. - 05. 05. 2014, 01. 09. - 27. 11. 2014
2. **Rudi Hackl**
   Institute of Physics, University of Belgrade, Belgrade, Serbia
   17. 07. - 23. 07. 2014, 17. 12. - 21. 12. 2014
3. **Mark Kartsovnik**
   High Magnetic Field Laboratory, Grenoble, France
   08. 04. - 14. 04. 2014, 24. 06. - 02. 07. 2014, 03. 11. - 12. 11. 2014
4. **Matthias Opel, Francesco Della Coletta**
   European Synchrotron Radiation Facility (ESRF), Grenoble, France
   29. 08. - 09. 09. 2014
5. **Matthias Opel**
   Materials and Structures Laboratory, Tokyo Institute of Technology, Yokohama, Japan
   23. 06. - 24. 06. 2014
6. **Edwin Menzel**
   Instituto de Fisica Fundamental, IFF-CSIC, Madrid, Spain
   26. 04. - 04. 05. 2014
7. **Edwin Menzel**
   University of the Basque Country UPV/EHU, Bilbao, Spain
   05. 05. - 10. 05. 2014
8. **Kirill Fedorov**
   University of the Basque Country UPV/EHU, Bilbao, Spain
   21. 09. - 26. 09. 2014

Conference Talks and Seminar Lectures

Alexander Baust

1. **Tunable and switchable coupling between two superconducting resonators**
   6^{th} Ph.D. Student Workshop on Solid-State Quantum Information Processing, Glocknerhaus, Heiligenblut, Austria
   06. - 10. 10. 2014

Frank Deppe

1. **Tunable coupling between two superconducting resonators**
   Seminar Talk, Institut Neél, Grenoble, France
   28. 01. 2014
2. **Tunability in superconducting flux quantum circuits**
   Seminar Talk, The University of Tokyo, Tokyo, Japan
   20. 10. 2014
3. **Ultrastrong light-matter coupling in circuit quantum**
   Invited Talk, Workshop on "Mathematics and Physics of Interacting Quantum Systems (MPIQS)", Japan
   24. 10. 2014
4. **Tunable and switchable coupling between two superconducting resonators**
   Invited Talk, CCQED Final Meeting, Aarhus University, Denmark
   30. 10. 2014

Stephan Geprägs

1. **Spin Hall magnetoresistance in ferromagnetic insulator/normal metal hybrids**
   IEEE International Magnetics Conference, Dresden, Germany
   04. - 08. 05. 2014
2. **Absence of an induced magnetic moment in Pt on $Y_3Fe_5O_{12}$ (YIG)**
   IEEE International Magnetics Conference, Dresden, Germany
   04. - 08. 05. 2014
3. **Pyrochlore Iridates: Possible Candidates for the Realization of Weyl Nodes**
   Workshop on "Strongly Correlated Electron Systems (SCES 2014)", Grenoble, France
   07. - 11. 07. 2014

Sebastian Gönnenwein

1. **Spin Current Transport Across Interfaces**
   Invited Talk, 550. Wilhelm und Else Heraeus Seminar, "Spin Transport Beyond Boltzmann", Bad Honnef, Germany
   09. 01. 2014
2. **Spin Currents in Ferromagnet/Normal Metal Hybrid Structures**
   Physik-Seminar des 2. Physikalischen Instituts, Universität zu Köln, Germany
   22. 01. 2014
3. **Spin Currents in YIG/Pt Hybrid Structures**
   Invited Talk, 14^{th} Reimei Workshop on "Spin Currents and Related Phenomena", Institut Laue Langevin, Grenoble, France
   11. 02. 2014
4. **Spin Currents in Ferromagnet/Normal Metal Hybrid Structures**
   Physik-Seminar, Johannes Gutenberg Universität Mainz, Germany
   30. 04. 2014
5. **Spin Mechanics and Spin Currents in Hybrid Heterostructures**
   Invited Talk, International Conference on "Spin Mechanics II", Tohoku University, Sendai, Japan
   22. 06. 2014
6. **From Spin Pumping to Spin Hall Magnetoresistance**
   Invited Talk, Spin Caloritronics Summer School, Kloster Irsee, Germany
   14. 07. 2014

7. **Experimental Observation of the Spin Nernst Effect**
   Invited Talk, International Conference "Spin Caloritronics VI", Kloster Irsee, Germany
   16. 07. 2014
8. **Spin Currents in Ferromagnet/Normal Metal Heterostructures**
   Invited Talk, 575. Wilhelm und Else Heraeus Seminar on "Functional Metalorganics and Hybrids", Bad Honnef, Germany
   18. 11. 2014
9. **Spin Currents in Ferromagnet/Normal Metal Heterostructures**
   Physik-Kolloquium der Universität Kaiserslautern, Germany
   24. 11. 2014
10. **Spin Currents in Ferromagnet/Normal Metal Heterostructures**
    Physik-Seminar der Universität Stuttgart, Germany
    08. 12. 2014

Jan Goetz

1. **From superconducting circuits to artificial atoms: An introduction to Josephson junction based qubits**
   6^{th} Ph.D. Student Workshop on Solid-State Quantum Information Processing, Glocknerhaus, Heiligenblut, Austria
   06. - 10. 10. 2014

Rudolf Gross

1. **Superconducting Hybrid Quantum Systems**
   R. Gross
   Physikalisches Kolloquium, Universität Mainz, Germany.
   14. 01. 2014
2. **Spin Currents and Quantum Spin Physics**
   R. Gross
   Physikalisches Kolloquium, Universität Regensburg, Germany.
   20. 01. 2014
3. **Superconducting Hybrid Quantum Circuits**
   R. Gross
   Invited Talk, 553. WE-Heraeus-Seminar on "Discrete and Analogue Quantum Simulators", Bad Honnef, Germany.
   10 – 12 February 2014.
4. **Exploring the Quantum with Solid State Systems**
   R. Gross
   Invited Tutorial, ICC-IMR/20^{th} REIMEI International Workshop "Spin Mechanics 2", Sendai, Japan.
   21 – 24 June 2014
5. **Spin Hall Magnetoresistance and Magnetoimpedance**
   R. Gross
   Invited Talk, 13^{th} Bilateral German-Japanese Symposium on "Interplay of Charge and Orbital Degrees of Freedom in Strongly Correlated Electron Systems", Schloss Ringberg, Germany.
   13 – 16 July 2014
6. **Solid State Circuits are Going Quantum**
   R. Gross
   Tutorial, Ferienakademie der TU München, Universität Erlangen-Nürnberg und der Universität Stuttgart, Sarntal, Italy.
   21 September – 03 October 2014
7. **Superconducting Hybrid Quantum Systems**
   R. Gross
   Physikalisches Kolloquium, Universität Heidelberg, Germany.
   17. 10. 2014
8. **Verrückte Welt der Quantenphysik**
   R. Gross

Invited Talk, "NanoDay – Tag der Nanowissenschaften", Deutsches Museum, Munich, Germany.
22 November 2014

Rudolf Hackl

1. **Phase transition in Fe-based compounds**
   Plenary lecture at the International Workshop "Novel Materials and Superconductors", Obertraun, Austria.
   14. 02. 2014
2. **Raman scattering in FeAs superconductors**
   Kick-off meeting for the second funding period of the DFG Priority Program SPP 1458 Dresden, Germany.
   27. 03. 2014
3. **A light scattering study of the pairing potential in Fe-based SC and related compounds**
   Invited Talk at the "International Conference Low-Energy Electron Dynamics in Solids (LEES 2014)", Amboise, France.
   04. 07. 2014
4. **Phase transitions in Fe-based compounds**
   Seminar Talk, Geballe Laboratory for Advanced Materials and Stanford Institute for Materials and Energy Sciences (SIMES), Stanford University and SLAC National Accelerator Laboratory, Menlo Park, USA.
   21. 10. 2014
5. **CDW order RTe_3**
   Seminar Talk, Geballe Laboratory for Advanced Materials and Stanford Institute for Materials and Energy Science (SIMES), Stanford University and SLAC National Accelerator Laboratory, Menlo Park, USA.
   28. 10. 2014

Hans Hübl

1. **Nano-Opto-Mechanics at Microwave Frequencies**
   Lecture Series "Methods in Materials Science", Graduiertenschule Mainz, Universität Mainz, Germany.
   21. 05. 2014
2. **Nano-Opto-Mechanics at Microwave Frequencies**
   Institutsseminar, Universität Konstanz, Germany.
   26. 05. 2014
3. **Nano-Opto-Mechanics at Microwave Frequencies**
   Seminar Talk, Tokio University, Japan.
   26. 06. 2014
4. **Gekoppelte harmonische Oszillatoren: Saiten, Spins und Mikrowellenresonatoren**
   Seminar Talk, Universität Karlsruhe, Germany.
   17. 07. 2014
5. **Nano-Opto-Mechanics at Microwave Frequencies**
   Physik-Seminar, University of Basel, Switzerland.
   26. 10. 2014
6. **Spins, Springs, and superconducting resonators: coupling harmonic oscillators in the solid state**
   Seminar Talk, Universität Stuttgart, Germany.
   09. 12. 2014
7. **Nano-Opto-Mechanics at Microwave Frequencies**
   Quantum Optics Colloquium, Niels Bohr Institute, University of Copenhagen, Dänemark.
   12. 12. 2014

Mark Kartsovnik

1. **High-Field Magnetotransport Studies of the Fermi Surface in the Electron-Doped Cuprate $Nd_{2-x}Ce_xCuO_4$**
   Invited Talk, International School of Solid State Physics on "Multi-condensates superconductiv-

ity", Erice, Italy.
19. - 25. 07. 2014

Florian Kretzschmar

1. **Raman Study of SDW order and band-folding in twin-free $BaFe_2As_2$**
Spring Meeting of the German Physical Society, Dresden, Germany.
02. 04. 2014

Edwin Menzel

1. **Squeezing with a flux-driven Josephson parametric amplifier**
APS March Meeting, Denver, USA.
03. - 07. 03. 2014
2. **Propagating quantum microwave: Dual-path state reconstruction and path entanglement Quantum Nanoelectronics**
Seminar Talk, University of California, Berkeley, USA.
11. 03. 2014
3. **Propagating Quantum Microwaves**
Invited Talk, Seminar of the QUINFOG, Instituto de Fisica Fundamental, Madrid, Spain.
28. 04. 2014
4. **On-chip elements for all-optical quantum computation with propagating microwaves**
Invited Talk, Seminar of the QUTIS Group, Universidad des País Vasco, Bilbao, Spain
06. 05. 2014

Matthias Opel

1. **Zinc Oxide – From Dilute Magnetic Doping to Spin Transport**
Invited Talk, Workshop on "Functional Materials for Electronics", European Synchrotron Radiation Facility (ESRF), Grenoble, France.
03. - 05. 02. 2014
2. **Origin of the Magnetoresistance (MR) in Pt on $Y_3Fe_5O_{12}$ (YIG)**
Materials and Structures Laboratory, Tokyo Institute of Technology, Tokyo, Japan.
23. 06. 2014
3. **Magnetoelectric and Magnetoelastic Effects in BaTiO3-Based Multiferroic Hybrid Structures**
Invited Talk, 8^{th} International Conference on the Science and Technology for Advanced Ceramics (STAC-8), Yokohama, Japan.
25. - 27. 06. 2014

Kurt Uhlig

1. **Dry Dilution Refrigerator for Experiments on Quantum Effects in the Microwave Regime**
18^{th} International Cryocooler Conference (ICC 18), Syracuse, New York, USA.
09. - 12. 06. 2014

Friedrich Wulschner

1. **Tunable coupling between two superconducting microwave resonators**
Spring Meeting of the German Physical Society, Dresden, Germany.
31. 03. 2014
2. **Tunable coupling between two superconducting microwave resonators**
Kryoelektronische Bauelemente 2014, Berlin, Germany.
22. 09. 2014
3. **Tunable coupling between two superconducting microwave resonators**
6^{th} Ph.D. Student Workshop on Solid-State Quantum Information Processing, Glocknerhaus, Heiligenblut, Austria.
08. 10. 2014

Edwar Xie

1. **3D circuit QED with superconducting qubits**
NIM Summer Retreat, Kreuth, Germany.

Appointments, Membership in Advisory Boards, etc.

1. **Werner Biberacher** is member of the Scientific Council of the High Magnetic Field Laboratory (LNCMI) Grenoble/Toulouse, France.
2. **Frank Deppe** is associate member of the Cluster of Excellence *Nanosystems Initiative Munich (NIM)*.
3. **Dietrich Einzel** is one of the four spokesmen of the scientific staff of the Bavarian Academy of Sciences and Humanities.
4. **Andreas Erb** is spokesmen of the "Arbeitskreis Intermetallische und oxydische Systeme mit Spin- und Ladungskorrelationen" of the *Deutsche Gesellschaft für Kristallzüchtung und Kristallwachstum (DGKK)*.
5. **Sebastian Gönnenwein** is member and principal investigator of the Cluster of Excellence *Nanosystems Initiative Munich (NIM)*.
6. **Rudolf Gross** is member of the International Advisory Committee of the International Conference M_2S HTSC 2015, Geneva, Switzerland.
7. **Rudolf Gross** is member of the Scientific Advisory Board of the Leibniz Institute for Solid-State and Materials Research, Dresden.
8. **Rudolf Gross** is member of the selection committee of the Stern-Gerlach-Medal of the German Physical Society.
9. **Rudolf Gross** is deputy spokesman of the division of *Low Temperature Physics* of the Condensed Matter Section of the German Physical Society.
10. **Rudolf Gross** is spokesman of the Collaborative Research Center 631 on *Solid State Quantum Information Processing* of the German Research Foundation.
11. **Rudolf Gross** is member of the Executive Board of the Cluster of Excellence *Nanosystems Initiative Munich (NIM)* and coordinator of the Research Area 1 on *Quantum Nanosystems*.
12. **Rudolf Gross** is member of the Appointment and Tenure Board of Technical University of Munich.
13. **Rudolf Hackl** is deputy coordinator of the DFG Priority Program SPP 1458 on "High Temperature Superconductivity in the Iron Pnictides".
14. **Rudolf Hackl** is member of the evaluation board of the neutron source Heinz Maier-Leibnitz (FRM II).
15. **Hans Hübl** is member and principal investigator of the Cluster of Excellence *Nanosystems Initiative Munich (NIM)*.
16. **Mark Kartsovnik** is member of the Selection Committee of EMFL (European Magnetic Field Laboratories)
17. **Mark Kartsovnik** is member of the International Advisory Committee of the 10^{th} International Symposium on Crystalline Organic Metals Superconductors and Ferromagnets (ISCOM 2015)

Lectures, Seminars, Courses and other Scientific Activities

Several members of the Walther-Meißner-Institute give lectures and seminars at the Technical University of Munich.

Lectures

Frank Deppe

WS 2013/2014	• Seminar: Supraleitende Quantenschaltkreise (Seminar on Superconducting Quantum Circuits, with R. Gross, A. Marx)
SS 2014	• Angewandte Supraleitung: Josephson Effekte, supraleitende Elektronik und supraleitende Quantenschaltkreise (Applied Superconductivity: Josephson Effects, Superconducting Electronics and Superconducting Quantum Circuits, with R. Gross) • Seminar: Supraleitende Quantenschaltkreise (Seminar on Superconducting Quantum Circuits, with R. Gross, A. Marx)
WS 2014/2015	• Seminar: Supraleitende Quantenschaltkreise Seminar on Superconducting Quantum Circuits, with R. Gross, A. Marx)

Dietrich Einzel

WS 2013/2014	• Mathematische Methoden der Physik I (Mathematical Methods of Physics I) • Übungen zu Mathematische Methoden der Physik I (Mathematical Methods of Physics I, Problem Sessions) • WMI-Seminar über aktuelle Fragen der Tieftemperatur-Festkörperphysik (WMI Seminar on Current Topics of Low Temperature Solid-State Physics, with R. Gross, S.B.T. Gönnenwein, R. Hackl, H. Hübl, A. Marx, M. Opel) • Seminar: Advances in Solid-State Physics (with R. Gross, S.T.B. Gönnenwein, H. Hübl, A. Marx, M. Opel)
SS 2014	• Mathematische Methoden der Physik II (Mathematical Methods of Physics II) • Übungen zu Mathematische Methoden der Physik II (Mathematical Methods of Physics II, Problem Sessions) • WMI-Seminar über aktuelle Fragen der Tieftemperatur-Festkörperphysik (WMI Seminar on Current Topics of Low Temperature Solid-State Physics, with R. Gross, S.B.T. Gönnenwein, R. Hackl, H. Hübl, A. Marx, M. Opel) • Seminar: Advances in Solid-State Physics (with R. Gross, S.T.B. Gönnenwein, H. Hübl, M. Opel, A. Marx)
WS 2014/2015	• Mathematische Methoden der Physik I (Mathematical Methods of Physics I) • Übungen zu Mathematische Methoden der Physik I (Mathematical Methods of Physics I, Problem Sessions) • WMI-Seminar über aktuelle Fragen der Tieftemperatur-Festkörperphysik (WMI Seminar on Current Topics of Low Temperature Solid-State Physics, with R. Gross, S.B.T. Gönnenwein, R. Hackl, H. Hübl, A. Marx, M. Opel) • Seminar: Advances in Solid-State Physics (with R. Gross, S.T.B. Gönnenwein, H. Hübl, A. Marx, M. Opel,)

Rudolf Gross

WS 2013/2014	• Physik der Kondensierten Materie I (Condensed Matter Physics I) • Übungen zu Physik der Kondensierten Materie I (Condensed Matter Physics I, Problem Sessions, with S. Geprägs) • WMI-Seminar über aktuelle Fragen der Tieftemperatur-Festkörperphysik (WMI Seminar on Current Topics of Low Temperature Solid-State Physics, with D. Einzel, S.T.B. Gönnenwein, R. Hackl, H. Hübl, A. Marx, M. Opel)

- Seminar: Advances in Solid-State Physics (with D. Einzel, S.T.B. Gönnenwein, H. Hübl, A. Marx, M. Opel)
- Seminar: Superconducting Quantum Circuits (with F. Deppe, A. Marx)
- Festkörperkolloquium (Colloquium on Solid-State Physics, with D. Einzel)

SS 2014
- Physik der Kondensierten Materie II (Condensed Matter Physics II)
- Übungen zu Physik der Kondensierten Materie II (Condensed Matter Physics II, Problem Sessions, with S. Geprägs)
- Angewandte Supraleitung: Josephson Effekte, supraleitende Elektronik und supraleitende Quantenschaltkreise (Applied Superconductivity: Josephson Effects, Superconducting Electronics and Superconducting Quantum Circuits, with F. Deppe)
- Übungen zu Angewandte Supraleitung: Josephson Effekte, supraleitende Elektronik und supraleitende Quantenschaltkreise (Applied Superconductivity: Josephson Effects, Superconducting Electronics and Superconducting Quantum Circuits, Problem Sessions, with F. Deppe)
- Seminar: Advances in Solid-State Physics (with D. Einzel, S.T.B. Gönnenwein, H. Hübl, A. Marx, M. Opel)
- WMI-Seminar über aktuelle Fragen der Tieftemperatur-Festkörperphysik (WMI Seminar on Current Topics of Low Temperature Solid-State Physics, with D. Einzel, S.T.B. Gönnenwein, R. Hackl, H. Hübl, A. Marx, M. Opel)
- Seminar: Superconducting Quantum Circuits (with F. Deppe, A. Marx)
- Festkörperkolloquium (Colloquium on Solid-State Physics, with D. Einzel)
- Ferienakademie: Kurs 3 “Physik und Elektronik im Alltag” (Ferienakademie: Course 3 “Physics and Electronics in Everyday Life”)

WS 2014/2015
- Superconductivity and Low Temperature Physics I
- Exercises to Superconductivity and Low Temperature Physics I
- WMI-Seminar über aktuelle Fragen der Tieftemperatur-Festkörperphysik (WMI Seminar on Current Topics of Low Temperature Solid-State Physics, with D. Einzel, S.T.B. Gönnenwein, R. Hackl, H. Hübl, A. Marx, M. Opel)
- Seminar: Advances in Solid-State Physics (with D. Einzel, S.T.B. Gönnenwein, H. Hübl, A. Marx, M. Opel)
- Seminar: Superconducting Quantum Circuits (with F. Deppe, A. Marx)
- Festkörperkolloquium (Colloquium on Solid-State Physics, with D. Einzel)

Sebastian T.B. Gönnenwein

WS 2013/2014
- Seminar: Advances in Solid-State Physics (with D. Einzel, R. Gross, H. Hübl, A. Marx, M. Opel)
- Magnetismus (Magnetism)
- Übungen zu Magnetismus (Magnetism, Problem Sessions)
- WMI-Seminar über aktuelle Fragen der Tieftemperatur-Festkörperphysik (WMI Seminar on Current Topics of Low Temperature Solid State Physics, with D. Einzel, R. Gross, R. Hackl, H. Hübl, A. Marx, M. Opel)
- Seminar zu aktuellen Fragen der Magneto- und Spinelektronik (Seminar on Current Topics in Magneto and Spin Electronics, with M. Brandt, H. Hübl)

SS 2014
- Spin Electronics
- Übungen zu Spin Electronics (Exercises to Spin Electronics)
- Seminar: Advances in Solid-State Physics (with D. Einzel, R. Gross, H. Hübl, A. Marx, M. Opel)
- WMI-Seminar über aktuelle Fragen der Tieftemperatur-Festkörperphysik (WMI Seminar on Current Topics of Low Temperature Solid State Physics, with D. Einzel, R. Gross, R. Hackl, H. Hübl, A. Marx, M. Opel)
- Seminar zu aktuellen Fragen der Magneto- und Spinelektronik (Seminar on Current Topics in Magneto and Spin Electronics, with M. Brandt, H. Hübl)

WS 2014/2015
- Physik der Kondensierten Materie I (Condensed Matter Physics I)
- Übungen zu Physik der Kondensierten Materie I (Condensed Matter Physics I, Problem Sessions, with S. Geprägs)

- Seminar: Advances in Solid-State Physics (with D. Einzel, R. Gross, H. Hübl, A. Marx, M. Opel)
- WMI-Seminar über aktuelle Fragen der Tieftemperatur-Festkörperphysik (WMI Seminar on Current Topics of Low Temperature Solid State Physics, with D. Einzel, R. Gross, R. Hackl, H. Hübl, A. Marx, M. Opel)
- Seminar zu aktuellen Fragen der Magneto- und Spinelektronik (Seminar on Current Topics in Magneto and Spin Electronics, with M. Brandt, H. Hübl)

Rudi Hackl

WS 2013/2014
- WMI-Seminar über aktuelle Fragen der Tieftemperatur-Festkörperphysik (WMI Seminar on Current Topics of Low Temperature Solid-State Physics, with D. Einzel, R. Gross, S.B.T. Gönnenwein, H. Hübl, A. Marx, M. Opel)

SS 2014
- Supraleitung und Tieftemperaturphysik II (Superconductivity and Low Temperature Physics II)
- Übungen zu Supraleitung und Tieftemperaturphysik II (Superconductivity and Low Temperature Physics II, Problem Sessions)
- WMI-Seminar über aktuelle Fragen der Tieftemperatur-Festkörperphysik (WMI Seminar on Current Topics of Low Temperature Solid-State Physics, with D. Einzel, R. Gross, S.B.T. Gönnenwein, H. Hübl, A. Marx, M. Opel)

Hans Hübl

WS 2013/2014
- Seminar: Spin Caloritronics and Spin Pumping
- Seminar: Advances in Solid-State Physics (with D. Einzel, R. Gross, S.T.B. Gönnenwein, A. Marx, M. Opel)
- WMI-Seminar über aktuelle Fragen der Tieftemperatur-Festkörperphysik (WMI Seminar on Current Topics of Low Temperature Solid State Physics, with D. Einzel, R. Gross, S.T.B. Gönnenwein, R. Hackl, A. Marx, M. Opel)
- Seminar zu aktuellen Fragen der Magneto- und Spinelektronik (Seminar on Current Topics in Magneto and Spin Electronics, with S.T.B. Gönnenwein, M. S. Brandt)

SS 2014
- Seminar: Spin Caloritronics and Spin Pumping
- Seminar: Advances in Solid-State Physics (with D. Einzel, R. Gross, S.T.B. Gönnenwein, A. Marx, M. Opel)
- WMI-Seminar über aktuelle Fragen der Tieftemperatur-Festkörperphysik (WMI Seminar on Current Topics of Low Temperature Solid State Physics, with D. Einzel, R. Gross, S.T.B. Gönnenwein, R. Hackl, A. Marx, M. Opel)
- Seminar zu aktuellen Fragen der Magneto- und Spinelektronik (Seminar on Current Topics in Magneto and Spin Electronics, with S.T.B. Gönnenwein, M. S. Brandt)

WS 2014/2015
- Magnetismus (Magnetism)
- Übungen zu Magnetismus (Magnetism, Problem Sessions)
- Seminar: Spin Caloritronics and Spin Pumping
- Seminar: Advances in Solid-State Physics (with D. Einzel, R. Gross, S.T.B. Gönnenwein, A. Marx, M. Opel)
- WMI-Seminar über aktuelle Fragen der Tieftemperatur-Festkörperphysik (WMI Seminar on Current Topics of Low Temperature Solid State Physics, with D. Einzel, R. Gross, S.T.B. Gönnenwein, R. Hackl, A. Marx, M. Opel)
- Seminar zu aktuellen Fragen der Magneto- und Spinelektronik (Seminar on Current Topics in Magneto and Spin Electronics, with S.T.B. Gönnenwein, M. S. Brandt)

The WMI Seminars

The Friday Seminar – Walther-Meißner-Seminar on Current Topics in Low Temperature Physics

WS 2013/2014:

1. **Single-shot readout of superconducting flux qubit using a Josephson parametric amplifier**
   Dr. Tsuyoshi Yamamoto, NEC Smart Energy Research Laboratories, NEC Corporation Tsukuba, Ibaraki, Japan
   16. 10. 2013
2. **Hunds Metallicity in Iron-based Superconductors**
   Dr. Markus Aichhorn, Institute of Theoretical and Computational Physics, Technische Universität Graz, Austria
   08. 11. 2013
3. **Fine structure of the Kondo resonance in ultraclean carbon nanotube quantum dots**
   Dr. Andreas Hüttel, Institut für Experimentelle und Angewandte Physik, Universität Regensburg, Germany
   15. 11. 2013
4. **Superconducting qubits: sidebands, cavities, and vortices**
   Prof. Dr. Britton Plourde, Physics Departments, Syracuse University, Syracuse, USA
   22. 11. 2013
5. **Coupling spins and diamond color centers to superconducting cavities**
   Dr. Johannes Majer, Atominstitut der Österreichischen Universitäten, TU Wien, Austria
   17. 01. 2014
6. **Theoretical understanding of ultrafast electron dynamics in model systems**
   Prof. Dr. Thomas P. Devereaux, Stanford Institute for Materials and Energy Sciences, Stanford, USA
   28. 01. 2014
7. **Quantum simulations of Mott transitions and interacting relativistic theories with photons**
   Prof. Dr. Dimitris G. Angelakis, ECE School, Technical University of Crete Chania, Crete, Greece
   31. 01. 2014
8. **Employing circuit QED to measure non-equilibrium work fluctuations**
   Dipl.-Phys. Ralf Blattmann, Lehrstuhl für Theoretische Physik I, Universität Augsburg, Germany
   07. 02. 2014

SS 2014:

9. **Fermion-fermion scattering with superconducting circuits**
   Laura García-Álvarez, Universidad del País Vasco, Bilbao, Spain
   27. 03. 2014
10. **Strong increase of Tc of Sr_2RuO_4 under both tensile and compressive strain**
    Dr. Clifford W. Hicks, Max-Planck-Institut für Chemische Physik fester Stoffe, Dresden, Germany
    25. 04. 2014
11. **Raman study of the Verwey transition in magnetite (Fe_3O_4) at high pressure and low temperature: effect of Al doping**
    Prof. Dr. Lev Gasparov, University of North Florida, Jacksonville, Florida, USA
    09. 05. 2014
12. **Charge order, Fermi-arc instability and d-wave bond order in underdoped cuprates**
    Prof. Dr. Andrea Damascelli, University of British Columbia, Vancouver, USA
    25. 06. 2014
13. **Hybrid Quantum Systems with Rare-earth Spin Ensemble**
    Prof. Dr. Pavel Bushev, Experimentalphysik, Universität des Saarlandes, Saarbrücken, Germany
    27. 06. 2014
14. **Vom Sand zum Siliziumwafer**
    Dr. Helmut Schwenk, Siltronik AG, Burghausen, Germany
    11. 07. 2014

WS 2014/2015:

15. **Exploring Spin Filter Materials for Oxide Spintronics**
Prof. Dr. Martina Müller, Peter-Grünberg-Institut, Forschungszentrum Jülich, Germany
12. 12. 2014

Topical Seminar on Advances in Solid State Physics – WS 2013/2014, SS 2014 and WS 2014/2015

WS 2013/2014:

1. **Preliminary discussion and assignment of topics**
R. Gross, Walther-Meißner-Institut
15. 10. 2013 and 22. 10. 2013
2. **Heat Flux between Nanosystems and Entropy Produced by Thermal Fluctuations**
Gustav Andersson, Technische Universität München
12. 11. 2013
3. **Exciting Andreev pairs in a superconducting atomic contact**
Sheng-da Wang, Technische Universität München
19. 11. 2013
4. **Storing Information in Magnetic Skyrmions**
Johannes Lang, Technische Universität München
26. 11. 2013
5. **One Year Research in Alabama**
Matthias Althammer, Walther-Meißner-Institut, Garching
03. 12. 2013
6. **Bounding the pseudogap with a line of phase transitions in $YBa_2Cu_3O_{6+\delta}$**
Vasileios Tzanos, Walther-Meißner-Institut, Garching
10. 12. 2013
7. **Extremely Large Magnetoresistance in the Nonmagnetic Metal $PdCoO_2$**
Ludwig Schaidhammer, Technische Universität München
14. 01. 2014
8. **Ultrahigh Magnetoresistance at Room Temperature in Molecular Wires**
Florian Schäble, Technische Universität München
21. 01. 2014

SS 2014:

9. **Preliminary discussion and assignment of topics**
Rudolf Gross, Walther-Meißner-Institut, Garching
08. 04. 2014 and 15. 04. 2014
10. **Topological Insulators**
Manuela Frank, Technische Universität München
29. 04. 2014
11. **Superconducting Circuits for Quantum Information: An Outlook**
Moritz Pflüger, Technische Universität München
13. 05. 2014
12. **Spin-Hall Magnetoresistance in YIG/Au-hybrids**
Tobias Meier, Walther-Meißner-Institut, Garching
20. 05. 2014
13. **Characterization of Graphene Solution Gated Field Effect Transistors**
Tobias Wimmer, Technische Universität München
27. 05. 2014
14. **A first glance at the dynamics of open quantum systems âĂŞ An Introduction to the formalism and to Quantum Process Tomography**

Christian Kathan, Technische Universität München
03. 06. 2014

15. **A Magnet Cryostat Dip Stick for Broadband Ferromagnetic Resonance Experiments**
Felix Hartz, Walther-Meißner-Institut, Garching
17. 06. 2014
16. **Kinetic Monte Carlo Simulations**
Andreas Garhammer, Walther-Meißner-Institut, Garching
24. 06. 2014
17. **Thin Film Fabrication for Spin Current and Spin Caloric Experiments**
Sascha Frölich, Walther-Meißner-Institut, Garching
01. 07. 2014
18. **The relevance of the Yosida function for a microscopic two-fluid description of superconductivity**
Matthias Englbrecht, Walther-Meißner-Institut, Garching
08. 07. 2014
19. **Raman Spectroscopy in CeTe3**
Henrik Gabold, Walther-Meißner-Institut, Garching
15. 07. 2014
20. **Tip-Enhanced Raman Scattering (TERS)**
Maria Theodoridou, Walther-Meißner-Institut, Garching
15. 07. 2014

WS 2014/2015:

21. **Preliminary discussion and assignment of topics**
R. Gross, Walther-Meißner-Institut
07. 10. 2014 and 14. 10. 2014
22. **Optical Detection of Radio Waves through a Nanomechanical Transducer**
Daniel Schwienbacher, Technische Universität München
28. 10. 2014
23. **Room-Temperature Antiferromagnetic Memory Resistor**
Johannes Klicpera, Technische Universität München
11. 11. 2014
24. **Spin Pumping and Spin-Transfer Torques in Antiferromagnets**
Jörg Wohlketzetter, Technische Universität München
18. 11. 2014
25. **Perovskite Oxides for Visible-Light-Absorbing Ferroelectric and Photovoltaic Materials**
Zoltan Jehn, Technische Universität München
02. 12. 2014
26. **Entangling Mechanical Motion with Microwave Fields**
Bernhard Kalis, Technische Universität München
16. 12. 2014
27. **An Electrically Pumped Polariton Laser**
David Busse, Technische Universität München
13. 01. 2015
28. **Quantum Limit of Heat Flow Across a Single Electronic Channel**
Markus Manz, Technische Universität München
20. 01. 2015
29. **Fermi Surface and Pseudogap Evolution in a Cuprate Superconductor**
Maximilian Patzauer, Technische Universität München
27. 01. 2015

Topical Seminar: Spin Caloritronics and Spin Pumping – SS 2014

SS 2014:

1. **Preliminary discussion and assignment of topics**
   Hans Hübl, Walther-Meißner-Institut
   10. 04. 2014 and 17. 04. 2014
2. **Spin Injection in Silicon**
   Kevin Keim, Technische Universität München
   24. 04. 2014
3. **Electrical Noise in Ferromagnetic Thin Films**
   Arthur Niedermayr, Technische Universität München
   05. 06. 2014
4. **Acoustic Spin Pumping**
   Sho Watanabe, Technische Universität München and Keio University
   12. 06. 2014
5. **Electrical Measurements on MoS2**
   Le Anh Tuan, Technische Universität München
   09. 07. 2014
6. **Spin Seebeck Insulator**
   Magdalena Pühl, Technische Universität München
   09. 07. 2014
7. **RF-Measurement Techniques up to THz Frequencies**
   Franz Langrieger, Technische Universität München
   10. 07. 2014
8. **Magnons in Nanostructures Ferromagnetic Thin Films**
   Sebastian Ruß, Technische Universität München
   10. 07. 2014

Topical Seminar on Superconducting Quantum Circuits – WS 2013/2014, SS 2014 and WS 2014/2015

WS 2013/2014:

1. **Preliminary discussion and assignment of topics**
   F. Deppe, A. Marx, R. Gross, Walther-Meißner-Institut
   15. 10. 2013 and 22. 10. 2013
2. **Progress Report**
   Kirill Fedorov, Ling Zhong, Walther-Meißner-Institut, Garching
   26. 11. 2013
3. **Electron spin resonance detected by a superconducting qubit**
   Alexander Baust, Christoph Zollitsch, Walther-Meißner-Institut, Garching
   10. 12. 2013
4. **Nonlinear optics quantum computing with circuit QED**
   Edwin Menzel, Max Häberlein, Walther-Meißner-Institut, Garching
   07. 01. 2014
5. **Dc SQUID coupled to mechanical oscillator**
   Matthias Pernpeintner, Karl Friedrich Wulschner, Walther-Meißner-Institut, Garching
   21. 01. 2014
6. **Towards Realizing a Quantum Memory for a Superconducting Qubit: Storage and Retrieval of quantum states**
   Manuel Schwarz, Jan Goetz, Walther-Meißner-Institut, Garching
   04. 02. 2014

SS 2014:

7. **Preliminary discussion and assignment of topics**
   F. Deppe, A. Marx, R. Gross, Walther-Meißner-Institut
   08. 04. 2014 and 15. 04. 2014
8. **Microstrip Quantum Beam-Splitter and Microwave Interferometer**
   Christian Schneider, Technische Universität München
   22. 04. 2014
9. **On-chip Quantum Beam-Splitter and Microwave Interferometer**
   Michael Fischer, Technische Universität München
   22. 04. 2014
10. **Autonomously stabilized entanglement between two superconducting quantum bits**
    Stephan Kaltenstadler, Technische Universität München
    06. 05. 2014
11. **Engineering the state of light using tunable-gap gradiometric flux qubits**
    Philipp Summer, Technische Universität München
    06. 05. 2014
12. **Reduction of the radiative decay of atomic coherence in squeezed vacuum**
    Marco Berger, Technische Universität München
    20. 05. 2014
13. **Phase stabilization of a microwave generator over extended periods of time**
    Johanna Fischer, Technische Universität München
    20. 05. 2014
14. **Observing single quantum trajectories of a superconducting quantum bits**
    Franz Haslbeck, Technische Universität München
    03. 06. 2014
15. **3D cavities for circuit quantum electrodynamics**
    Jonathan Müller, Technische Universität München
    03. 06. 2014
16. **Superconducting quantum circuits: Microwave resonators with antennas**
    Korbinian Reiser, Technische Universität München
    17. 06. 2014
17. **Superconducting quantum circuits: Microwave resonators with control lines**
    Sebastian Meier, Technische Universität München
    17. 06. 2014
18. **Chains of tunable and nonlinear superconducting resonators**
    Udo Schaumburger, Technische Universität München
    01. 07. 2014
19. **Measurements of RF-SQUID coupled superconducting resonators**
    Fabian Kössel, Technische Universität München
    01. 07. 2014

WS 2014/2015:

20. **Preliminary discussion and assignment of topics**
    F. Deppe, A. Marx, R. Gross, Walther-Meißner-Institut
    07. 10. 2014 and 14. 10. 2014
21. **3D Cavities for circuit QED**
    Gustav Andersson, Technische Universität München
    21. 10. 2014
22. **Coupling of a transmon qubit to a CPW resonator**
    Javier Puertas Martinez, Technische Universität München
    04. 11. 2014
23. **Tracking photon jumps with repeated quantum non-demolition parity measurements**
    Edwar Xie, Walther-Meißner-Institut, Garching

18. 11. 2014

24. **Defining and detecting quantum speedup**
Alexander Baust, Walther-Meißner-Institut, Garching
18. 11. 2014

25. **Fabrication stability of Josephson junctions and superconducting flux qubits**
Lujun Wang, Technische Universität München
02. 12. 2014

26. **8-Channel microwave receiver for quantum experiments**
Martin Betzenbichler, Technische Universität München
02. 12. 2014

27. **Quantum limited amplification and entanglement in coupled nonlinear resonators**
Martin Betzenbichler, Technische Universität München
16. 12. 2014

28. **Unconditional quantum teleportation between distant solid-state quantum bits**
Stefan Pogorzalek, Technische Universität München
16. 12. 2014

29. **Bidirectional and efficient conversion between microwave and optical light**
Jan Goetz, Walther-Meißner-Institut, Garching
20. 01. 2015

30. **Observation of a dissipation-induced classical to quantum transition**
Friedrich Wulschner, Walther-Meißner-Institut, Garching
20. 01. 2015

C: Solid State Colloquium

The WMI has organized the Solid-State Colloquium of the Faculty of Physics in WS 2013/2014, SS 2014, and WS 2014/2015. The detailed program can be found on the WMI webpage: http://www.wmi.badw-muenchen.de/teaching/Seminars/fkkoll.html.

Staff of the Walther-Meißner-Institute

Director
Prof. Dr. Rudolf Gross

Deputy Director
Priv.-Doz. Dr. habil. Sebastian Gönnenwein

Technical Director
Dr. Achim Marx

Administration/Secretary's Office
Ludwig Ossiander

Emel Dönertas

Scientific Staff
Dr. Frank Deppe
Priv.-Doz. Dr. habil Dietrich Einzel
Prof. Dr. Andreas Erb
Dr. Kirill Fedorov
Dr. Stephan Geprägs
Priv.-Doz. Dr. habil. Rudolf Hackl
Dr. Hans Hübl
Dr. Mark Kartsovnik
Dr. Edwin Menzel
Dr. Matthias Opel
Dr. Mathias Weiler

Dipl.-Phys. Andreas Baum
Dipl.-Phys. Alexander Baust
Dipl.-Phys. Thomas Böhm
Dipl.-Phys. Nitin Chelwani
M. Sc. Alma Dorantes
Dipl.-Phys. Peter Eder
Dipl.-Phys. Jan Goetz
Dipl.-Phys. Max Häberlein
Dipl.-Phys. Florian Kretzschmar
Dipl.-Phys. Michael Kunz
Dipl.-Phys. Johannes Lotze
Dipl.-Phys. Hannes Maier-Flaig
Dipl.-Phys. Sibylle Meyer
Dipl.-Phys. Matthias Pernpeintner
Dipl.-Phys. Michael Schreier
Dipl.-Phys. Manuel Schwarz
Dipl.-Phys. Karl Friedrich Wulschner
M. Sc. Edward Xie
Dipl.-Phys. Ling Zhong
Dipl.-Phys. Christoph Zollitsch

Technical Staff
Peter Binkert
Thomas Brenninger, M.Sc.
Dipl.-Ing. (FH) Ulrich Guggenberger
Dieter Guratzsch
Astrid Habel
Karen Helm-Knapp
Dipl.-Ing. (FH) Josef Höss
Sebastian Kammerer
Julius Klaus

Robert Müller
Jan Naundorf
Georg Nitschke
Christian Reichlmeier
Alexander Rössl
Harald Schwaiger
Helmut Thies
Siegfried Wanninger

Assistants
Sybilla Plöderl

Maria Botta

Permanent Guests

Dr. Werner Biberacher
Prof. Dr. B.S. Chandrasekhar
Dr. Karl Neumaier
Dr. Christian Probst
Dr. Kurt Uhlig

Guest Researchers

1. Dr. Werner Biberacher
   permanent guest
2. Prof. Dr. B.S. Chandrasekhar
   permanent guest
3. Dr. Karl Neumaier
   permanent guest
4. Dr. Christian Probst
   permanent guest
5. Dr. Kurt Uhlig
   permanent guest
6. Prof. T.P. Devereaux, Stanford Institute of Materials and Energy Science (SIMES), Stanford University, Stanford, USA
   21. 01. - 30. 01. 2014, 19. 06. - 27. 06. 2014
7. Akashdeep Kamra, Kavli Institute of Nanoscience, Delft University of Technology, Delft, The Netherlands
   03. 02. - 31. 05. 2014
8. Prof. Vladimir Zverev, Institute of Solid Physics, Chernogolovka, Russia
   23.03. - 26. 04. 2014, 16. 06. - 05. 07. 2014
9. Dr. Guillermo Romero, Universidad del Pais Vasco, Bilbao, Spain
   23. 03. - 29. 03. 2014
10. Laura García-Álvarez, Universidad del Pais Vasco, Bilbao, Spain
    23. 03. - 29. 03. 2014
11. Prof. Lev Gasparov, University of Florida, USA
    29. 04. - 14. 05. 2014
12. Prof. Dr. Enrique Solano, Universidad del Pais Vasco, Bilbao, Spain
    15. 05. - 17. 05. 2014
13. Dr. Mikel Sanz, Universidad del Pais Vasco, Bilbao, Spain
    15. 05. - 17. 05. 2014
14. Dr. Nedad Lazarevic, University of Belgrade, Belgrade, Serbia
    02. 06. - 13. 06. 2014, 21. 11. - 05. 12. 2014
15. Dr. B. Moritz, Stanford Institute of Materials and Energy Science (SIMES), Stanford University, Stanford, USA
    19. 06. - 27. 06. 2014
16. Prof. Juan Poyato Ferrera, Instituto de Ciencia de Materiales, Sevilla, Spain
    22. 07. - 30. 07. 2014
17. Prof. Zoran Popovic, University of Belgrade, Belgrade, Serbia
    01. 09. - 14. 09. 2014
18. Dr. Yunshan Cao, Technical University Delft, Netherlands
    19. 10. - 26. 10. 2014
19. Dr. Natasha Kushch, Institute of Problems of Chemical Physics, Chernogolovka, Russia
    03. 11. - 03. 12. 2014
20. Hans Skarsvag, Norwegian University of Science and Technology, Trondheim, Norway
    03. 11. - 10. 11. 2014

Commission for Low Temperature Physics

Members of the Commission for Low Temperature Research of the Bavarian Academy of Sciences and Humanities:

- **Vollhardt, Dieter**, chairman
  (Universität Augsburg)
- **Abstreiter, Gerhard**, deputy chairman
  (Technische Universität München)

- **Bloch, Immanuel**
  (Ludwig-Maximilians-Universität München and Max-Planck-Institut für Quantenoptik)
- **Bühler-Paschen, Silke**
  (Technische Universität Wien)
- **Finley, Jonathan**
  (Technische Universität München)
- **Gross, Rudolf**
  (Technische Universität München)
- **Hänsch, Theodor**
  (Ludwig-Maximilians-Universität München and Max-Planck-Institut für Quantenoptik)
- **Schwoerer, Markus**
  (Universität Bayreuth)
- **Wallraff, Andreas**
  (Eidgenössische Technische Hochschule Zürich)
- **Weiss, Dieter**
  (Universität Regensburg)
- **Zinth, Wolfgang**
  (Ludwig-Maximilians-Universität München)